THE ^{64}Zn(t,^{3}He) CHARGE-EXCHANGE REACTION AT 115 MeV PER NUCLEON AND APPLICATION TO ^{64}Zn STELLAR ELECTRON-CAPTURE

By

George Wesley Hitt

AN ABSTRACT OF A DISSERTATION

Submitted to
Michigan State University
in partial fulfillment of the requirements
for the degree of

DOCTOR OF PHILOSOPHY

Department of Physics and Astronomy

2009

Remco G. T. Zegers

ABSTRACT

THE ^{64}Zn(t,^{3}He) CHARGE-EXCHANGE REACTION AT 115 MeV PER NUCLEON AND APPLICATION TO ^{64}Zn STELLAR ELECTRON-CAPTURE

By

George Wesley Hitt

A secondary, 115 MeV per nucleon triton beam has been reinstituted at the National Superconducting Cyclotron Laboratory for use in (t,^{3}He) charge-exchange reaction studies. This (n,p)-type charge-exchange reaction is useful for extracting the full Gamow-Teller (GT) response of the nucleus, overcoming Q-value restrictions present in conventional decay studies. The GT$_+$-strength in the pf-shell nucleus ^{64}Cu has been determined from the absolute cross section measurement of ^{64}Zn(t,^{3}He) near zero-degrees, exploiting an empirical proportionality between the differential angular cross section and the GT-strength. The detailed features of the GT$_+$-strength distribution in a nucleus has an important impact on electron-capture rates in Type Ia and core-collapse supernovae. The measured GT$_+$-strength in ^{64}Cu is directly compared with the results of modern pf-shell effective interactions GXPF1a and KB3G which can be used to calculate the GT$_+$ contribution to electron-capture on nuclei in supernova simulations. The (t,^{3}He) charge-exchange program at the National Superconducting Cyclotron Laboratory provides stringent tests and can aid the development of such nuclear shell-model calculations.

Contents

List of Tables

List of Figures

Images in this dissertation are presented in color.

Chapter 1

Introduction

In a nuclear collision, charge-exchange reactions result from the projectile exchanging a proton for a neutron, or vice-versa, with the target nucleus. The charge-exchange reaction is a useful tool for investigating features of electron-capture in the stellar environment. Electron captures are expected to play an important role in thermonuclear and core-collapse supernovae. In this work, the focus is on charge-exchange reactions at intermediate beam energy ($\sim$100 MeV/nucleon). The reaction is mediated by the isospin-flip components of the nucleon-nucleus interaction which contains a variety of terms related to meson-exchange [1]. Of particular importance for describing electron-capture rates are Gamow-Teller transition strengths which are associated with spin and isospin transfer. In the effective nucleon-nucleus interaction, such transitions are represented by components with the range of the one-pion exchange potential (OPEP) [2]. This work focuses on GT transitions from ^{64}Zn to ^{64}Cu, studied using the ^{64}Zn(t,^{3}He)^{64}Cu charge-exchange reaction. The ^{64}Zn parent nucleus is presumably a pf-shell nucleus, and the knowledge of electron-capture rates on pf-shell nuclei are crucial for both thermonuclear [3] and core-collapse supernovae [4].

Gamow-Teller transitions induced by charge-exchange reactions are mediated via the spin-isospin ($\sigma\tau$) component $V_{\sigma\tau}$ of the strong nuclear interaction. Information about the weak process can be obtained however, because of the similar action of the bare $\sigma\tau$ operator in the β-decay process and connection of identical initial and final nuclear states

by this operator in both charge-exchange and β-decay processes. In fact, as described in Chapter 3, a simple proportionality exists between the charge-exchange differential cross section in the limit of vanishing momentum transfer and the Gamow-Teller matrix element of β-decay transitions. Provided the GT matrix elements can be reliably separated from other effects of the strong nuclear interaction, the cross section for a charge-exchange reaction will then be advantageously larger than its weak, electron-capture analog. An important difference with β-decay is that charge-exchange is unhindered by Q-value restrictions present in direct electron-capture studies. Many nuclei, that otherwise have prohibitive electron-capture Q-values, efficiently capture the degenerate, high-energy electrons in dense stellar cores. Charge-exchange reactions can probe the full Gamow-Teller response of the nucleus. This includes the response as it is seen by electron-capture in the stellar environment. This information then is a valuable addition to supernova modeling efforts, offering stringent tests of B(GT) inputs determined from nuclear structure theory.

Outline

The following work is from a nuclear experimental perspective and examines the light-ion charge-exchange reaction ^{64}Zn(t,^{3}He)^{64}Cu. In the current Chapter, a brief historical review of the connection between charge-exchange experiments and supernova theory is given. Next, in Chapter 2, the salient features of stellar electron-capture are discussed, emphasizing the rate-sensitivity to the detailed B(GT) distribution in the daughter nucleus. It is the rate-sensitivity to the distribution of GT states that is an important motivation for high-resolution charge-exchange measurements. In Chapter 3, the charge-exchange reaction is described based on the distorted-wave Born approximation. The necessary steps are taken there to account for the composite nature of the (t,^{3}He) probe and to develop theoretical tools needed to extract B(GT) from measured cross sections. Chapter 4 provides an account of all experiments performed and equipment used to realize the ^{64}Zn(t,^{3}He)^{64}Cu measurement. This includes the development of a secondary triton beam [5–7], the inaugural measurement with the ^{24}Mg(t,^{3}He) reaction [8], cali-

bration measurements, and steps taken to maximize the experimental resolution of the residue excitation energy. Chapter 5 gives an account of the data analysis procedure for determining differential cross sections of the ^{64}Zn(t,^{3}He) reaction. Chapter 6 applies the methods discussed in Chapter 3 to the measured cross sections and from them extracts the Gamow-Teller operator strength in ^{64}Cu. Chapter 7 presents the ^{64}Zn ground state electron-capture rate calculation, performed for a variety of stellar density and temperature conditions. Electron-capture rates for two large-scale shell-model B(GT) distributions are also included. Two temperature and density profiles for the capture rates (data and shell-model) are presented, but a grid of rates for 14 electron densities ($1 \geq \rho Y_e \geq 10^{14}$ g/cm^3) and 13 temperatures ($0.010 \geq T_9 \geq 100 \times 10^9$K) covering most scenarios have been tabulated. Chapter 8 summarizes the main findings of the triton beam development, the ^{64}Zn measurement, and the shell-model performance for calculating B(GT) in the pf-shell. Recommendations are made for future improvements and new measurement efforts.

Historical Link with Supernovae

The first charge-exchange reaction studies carried out were with the (p,n) reaction at what was the University of California Radiation Laboratory in the late-1950's [9]. Using the neutron-time-of-flight facility there, low energy (p,n) reaction studies were carried out on a wide variety of nuclei (e.g. [10, 11]). These data were soon supplemented by (p,n) measurements made with protons from the AERE Harwell syncrocyclotron in Berkshire, England (e.g. [12]). On the basis of these data, it was observed that, while there is a strong resonance corresponding to the population of the target's isobaric analog state (IAS) in the residue, there was an apparent lack of spin-flip resonances ($\Delta L = 0, \Delta S = 1, \Delta T = 1$). Ikeda *et al.* [13] in 1963 treated the (p,n) reaction as an analogy to β-decay, where population of the IAS was similar to the Fermi-type (F) decay ($\Delta L = 0, \Delta S = 0, \Delta T = 1$) and the spin-flip transition to that of Gamow-Teller (GT) decay. They suggest this is reasonable with the (p,n) reaction at forward angles (i.e. low-momentum transfer q),

since β-decay involves very small q. By treating the (p,n) reaction in the first Born approximation, and comparing with β-decay ft and photo-effect data, they interpreted the lack of spin-flip resonances at these low-excitation energies as evidence that a collective GT-type resonance must exist at several MeV of excitation [13].

The GT giant resonance predicted by Ikeda *et al.* [13] was experimentally observed in 1975, in a series of 0° (p,n) reaction measurements at Michigan State University's Cyclotron Laboratory, by Doering *et al.* [14] using a beam of 35 MeV protons. On targets of ^{48}Ca,^{90}Zr,^{120}Sn, and ^{208}Pb, these authors located the GT giant resonance in each case at several MeV in excitation above the IAS. The result was not without controversy. However, the (p,n) charge-exchange program at the Indiana University Cyclotron Facility (IUCF), beginning in February of 1979 [15], significantly advanced the state of the art. Among many lines of investigation, one was a campaign to deepen the understanding of collective spin-isospin modes in nuclei, particularly the GT giant resonance. Within a few years, the facility yielded a large body of intermediate energy (E_p $\sim$130-160 MeV) (p,n) reaction data over a wide range of target masses [15–21], confirming the existence of the GT giant resonance.

Around the same time of these discoveries, Bethe *et al.* in 1979 [22] recognized two important consequences of the existence of the giant Gamow-Teller state. First, though somewhat less related to the present work, was that ground-state to ground-state and low-excitation β-transitions of all types (decays or captures) are hindered through admixture with the giant GT state's single-particle configurations. This essentially pushes strength out of low-lying states and up to the giant GT state. The second, directly relevant issue is that, in a core-collapse supernova explosion, the Fermi energy due to the gravitational confinement of the degenerate electrons would allow them to access the giant GT resonance (GTR) in the daughter directly in an electron-capture [22]. As a qualifier, Bethe *et al.* pointed out that at the time of their writing, a single concentration of B(GT$_+$), that is Gamow-Teller strength seen in the isospin raising direction, had not been observed like it had for B(GT$_-$) from the isospin-lowering (p,n) measurements. The hindrance of low-lying transitions, for both β-decays and electron-captures, will be the

same whether or not a single giant GT resonance exists in a given nucleus. As is discussed below however, there typically isn't a single, strong giant GT_+ state in electron-capture daughters. This has important consequences for the stellar electron-capture rate and is a key motivation for later uses of high-resolution charge-exchange measurements.

In the meantime, a fruitful feedback between nuclear shell-model and supernova theory formed. Shortly after Bethe *et al.*, authors Fuller, Fowler and Newman (FFN) worked to treat all β-transitions in the supernova in a more realistic way. In a famous series of papers starting in 1980 [23–27], they calculated electron-capture rates for *sd* and lower pf-shell nuclei, parameterized as a function of stellar temperature and density. Primarily, Fuller *et al.* made use of existing decay data, shell-model calculations and simple independent-particle models to determine the location and strength of the low-lying B(GT) and the GTR. These rates remained a standard input for supernova models for more than 20 years. For electron-capture, a typical FFN input for a given nucleus consisted of a few low-lying transition strengths inferred from β-decay measurements and a location and width of the giant GT state. Again, unlike the GTR seen in the (p,n) reaction, the GTR in the electron-capture direction is in reality a relatively looser grouping of $B(GT_+)$, spread over multiple discrete states. And again, this will have important consequences for the stellar electron-capture rate.

Meanwhile, several systematic regularities were emerging from the growing body of forward-angle (p,n) reaction data. This was aided by new (p,n) charge-exchange facilities, coming online in the mid-1980's at TRIUMF (e.g. Ref. [28]) and Los Alamos National Laboratory (LANL) [29]. Between these two facilities and IUCF, (p,n) reactions could be performed at bombarding energies from 50 to 800 MeV; IUCF providing proton beams from 50 to 200 MeV, TRIUMF from 200 to 500 MeV and LANL at 318 and 800 MeV. It appeared that there was a strong energy dependence in the ratio of cross sections for Fermi and Gamow-Teller type excitations [28, 30]. These effects were described nicely by treating the (p,n) reaction in the distorted-wave Born approximation (DWBA) and the N-nucleus interaction by using an effective NN-interaction derived from nucleon-nucleon scattering data by authors Love and Franey [2, 31]. Also, it appeared that the β-decay

strengths B(F) and B(GT) were related to the (p,n) cross sections at forward angles for exciting the IAS and GT giant resonances, respectively [32]. Taddeucci *et al.* found empirically that this relationship is linear with an energy-dependent coefficient [32]. This opened the possibility that energetically inaccessible β-decay strength can be probed, over a wide mass range, by exploiting its analogous relationship with the (p,n) reaction at forward angles [32].

The experimental work of Taddeucci *et al.* [32] and the theoretical work of Love and Franey [2, 31] established a firm basis for developing other charge-exchange probes to extract B(GT). Among other points, their work cemented the importance of intermediate beam energy ($\gtrsim$ 100 MeV/nucleon) for isolating the action of $V_{\sigma\tau}$, responsible for the GT transition, from other terms in the effective interaction. Of course, the (p,n) reaction only excites $\Delta T = 1$ modes, specifically by lowering the isospin projection $\Delta T_z = -1$. This is analogous to β-decay and samples the GT$_-$ strength in the daughter. To determine B(GT$_+$), the strength associated with raising the isospin projection $\Delta T_z = +1$ and electron-capture, the (n,p) reaction was first developed at Crocker National Laboratory at UC Davis in 1982 [33]. The most extensive (n,p) program was later developed in the late 1980's at TRIUMF [34]. At this time, the (p,n) and (n,p) reactions respectively allowed determination of the B(GT$_-$) and B(GT$_+$) in nuclei, with corresponding resolutions of $\sim$300 keV and $\sim$1 MeV (FWHM). In the first case, the resolution is set by intrinsic limitations on measuring neutron energies by the time-of-flight method. In the later case, the resolution is dominated by the energy spread of the neutron beam. Consequently, (n,p) studies have tended to be insensitive to the fragmentation of B(GT$_+$) and features of the detailed distribution remained unknown.

Composite charge-exchange probes were also becoming available as probes of B(GT), around the same time as the discovery of the GTR with (p,n) reactions. In the isospin raising direction, a low energy (E_t = 25 MeV) (t,^{3}He) probe was developed at Los Alamos National Laboratory (LANL) in 1972 [35]. Initially, these measurements were not aimed at investigating B(GT) and, as mentioned above, their ejectile spectra contained strong contributions from terms other than the $V_{\sigma\tau}$ operator at this relatively low beam

energy. In their case, the central-volume term V_o^C, responsible for optical distortion and mainly for multi-step processes, played a strong role and necessitated coupled-channel calculations to separate terms in the analysis. Consequently, the remainder of this history will be limited discussion of higher energy measurements. Nevertheless, it was clear from these data published by Flynn *et al.* [35] that states populated by $\Delta T_z = +1$ spin-isospin excitation could be measured with greatly improved resolution over that of (n,p) reactions. In their case, this was 55 keV FWHM, due largely to small energy spread of the primary t-beam.

The reverse reaction with the (^{3}He,t) probe was developed in 1983 at Laboratoire National Saturne (Saclay) [36] at 200, 400 and 670 MeV/nucleon, although the excitation energy resolution was 1.1 MeV (FWHM) or more. In 1993, (^{3}He,t) at 70 MeV/nucleon was added at IUCF [37], achieving ∼130 keV excitation energy resolutions. The (^{3}He,t) probe was further developed the following year at the Research Center for Nuclear Physics (RCNP), Osaka [38] and at Kernfysisch Versneller Instituut (KVI) in 2000 [39] with 150 and 60 MeV/nucleon bombarding energies, respectively. At its inception, the RCNP program featured this $\Delta T_z = -1$ probe with 210 keV resolution (FWHM). Presently, (^{3}He,t) measurements at RCNP routinely achieve an impressive ∼30 keV resolution. In the reverse direction, $\Delta T_z = +1$, the (d,^{2}He) probe was developed in 1995 at the Institute of Physical and Chemical Research (RIKEN), Japan [40], in 1996 at Texas A&M [41] and at KVI in 2002 [42]. The KVI program was the most extensive, achieving resolutions of ∼120 keV, although presently, there are no active (d,^{2}He) charge-exchange programs. Lastly, the (t,^{3}He) probe at 127 MeV/nucleon was demonstrated at the National Superconducting Cyclotron Laboratory using a secondary triton beam [5, 6] in 1997.

Of particular note among these programs, was the initial work of Jänecke *et al.* in 1993 at IUCF with the (^{3}He,t) probe. There, the authors make use the technique's ∼130 keV energy resolution to successfully observe the fragmentation of the GTR anticipated by Gaponov and Lyutostanskii in 1974 [43], and Brown *et al.* in 1988 [44]. This was confirmed by subsequent measurements on many nuclei during the above mentioned programs at IUCF and RCNP. The fragmentation of the GT strength is particularly important for

calculating the associated stellar weak rates, as discussed in Chapter 2.

As mentioned above, during this period in the 80's and 90's, the weak rates determined by FFN using early shell-model and independent particle model (IPM) determinations of B(GT) were the standard in thermonuclear and core-collapse supernova modeling. It was understood that the techniques used by FFN would not locate the GTR in the most precise way since they neglected residual interactions among nucleons [43,44]. Limitations on computing power at the time however, meant that the alternative, fully diagonalizing the Hamiltonians in the *sd*- and *pf*-shell model spaces, was not possible. For the *sd*-shell, this was no longer the case by the early 1990's and shell-model B(GT) and weak rates incorporating realistic residual interactions were made available by Kajino *et al.* [45]. Similarly, in 2000, Langanke and Martínez-Pinedo (LMP) completed large-scale shell-model determinations of B(GT) in the mass region $A = 45-65$ [46]. From these rate sets, both groups make direct comparisons with FFN. Overall, the effect of adding realistic residual interactions, as shown in earlier charge-exchange measurements, was that the B(GT) was fragmented over many individual final states, and that the centroid tended to move to higher excitation energy in the daughter nucleus.

Consequently, newer electron-capture rates tended to be lower than FFN rates, on both *sd*-shell [45] and *pf*-shell [46] nuclei. Immediately after the LMP publication, supernova modelers Brachwitz *et al.* [3] in 2000 and later Hix *et al.* in 2003 [4] explored the implication of these revised rates for thermonuclear Type Ia and core-collapse supernova trajectories, respectively. In both scenarios, these authors found that the lowered rates imply significantly different electron fractions Y_e in the pre-supernova star and changes to the explosion dynamics. In the Type Ia case, the new rates significantly altered the ignition conditions and the nucleosynthesis yields for iron-group elements [3]. Specifically, in the Type Ia scenario, the lower rates imply, by way of constraint, lower electron fractions and consequently imply higher central ignition densities. In the core-collapse case, the new rates significantly altered the matter composition of the pre-collapse outer-core and boosted the post-bounce neutrino luminosity and energy spectrum [4].

These results, since they lead to such large changes to supernova evolution, fueled

interest in examining experimental determinations of B(GT) with charge-exchange reactions. Those measurements achieving resolutions of a few hundred keV or better are particularly attractive, since they can resolve the detailed features of the B(GT) distribution. Consequently, such measurements can make a stringent distinction between the performance of FFN, LMP or other methods for determining the B(GT) distribution and the associated electron-capture rates. For charge-exchange in the electron-capture direction, there are currently no functioning (d,^{2}He) programs which have reliably provided B(GT) distributions with high resolution. Also, the (t,^{3}He) programs at LANL and KVI, using a primary triton beams with 25 MeV and 120 MeV respectively, were discontinued. Furthermore, the Coupled Cyclotron Facility (CCF) upgrade at NSCL [47] removed that facilities capability to produce secondary tritons, which relied on a primary α beam. Therefore, there is currently a strong motivation to reinstitute a high-resolution charge-exchange probe for extraction of B(GT$_+$) distributions.

The lightest beams now available at the NSCL CCF are ^{16,18}O beams. Therefore, the redevelopment of the (t,^{3}He) probe at NSCL, using secondary tritons from fragmentation of ^{16,18}O, has been studied [7]. Also, both supernova sensitivity studies [3, 4] that motivate the present work demonstrated that upper pf-shell and heavier nuclei are important electron-capture parents. Therefore, the ^{64}Zn(t,^{3}He) charge-exchange reaction has been studied, for its relevance in thermonuclear and core-collapse supernovae. Of course, one can only study the ground state capture rate, yet several nuclei, often radioactive species, are important capture parents at any given point on the supernova trajectory (e.g. Ref. [48,49]). And excited-state to excited-state transitions are experimentally inaccessible and numerous. Therefore, the more important use of this and subsequent (t,^{3}He) measurements is as a test of B(GT$_+$) distributions determined theoretically. This work will examine the performance of the shell-model B(GT$_+$) in ^{64}Cu, using the codes OXBASH [50] and NuShellX [51] and the pf-shell effective interactions KB3G [52] and GXPF1A [53]. These or similar methods for calculating B(GT) distributions inevitably will provide the majority of transitions as input for supernova simulations. Therefore, it is important to use measurable cases like ^{64}Zn(t,^{3}He)^{64}Cu to build confidence in the

theoretical determination of B(GT) in general.

Chapter 2

Astrophysics Motivation

This chapter motivates the determination of Gamow-Teller strength for its importance in stellar electron-capture, specifically for supernovae. First, the observational history of supernovae and the resulting taxonomy is reviewed, concluding with the current understanding of the various progenitor types. Next, the foundational works of Fuller, Fowler and Newmann [23–27] are briefly reviewed, at first for their description of the influence from the stellar environment on electron-capture rates. Next, for each progenitor/supernova type the role of electron-capture is discussed, as it influences explosion models. Particular attention is given to sensitivity studies mentioned in Chapter 1 [3, 4], done with supernova models, using electron-capture rates based on $B(GT_+)$ distributions determined by simplified treatments like that of Fuller *et al.* or modern shell-model calculations. Significant differences in supernova evolution revealed by these studies result from the electron-capture rate's sensitivity to the detailed $B(GT_+)$ distribution. A discussion of these consequences conclude the chapter and provide motivation for measuring the $B(GT_+)$ in electron-capture daughters.

2.1 An Introduction to Supernovae

Supernovae are extremely bright, short-lived, cataclysmic astronomical explosions that release, in a matter of days, many times more energy than is radiated by an average star

during its entire lifetime. For example, our Sun radiates $\sim 10^{33}$ ergs per second. Compare this to the typical energy released in photons by supernovae of $\sim 10^{51}$ ergs [54]. This is comparable to the integrated intensity of our Sun, radiating at its current output, for more than 10 billion years ($\sim 3.2 \times 10^{17}$ seconds), the typical theoretical lifetime of such a star. Supernova luminosities are typically such that, at their peak light output, they often outshine their host galaxies.

The observational history of supernovae stretches back thousands of years, predating virtually all observational technology, since supernovae occurring locally in our own Milky Way galaxy have often outshined all other stars in the night sky. Some have had apparent magnitudes bright enough to make them visible to the naked eye during daylight hours. One candidate for the oldest observation comes from a stone tablet unearthed in the Kashmir region of India, dated to perhaps 5500 to 5700 B.C, depicting a bright pair of stars in the vicinity of the constellations Orion and Taurus [55]. More recently, medieval observations ranging from ancient Japanese and Chinese texts to Native American cave paintings in North America all point to very bright, anomalous star appearing mid-year in 1054 A.D. These observations have been well-correlated to the famous Crab Nebula, located in the constellation Taurus. More famously, a pair of local supernovae occurred in 1572 and 1604 A.D., being traditionally attributed to Tycho Brahe and Johannes Kepler, respectively. Their remnants are located in the constellations Cassiopeia and Ophiuchus respectively. The last supernova to take place in or near our galaxy was 1987A in 1987, in the Large Magellanic Cloud, just outside the Milky Way proper some 169,000 light years away. Supernova 1987A is most remarkable because it was detected perhaps several hours after the explosion and neutrino events correlated with the explosion were observed. This makes it one of the best known supernovae and one of the only ones where detailed data is available on the progenitor star.

Modern observations made with ground and space-based telescopes have vastly increased both the number of known supernovae and also knowledge of their particular features. The first extra-galactic supernova observed, S Andromedae (also known as SN1885A) was discovered in the Andromeda galaxy by C. E. A. Hartwig in 1885. Since

then, the development of larger telescopes with deeper ranges has lead to nearly 5000 cataloged supernovae in the wider observable universe to date. The most distant observation to date is SN1997ff [56], seen possibly as far away as 10 billion light years. Many supernova surveys are currently under way, such as the Supernova Legacy Survey (SNLS), the Equation of State Supernova Cosmology Experiment (ESSENCE) and the Lick Observatory and Tengara Observatory Supernova Searches (LOTOSS) to name a few. The number of observations is set to dramatically increase in the immediate future as well, as the Sloan Supernova Survey, part of the Sloan Digital Sky Survey-II, advances analysis of a comprehensive campaign of observations taken from 2005-2007 [57, 58]. In the first two three-month observational seasons alone, nearly 400 supernovae were detected and confirmed.

Along side technical advances that allowed such distant and numerous observations, the capability to conduct detailed spectroscopic studies of the supernova light has also developed. Issac Newton was among the first to record his observation that sunlight can be decomposed into its component colors by refraction in a prism. However, it was J. Fraunhofer that first made a detailed description of the solar absorption spectrum, a series of narrow, dark lines seen in an otherwise uniform spectrum of visible colors in sunlight. By the 1930's, refined spectroscopic and photometric techniques were being applied to telescopic supernova observations, making information on their isotopic composition and time evolution available.

From the current wealth of data, some basic features of supernovae emerge. It is generally seen that galaxies, with chemical composition like our own Milky Way, experience $\sim 2 \pm 1$ supernovae per century. The time evolution of their luminosities, or "light-curves", generally rise quickly and reach peak luminosity on the order of days. After reaching peak light, their luminosities fade significantly over a period of several months. Supernovae can be broadly classified as Type I or Type II supernovae, based on the absence or presence, respectively, of hydrogen absorption lines in their early spectra [59]. Finer distinctions arose as the quality of spectroscopic data increased. F. Bertola first discovered the absence of silicon absorption lines [60] that later split Type I into categories with and without

silicon II P Cygni absorption lines in their spectra. Respectively, these are the Type Ia and Ib categories [61]. The Type Ib class was then further divided, those with and without helium absorption, into Type Ib proper and the new Type Ic respectively [62]. Type II supernovae have also been subdivided into several categories, though based mainly on differences in light-curves, not atomic absorption spectra. The divisions are not as sharp as those in the Type I family, as Type II events show much less regularity, and intermediate cases exist between almost any possible divisions. Perhaps the most significant division to date comes from R. Barbon *et al.* [63], between so called Type IIP and Type IIL. Type IIP designating events where the luminosity plateaus (P) for several weeks before significantly decaying. The luminosity of Type IIL events decrease linearly (L) as a function of time. More sophisticated divisions than these have been made but they are beyond the scope of this text. The more relevant distinctions come from investigations into the progenitors and explosion mechanisms, as constrained by these observational classes.

2.2 Type Ia Model

One of the most interesting features of Type Ia supernovae is the high degree of regularity in their absorption spectra and light curves. This suggests that the physical mechanism and conditions leading up to the explosion event are fundamentally the same in some way. Indeed, before the clear distinction between Type I and Type II supernovae had even been made, there were already suggestions by Zwicky in 1938 [64] that the regularity of their luminosities would make supernovae excellent "standard candles" for measuring intergalactic distances. The use of Type Ia supernovae as distance indicators was also bolstered by early work on the theory of white dwarf stars. Chandrasekhar began this effort around the time that Bethe had forwarded that hydrogen fusion into helium might be the primary energy generation mechanism in the sun. Chandrasekhar determined that the life of a Sun-like star would end as an inert core of helium ash, held up entirely by electron degeneracy pressure. This offered a satisfactory explanation of Sirius A's invisible

companion which, being only 8 light years away and yet having a very hot thermal emission spectrum, could be no larger than the Earth. It also laid the foundation for the theory of carbon-oxygen white dwarfs, a more massive analog to the helium white dwarf, which remains the frontrunner among Type Ia progenitor models.

As Type Ia supernovae relate to distance measurements; the seminal work of E. Hubble [65] has perhaps been the single strongest motivation behind ongoing efforts to characterize Type Ia explosions. His observation that the spectral redshift of other galaxies, due to their radial egression, is proportional to their distance from our own Milky Way lead him to conclude that the universe is expanding. Though the accepted value for Hubble's constant H_0, the proportionality constant in Hubble's Law, has changed over the intervening years, this basic fact remains one of the most often cited evidences for Big Bang cosmology. Efforts to determine H_0 independently (apart from Cephids and galactic properties) using Type Ia supernovae began with C. T. Kowal [66], once the taxonomic classes of supernovae settled and the regularity of the Type Ia class began to emerge. New observations and finer taxonomic distinction steadily reduced the dispersion in Kowal's result and interest in determining the value of H_0 greatly intensified after 1975 [67]. As a result, by 1979 the Type Ia supernova were regarded as so regular that G. A. Tammann proposed that they could be observed at large redshift ($z > 0.5$) using the Hubble Space Telescope for determination of Einstein's cosmological constant Λ [68].

However, the intense efforts to exploit the regularity of Type Ia supernovae as distance indicators also slowly revealed their intrinsic diversity, first noticed in 1987 [69]. There is now a well-known "Phillip's Relation" [70] which is a correlation between the decline rate and the peak-luminosity of Type Ia supernovae. In simplistic terms, the light curves of bright Type Ia supernovae decay slowly and dim events decay more quickly. Phillips *et al.* showed [70] that this relationship is indeed intrinsic to the Type Ia event itself and not due to reddening from dust in the host environment which can only attenuate the light curve, not alter its shape. This immediately presented a strong motivation to determine a calibration for Type Ia supernova luminosities so as to restore confidence in their use as standard candles. Phillps *et al.* [70] does so in a empirical way and quotes a refinement

to H_0. However, it would be very satisfying to place the result on a more fundamental theoretical footing (e.g. Ref. [71]). Early theoretical work suggested the regularity of the Type Ia explosion was due to the regularity of the progenitor star and the explosion mechanism. Therefore, a major goal of ongoing theoretical efforts is to produce a Type Ia explosion model that yields the observed diversity and can relate it to fundamental micro-physics in the explosion mechanism.

Along a parallel front, Type Ia supernovae attracted attention as an important site for the nucleosynthesis and distribution of heavy elements in the universe. Burbidge, Burbidge, Fowler and Hoyle (B^2FH), using data on solar system isotopic abundances, laboratory spectroscopy of nuclei and stellar models from observational astronomy, first proposed in 1957 a detailed and multifaceted scenario for how stars might synthesize all heavy elements from primordial hydrogen [72]. Soon afterward, Hoyle and Fowler suggested that supernovae were possible sites for iron-group nucleosynthesis [73]. In their model, they linked supernovae to the aforementioned carbon-oxygen white dwarf, one which was particularly near in mass to the Chandrasekhar limit. They showed that the ignition of carbon-fusion in this electron-degenerate environment would not lead to a pressure increase, the subsequent feedback necessary to establish stable burning conditions, since the equation of state yields a pressure that is only density-dependent. Instead, they showed that a runaway thermonuclear reaction should take place, burning the entire white-dwarf into ^{56}Ni. The appeal of this model was considerable. Since explosion sets in when the white dwarf progenitor exceeds the Chandrasekhar mass, all explosions would start with practically identical amounts of carbon-oxygen fuel, tightly confined in the same configuration. Also, since the entire mass is converted to ^{56}Ni, the explosions would be monoenergetic and the radioactive decay of ^{56}Ni would produce a homogeneous light curve at late times.

Intermediate-mass spectroscopy of supernova light, which lead to the division of the Type I class into Type Ia, Ib and Ic subgroups as mentioned above, complicated the situation for such simple models. The most significant break with Hoyle and Fowler's simple model was later observation that the mass of ^{56}Ni produced in Type Ia explosions is vari-

able. Much smaller amounts are sufficient to reproduce the observed spectroscopy [74]. Typically, 0.6 solar masses of ^{56}Ni (or about half the white-dwarf mass) is observed [75,76] and variations are seen, from as little as 0.07 solar masses like in SN1991bg [77] and as much as 0.92 sloar masses like in SN1991T [78]. Realistic models are now required to reproduce the observed isotopic abundance pattern of Type Ia ejecta. However, this requirement also lead models to convergence with the requirements placed on them by the aforementioned Phillips-relation. Motivation to understand the dispersion within the Type Ia class and enhanced computing resources available by the early to mid 1990's fueled a burst in modeling efforts. Explosion models began to include sophisticated features such as off-center ignition points, subsonic deflagration rather than supersonic burning, pulse-delayed transitions to detonation and sub-Chandrasekhar mass progenitors (e.g. Refs. [79–86]).

At this point, a contemporary summary of the observational constraints on the Type Ia explosion model is instructive. Hillebrandt and Niemeyer in Ref. [87] have made a thorough review of the observational features of Type Ia supernovae and summarized the requirements that they place on explosion models. First, they note that the tail of the Type Ia supernovae light curve is entirely explained by the gamma emissions of radioactive ^{56}Ni to ^{56}Co daughters and ^{56}Fe granddaughters. Also, as the ejecta expand and become optically thin, spectroscopy reveals, as mentioned in the Type Ia taxonomy, a near-total lack of hydrogen and helium but a wide variety of intermediate-mass nuclei. Therefore, explosion models must be powerful enough to produce sufficient amounts of ^{56}Ni and intermediate-mass isotopes from material heavier than helium. Additionally, the ejecta must have velocities that agree with observed Doppler corrections from absorption spectra, blue-shifted due to speeds on the order of 10,000 km/s. Furthermore, the isotopic abundance of ejecta cannot show large deviations with solar abundances in the aggregate and Fe-peak.

Second, it is seen that Type Ia supernovae have highly regular absorption spectra and light curves. In other words, over a large sample of Type Ia observations, the tails of light curves are consistently determined by ^{56}Ni decay alone and the representation

of intermediate-mass nuclei in late-time absorption spectra are recurrent. The authors of Ref. [87] then conclude that a standard explosion mechanism should be robust enough to produce highly regular explosions without fine-tuning model parameters and initial conditions.

Third, it is well-established that all major deviations in the observables amongst Type Ia supernovae are strongly correlated with the explosion strength [88]. In general, stronger explosions have brighter peak-light, are brighter for longer times, have more blue-shifted spectra, and have faster ejecta velocities. Therefore, the explosion model should have at least a single tunable parameter that directly influences the explosion strength without breaking any of the correlations seen with light curves and spectra [87].

Fourth and last, for very distant Type Ia supernovae (redshift of $z>0.8$), the brightness seems dimmer and rise-times slower than expected. This suggests variations in explosion strength as a function of host galaxy age, metalicity, or some other similar property. Therefore, a final necessary constraint on an acceptable explosion model is its correlation with progenitor system and its host environment [87].

Based on these constraints, the near-Chandrasekhar-mass, carbon-oxygen white dwarf model remains the most widely accepted progenitor [87]. There are also several significant theoretical challenges that remain to be overcome for explosion models based on this progenitor. In broad terms, these are; 1) determination of the central ignition density, 2) the propagation of the flame-front, 3) transition from simmering and deflagration to detonation phases, and 4) reproduction of observed spectra and light curves [89]. Of course, the spectra and light curves are the only direct observables of the Type Ia event. Also, determination of the central ignition density remains the most uncertain of these four outstanding problems. Discussion of sensitivity studies which conclude this chapter, show that electron-capture plays a significant role both of these two major challenges.

2.3 Core-Collapse Model

Authors W. Baade and F. Zwicky were the first to posit the theory that supernovae are caused by stars collapsing into neutron stars [90]. Ironically, all known supernovae at that time, which they based their calculations on, were later determined to be Type Ia events. Nevertheless, their considerations proved remarkably insightful, once applied to the later distinct Type II class, and to this day it remains the essential basis of core-collapse supernova theory. Unlike Type Ia events however, core-collapse explosions exhibit significant irregularities. The core-collapse category has received defectors from the Type I group, those of the above mentioned Type Ib and Type Ic class. These events are the explosion of massive stars ($>30M_{\text{solar}}$) that have previously ejected their outer hydrogen (Type Ib) or outer helium (Type Ic) envelopes. Those remaining in the Type II class have been identified as having progenitor stars in the range of 8-30 M_{solar}.

This lower threshold of $M > 8M_{\text{solar}}$ roughly corresponds to the ignition conditions for carbon fusion, which is the key difference between core-collapse and Type Ia progenitors. Stars that do not produce temperatures sufficient to ignite carbon fusion burning end their lives as helium white dwarfs (in mass-tranferring binary systems) or as carbon-oxygen white dwarfs. For larger, hotter stars however, nothing prevents fusion cycles from advancing to that producing ^{56}Ni ash, which then decays to ^{56}Fe. This isotope has a very high binding energy per nucleon such that any higher temperatures brought on by contraction cannot ignite energetically favorable (or profitable) fusion reactions. Consequently, as these stars near the end of their lives, a short, two-week fusion cycle burns core silicon by successive alpha captures into an electron-degenerate iron core. In the Type Ia case, which is modeled as an accreating white dwarf in a binary system, accretion pushes the white dwarf to near the critical mass and ignites carbon fusion. In the core-collapse scenario, accretion of iron ash in the core from silicon burning also pushes the electron-degenerate iron core over its Chandrasekhar-limit, only now there are no fusion reactions that can stop a runaway collapse.

Efforts to model the core-collapse explosion divided the problem at this point, due to

the very different physics that takes place before and after this moment. Specifically, the accepted convention is to divide a pre-collapse phase from a collapse phase as the times before the in-fall velocity of the outer edge of the iron core is less than 1000 km/s [91]. This precise division allows modeling efforts on either side a fixed reference so that one may use the results of the other as initial/final conditions. More importantly for this text, the in-fall velocity that sets the boundary comes at a time when the typical core density is just below 10^{10}g/cm^3 and the core temperature is nearly 10^{10}K. Densities and temperatures below these rough values occur during the pre-collapse phase and necessitate detailed nuclear reaction networks in order to accurately account for the composition and energy budget [92]. Also, below these densities, scattering with electrons thermalizes the neutrino spectrum but, they otherwise escape easily so that neutrino emission is the principle mechanism of energy and entropy loss [93]. Above these densities, during the collapse phase, temperatures are such that matter enters nuclear statistical equilibrium so that detailed reaction networks for strong and electromagnetic interactions are no longer necessary [94]. Also, small neutrino-nucleus cross sections are overcome by rising densities. Neutrinos then become trapped in the core and it becomes necessary to track their detailed spectrum and momentum distribution [95].

It is difficult to summarize contemporary core-collapse modeling beyond these early works with a short text. This is largely due to the fact that observationally, core-collapse supernova exhibit diverse features, as mentioned above. The constraints therefore placed on core-collapse explosions are not nearly as narrow as in the Type Ia case, so that models address many different progenitors, progenitor masses and evolutionary lines. Nevertheless, one feature nearly all models have in common is their failure to robustly produce explosions. The particular cases of a $15M_{\rm solar}$ and $25M_{\rm solar}$ main-sequence progenitors, developed to roughly match the spectroscopy of SN1987a, are often taken as representative in the literature. For the simulations of the presupernova evolution from main-sequence, the one dimensional model of Weaver *et al.* [96] has been the basis of most works, yielding the familiar "onion-skin" structure of ashes from various fusion cycles leading up to the collapse. Models such as these are used as the initial conditions

for core-collapse simulations, though the subset of models developed to investigate nucleosynthesis and ejecta spectroscopy resort to adding "pistons" or "bombs" to the core to force explosion [91] (WW95). These methods are fine-tuned to reproduce observed features, like those of SN1987a [91]. During the mid-1990's, at the time of these works, inadequate treatment of presupernova neutrino transport was believed to be the culprit in the failed explosions. However, consistent treatments in one dimensional [97] and two dimensional [98] models failed to produce explosions as well. In light of these and other works, two outstanding candidates can possibly play the decisive role in the explosion; unknown features of neutrinos and/or their spectra or bona-fide three dimensional phenomena, such as angular momentum, magnetic fields, etc. Again, as in the case of Type Ia supernovae, the chapter will conclude below with a discussion of sensitivity studies that show electron-capture plays a significant role, particularly on the neutrino spectra.

2.4 Electron-Capture Rates in Stellar Interiors

At this point, it is necessary to discuss in detail the way in which electron capture is treated in nearly all supernova models. The seminal works of authors Fuller, Fowler and Newman [23–27], following the recognition of Bethe *et al.* [22] as to the importance of the GT giant resonance, were the first to formally tackle the problem of determining weak reaction rates in the electron-degenerate stellar interior. Fuller *et al.* addressed the two main features of the problem; the determination of the phase space available in the stellar environment for the weak reactions [23] and the determination of the associated nuclear matrix elements [23–25]. As an aside, Ref. [26] is concerned with interpolating between values in reaction rate tables provided in their earlier texts and Ref. [27] is an online publication of the final manifestation of the rates. So then, the last two references in the series are not primarily concerned with the physics of stellar weak rates. What follows in this section is a recapitulation of the results laid out in Ref. [23] *concerning the available phase space.* The intent here is to par down the notation, generality and rigor of their derivation and simply show the reader the basic physical origin of continuum electron-

capture's rate sensitivity to the specific distribution of GT-strength in the daughter.

The total electron capture rate λ of a given nuclear species is the sum of rates from each initial state in the parent to each final state in the daughter

$$\lambda = \sum_i \sum_j \lambda_{ij}. \tag{2.1}$$

The individual decay rates, be they electron or positron emissions or captures, each have two principle ingredients; the nuclear matrix element of the transition and phase-space volume available. They are related to the individual decay rates λ_{ij} of the $i^{\underline{\text{th}}}$ parent state and the $j^{\underline{\text{th}}}$ daughter state as [23]

$$\lambda_{ij} = \ln 2 \frac{f_{ij}(T, \rho, U_{\text{F}})}{(ft)_{ij}}, \tag{2.2}$$

where the comparative half-life $(ft)_{ij}$ is a function of the reduced operator strengths (reduced matrix elements),

$$ft = \frac{K}{g_{\text{V}}^2 B(\text{F}) + g_{\text{A}}^2 B(\text{GT})}, \tag{2.3}$$

and the phase-space integral $f_{ij}(T, \rho, U_{\text{F}})$ is an implicit function of the stellar temperature T, density ρ, and electron chemical potential U_{F}. The constants g_{V} and g_{A} are the vector and axial-vector coupling constants, respectively, of weak decay. The constant $K = 2\pi^3\hbar^7/m_{\text{e}}^2 c^4$. The general form of $f_{ij}(T, \rho, U_{\text{F}})$ is too cumbersome for the considerations presented here. The following form for $f_{ij}(T, \rho, U_{\text{F}})$ is for the particular case of continuum electron-capture, where the possibility of a degenerate (anti-) neutrino gas forming and of electrons forming ions/atoms are neglected [23],

$$f_{ij}(T, \rho, U_{\text{F}}) = \int_{w_l}^{\infty} w^2 (q_{ij} + w)^2 G(+Z, w) S_-(T, U_{\text{F}}(\rho)) dw. \tag{2.4}$$

Here $w = E_e/m_e c^2$ is the dimensionless total electron energy, $q_{ij} = Q_{ij}/m_e c^2 = (Q_{\text{g.s.}} + E_{\text{x}i} - E_{\text{x}f})/m_e c^2$ is the dimensionless reaction Q-value for capture from a parent state with excitation $E_{\text{x}i}$ to a daughter state with excitation $E_{\text{x}f}$, and $w_l = |q_{ij}|$ is the capture

threshold total energy, again in dimensionless form. The function $G(+Z, w)$ is related to the relativistic Coulomb barrier factor $F(+Z, w)$ which appears in the usual formulation of the β-decay phase-space integral (e.g. Ref. [99]). The specific relation is declared as $G(+Z, w) = (p/w)F(+Z, w)$ by Ref. [23], where $p = p_e/m_e c$ is the dimensionless electron momentum, and is chosen to exploit the ease with which $G(+Z, w)$ can be determined numerically. Actually, $G(+Z, w)$ does not differ from unity enough as to figure in this discussion significantly, so it is hereafter disregarded. The function $S_-(T, U_{\rm F}(\rho))$ is the Fermi-Dirac distribution of electrons in the stellar plasma,

$$S_-(T, U_{\rm F}(\rho)) = \frac{1}{e^{(U - U_{\rm F}(\rho))/k_{\rm B}T} + 1}, \tag{2.5}$$

where $U = (w-1)m_e c^2$ is the electron kinetic energy less it's rest mass and $U_{\rm F}$ the electron chemical potential less it's rest mass. The chemical potential $U_{\rm F}$ here differs from the usual notion, associated with the symbol μ_e. This is to denote the extreme difference between the non-interacting Fermi gas, the degeneracy of which is parameterized by $\mu_e/k_{\rm B}T$ for comparatively cold, rarefied environments. In the stellar interior however, the electron Fermi-motion is relativistic and the electrons in the gas interact strongly via pair-production. Fuller *et al.* [23] determines the appropriately corrected stellar chemical potential as $U_{\rm F} = m_e c^2 \sqrt{1.02 \times 10^{-4}(\rho/\mu_e)^{2/3} + 1} - m_e c^2$. Note that in this expression μ_e is molecular weight, not chemical potential.

Now that all the ingredients have been outlined, the sensitivity of the electron-capture rate to the daughter B(GT$_+$) distribution is discussed, with the caveat that only capture on the parent ground state is considered explicitly. This is due mainly because what will be stated below holds true for any parent state. This is also due to the fact that in Chapter 7 the formalism described here is used to calculate the electron-capture rate on ^{64}Zn from the B(GT$_+$) measured in ^{64}Cu which of course, can only represent captures from the ^{64}Zn ground state. Dropping the index i, setting $G(+Z, w) \approx 1$ and denoting $W(q_j, w) \equiv w^2(q_j + w)^2$, the total electron-capture rate on the parent ground state is,

$$\lambda_{\text{g.s.}} = \frac{g_{\text{A}}^2/g_{\text{V}}^2}{K/g_{\text{V}}^2} \sum_j B_j(\text{GT}_+) \int_{w_l}^{\infty} W(q_j, w) S_-(T, U_{\text{F}}(\rho)) dw. \tag{2.6}$$

Clearly, the contribution of a given final state to the total rate is proportional to the final state's $\text{B}(\text{GT}_+)$ however, this is modulated by the size of the phase-space integral. Investigating the integral, the integrand in Equation 2.6 has two terms:

1. A statistical factor $W(q_j, w) = w^2(q_j + w)^2$ which results from the density of available electron states from which to capture; and

2. A quantum factor $S_-(T, U_{\text{F}}(\rho))$ describing the filling of available electron states.

The statistical factor $W(q_j, w)$ arises from evaluation of the density of states when deriving Equation 2.4 from Fermi's Golden Rule in the *allowed* approximation. When integrated, it is essentially responsible for the manifestation of the Sargent's Rule in β-decay, namely that phenomenologically the decay rates roughly go as $\lambda \propto Q^5$. Since increasing excitation energy in the daughter nucleus corresponds to decreasing reaction Q-value ($E_{\text{x}} = Q_{\text{g.s.}} - Q_{\text{react}}$), this factor has its largest value for an electron-capture to the daughter ground state. For daughter excited states, its value drops quickly with increasing excitation energy in the daughter nucleus. This factor acts as a weighting function in the integrand of Equation 2.6, lending stronger influence to lower-lying states in the daughter on the overall capture rate.

The quantum factor $S_-(T, U_{\text{F}}(\rho))$, the Fermi-Dirac distribution of degenerate electrons in the stellar interior, is the only term through which the stellar conditions influence the capture rate for an individual initial state. The stellar temperature also affects the population of parent excited states, but this is typically unimportant for temperature below $\sim$1 MeV. In the zero-temperature limit, $S_- = 1$ up to the electron kinetic energies equal to the chemical potential U_{F} and $S_- = 0$ for higher energies. Consequently, $S_-(T, U_{\text{F}}(\rho))$ acts as a low-pass filter upon the daughter $\text{B}_j(\text{GT}_+)$ spectrum. Regardless of how large the $\text{B}(\text{GT}_+)$ may be for the $j^{\underline{\text{th}}}$ final state, if the state lies at an excitation energy above $U_{\text{F}} + m_e c^2$, it is energetically inaccessible and cannot contribute to the total

capture rate.

The interplay of the two terms $W(q_j, w)$ and $S_-(T, U_{\rm F}(\rho))$ under varying stellar conditions accounts for the sensitivity of the electron-capture rate. At lower electron densities, for instance at or below 10^7g/cm^3, $U_{\rm F} + m_e c^2$ is a fraction of an MeV or less and typical temperatures are such that $k_{\rm B}T$ is also a fraction of an MeV. Therefore, $S_-(T, U_{\rm F}(\rho))$ tends to be a hard cut-off in the relevant B(GT$_+$) spectrum and high densities of GT states around and below an MeV of excitation in the daughter can lead to large temperature sensitivity in the capture rate. The weighting affect of $W(q_j, w)$ in the integrand of Equation 2.6 magnifies the affect of any discrepancies in the low-lying GT-spectrum on the capture rate. At higher densities, near 10^{10}g/cm^3, the Q-window created by $U_{\rm F} + m_e c^2$ is around 5 MeV and though $k_{\rm B}T$ is often about an MeV, the temperature sensitivity of the capture rate at these densities is significantly reduced. This is largely due to the weighting effect of $W(q_j, w)$ which tends to make the rate insensitive to GT-states above $U_{\rm F} + m_e c^2$, despite being energetically accessible due to thermal smearing of the electron Fermi surface.

2.5 Electron-Capture Influences in Supernovae

The third factor in the electron capture rate of course is the daughter B$_j$(GT$_+$) spectrum. Recall however, that the term $S_-(T, U_{\rm F}(\rho))$ in Equation 2.6 creates a "Q-window", restricting the reaction to that possible by available electron energies. Under terrestrial conditions, this term must be replaced to describe a very different, very rarefied electron environment (probably with atomic electrons), which greatly restricts access to daughter states. Therefore, if one includes consideration of thermally populated parent states, there are many transitions accessible in the stellar environment that are unmeasurable terrestrially. Faced with this large number of unknown GT matrix elements, Fuller *et al.* [23–25] used measured matrix elements and properties from mirror decays under isospin symmetry where possible. Otherwise, matrix elements were either 1) taken from large-scale shell-model calculations (e.g. [100]); 2) calculated on an independent particle

(IPM) shell-model basis [23], or 3) assigned an average matrix element gleaned from nuclei with similar masses. This determination was made for *sd*-shell nuclei ($17 \leq A \leq 40$). The same authors later applied the same considerations up to mass $A = 60$ [24, 25]. The resulting $B_j(GT_+)$ spectrum for an electron-capture daughter has two main parts: the low-lying transitions which are mostly measured states, and the GT giant resonance lying at several MeV excitation in most *sd*-shell nuclei.

It was understood by Fuller *et al.* and collaborators that neglecting the residual interaction between nuclei within a major shell was not necessarily a good approximation [44]. Indeed, the inclusion of the residual interaction in shell-model Monte-Carlo calculations, starting with the work in Ref. [101], moves the centroid of the GT giant resonance, usually to higher excitation, and fragments its strength over many individual, weaker states. Furthermore, excitations from single-particle states outside a major shell lead to a sizable, universal quenching of the B(GT) of $(0.74)^2$ [102]. Currently, calculations of the B(GT) using large-scale shell-model diagonalization and residual interactions, performed specifically for supernovae studies, are available up to mass $A = 63$ [103] using the KB3G pf-shell effective interaction [52]. In general, the effect of these new calculations of $B(GT_+)$ is reduce the electron-capture rate relative to the rates of FFN. This is due to application of the universal quenching factor to low-lying states determined by calculation and the shift of the GT giant resonance to higher excitation energy, further from the stellar Q-window.

As mentioned above, the Type Ia explosion dynamics sensitively depend on, among other things, the central ignition density, which in turn depends on the central electron fraction Y_e [89]. The central electron fraction is, in part, constrained by electron capture. The primary site of electron capture in the Type Ia explosion is in the narrow (10^{-4}cm) flame front, where respective temperatures and densities of 10^{10}K and 10^{10}g/cm^3 are possible. This flame front leaves in its wake a body of nuclear ashes, the composition of which is influenced by electron captures. This is significant since it is this material which is ejected by the explosion and its composition determines the decay light curve and spectral emissions of the Type Ia event.

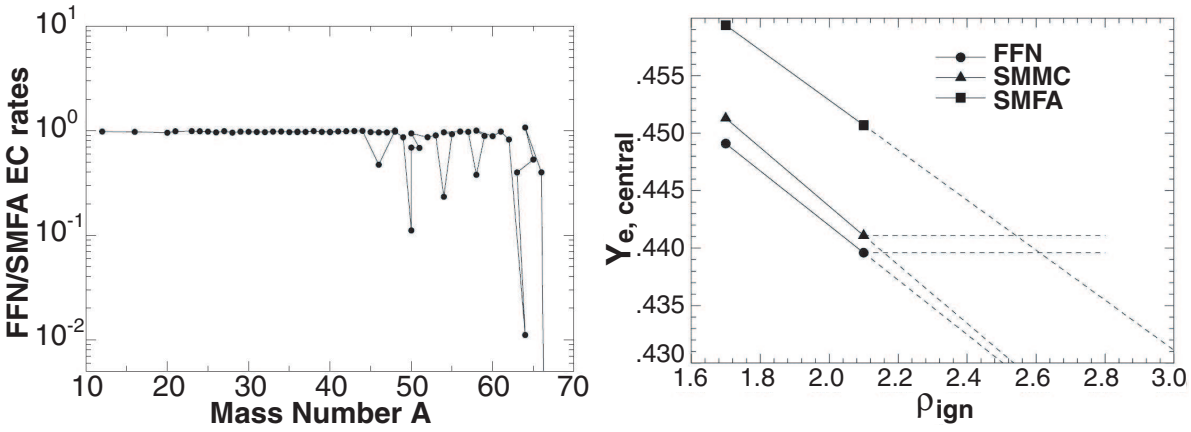

Figure 2.1: (Left) The isotopic abundance of ejecta from a model Type Ia explosion using electron-capture rates modified by shell-model calculations and normalized to that produced with FFN rates [104]. (Right) Reproduced from Ref. [3], the central electron fraction plotted as a function of central ignition density, resulting from using FFN rates (circles) and rates modified by shell-model calculations (squares). The third curve (triangles) are with bare shell-model Monte-Carlo rates (see discussion in Ref. [105]).

Brachwitz *et al.* [3] have carried out a sensitivity study investigating the effect of replacing the electron-capture rates of Fuller *et al.* with shell-model modified rates [105]. Their main result is displayed in Figure 2.1, showing significant changes to Type Ia nucleosynthesis (left) and the central ignition density for the white-dwarf progenitor (right). In Figure 2.1 (left), the isotopic abundance of modeled Type Ia ejecta is plotted as a function of mass number and normalized to that of FFN. The reduced electron-capture rates, due to the shell-model $B(GT_+)$ distributions, lead to reduced synthesis of iron-group elements. This is particularly so of those isotopes which are the electron-capture daughters of $odd-odd$ parent nuclei, cases which are particularly challenging for shell-model theory. Examples are seen in Figure 2.1 (left), where large deviations from FFN above $A = 50$ are, for example that of ^{50}Ti, ^{54}Cr, ^{58}Fe, and ^{64}Ni. In Figure 2.1 (right), the central electron fraction is plotted as a function of central ignition density. The important comparison is between the effect of the standard FFN rates (circles) and the shell-model modified rates (squares). For a given central electron fraction, projecting these two curves onto the abscissa shows a $\sim$25% difference in the inferred central ignition density.

Hix *et al.* [4] and Langanke *et al.* [106] have carried out a similar sensitivity study for

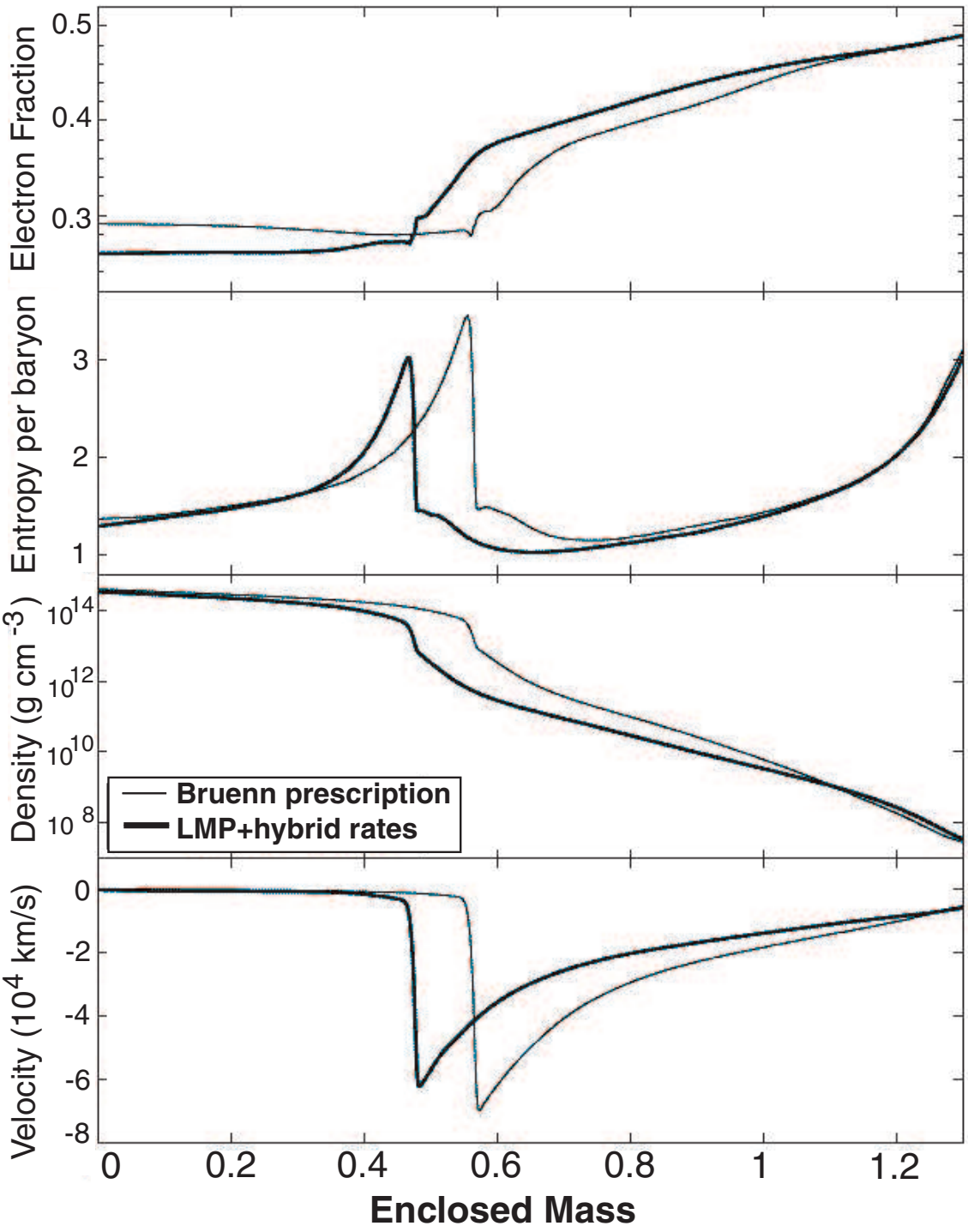

Figure 2.2: Reproduced from Ref. [4], from top to bottom, the electron fraction, entropy per baryon, density and velocity of core material for a $15M_{\rm solar}$ core-collapse explosion immediately after bounce. The lighter lines are profiles determined using the Bruenn prescription for electron-capture [95], the darker that of LMP+hybrid rates (see discussion in [4]).

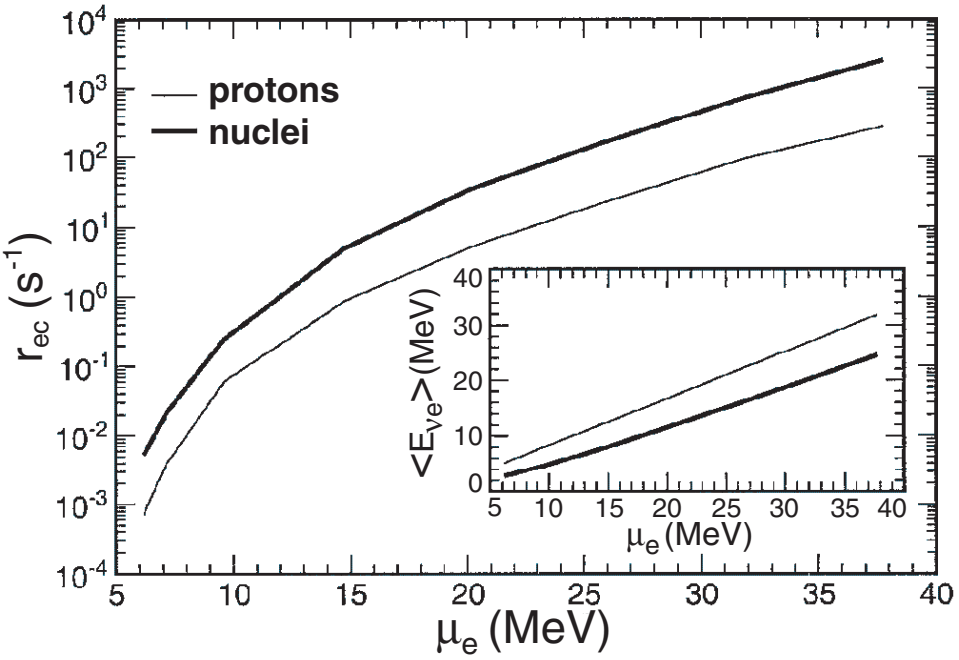

Figure 2.3: Reproduced from Ref. [106], the electron capture rate on protons (light curve) and on nuclei (dark curve) plotted as a function of electron chemical potential. In the inset, the average neutrino energy plotted as a function of electron chemical potential, again for captures on free protons and nuclei.

a $15M_{\rm solar}$ core-collapse scenario under the approximation of spherical symmetry. Figure 2.2 shows the main results presented in Ref. [4]. Here, the Bruenn parameterization for electron-capture rates [95] is compared to those resulting from large-scale shell model calculations. The noteworthy features of the Bruenn parameterization are that it treats electron-capture only on an average heavy nucleus $< A >$, determined from the equation of state, and assigned a single B(GT$_+$) value based on a generic $0f_{7/2} \rightarrow 0f_{5/2}$ transition. Furthermore, for nuclei with neutron number above 40, it assigns no B(GT$_+$) and therefore no electron-capture rate. The result of replacing this method with shell-model B(GT$_+$)s for each isotope is an overall reduction in the total capture rate in lower density regions and particularly during the in-fall phase, where captures on nuclei are mostly on those with $N < 40$. This is similar to the reduction seen in Ref. [3] for the thermonuclear Type Ia explosion, where the densities and temperatures are comparable. However, at higher densities and closer to the core center, captures on nuclei occur on species with masses up to and perhaps higher than $A \sim 120$. The overall result, seen in Figure 2.2, is

that the electron fraction below the shock is lower and more matter remains above the shock front, making successful explosion less likely. Because the matter at higher altitudes underwent less captures, it is less neutronized, lowering the entropy, density and in-fall velocity of the material above the shock. The net effect is that a weaker shock wave resulting from the shell-model rates, climbs as high into the outer core as the stronger shock wave produced under the Bruenn prescription [4].

Another important result from the same study is reported in Ref. [106], one of the results of which is displayed in Figure 2.3. Here, in the main panel, the individual capture rates are multiplied by their respective parent abundances showing that, over all values of the electron chemical potential that might be sampled by the core-collapse trajectory, the capture rate is dominated by captures on nuclei. In the inset, the average neutrino energy as emitted from captures on protons and nuclei is displayed. The contrast setup by these two plots is that at any given time in the collapse, though the energy of neutrinos emitted from captures onto protons is $\sim$20% greater, the production rate from captures onto nuclei is nearly an order of magnitude higher. Therefore, the correct neutrino luminosity, energy and angular momentum spectrum, for the collapse, bounce and post-bounce phases, will require knowledge of the detailed B(GT$_+$) in capture daughters [106].

In summary, the observational history of supernovae has been reviewed. The resulting taxonomy corresponds with two different major classes of progenitor, the near Chandrasekhar-mass white dwarf and a massive star with $M > 8M_{\rm solar}$, each involving different physics and theoretical challenges. One common element between them and an ingredient that plays an important role in each event's nucleosynthesis yields and explosion dynamics is nuclear electron capture. The formalism for calculating the capture rate in the electron-degenerate environment has been reviewed, with particular emphasis on the origin of the rate sensitivity. It is seen that the phase-space volume and Q-window created by the electron chemical potential make the low density electron capture rate sensitive to the particular distribution of B(GT$_+$) in the capture daughter. The effect of different methods for determining B(GT$_+$) in capture daughters on explosion models [3, 4, 106] provides a strong motivation for measuring the B(GT$_+$) directly with

charge-exchange reactions. It can not be stressed enough though, that the vast majority of GT transitions, particularly those stemming from parent excited states, will remain unmeasurable and can only be provided by theory. However, experimentally accessible $B(GT_+)$ distributions will aid the development of theoretical work by offering comparative benchmarks at the measurable cases. Theoretical methods that reproduce these $B(GT_+)$ distributions will enjoy increased confidence in their ability to reliably determine transitions that cannot be measured. To this end, the remainder of the text will be concerned with the measurement of $B(GT_+)$ in the upper pf-shell nucleus ^{64}Cu via the ^{64}Zn(t,^{3}He) charge-exchange reaction. This nucleus is potentially relevant to Type Ia and core-collapse scenarios however, it is more important as a stringent test of the shell-model at the high-A end of the pf-shell.

Chapter 3

Theoretical Techniques

Motivated by the astrophysical importance of determining B(GT_+) in nuclei, this chapter now bridges the gap between nucleus-nucleus scattering measurements and the GT operator strength via direct reaction theory. The emphasis is on developing simple, physically motivated, and case-specific theoretical tools to facilitate the analysis of the ^{64}Zn(t,^{3}He)^{64}Cu charge-exchange reaction, in order to determine B(GT_+) in ^{64}Cu. The main considerations of Taddeucci *et al.* [32] are reviewed, where they express an empirical proportionality between the differential reaction cross section in the limit of vanishing momentum transfer, and B(GT). Alongside the discussion below, the single transition to the ^{12}B g.s. via the ^{12}C(t,^{3}He) reaction is provided as an example. This is also useful in later chapters concerning the data analysis, where data from the ^{12}C(t,^{3}He) reaction is used for calibration purposes.

Two important caveats within the work of Ref. [32], apart from achieving the vanishing momentum transfer limit in the data analysis, provide the main burdens for this chapter. First, their work is only concerned with the nucleon-nucleus (N-nucleus) interaction for the (p,n) probe, but the present work uses the composite (t,^{3}He) probe. Many-body wavefunctions are needed for all particles involved, as well as single-particle binding energies and one-body transition densities for target and probe systems. More importantly, an effective nucleon-nucleon (NN) interaction must be supplied, as part of a double-folding procedure over these transition densities, to account for the composite

nature of the probe in the reaction. Secondly, the proportionality expressed in Ref. [32] applies specifically to the partial differential cross section associated with a transfer of total orbital angular momentum in the target system of $\Delta L = 0$. However, neither the (p,n) or (t,^{3}He), nor any other hadronic probe, is intrinsically selective of this quantum number change. Therefore, the result of the aforementioned double-folding procedure, a many-body form factor, is treated in the distorted-wave Born approximation (DWBA) in order to determine the kinematics and distortion, including Coulomb effects. Partial differential cross sections for various ΔL values are calculated. These are then available as fitting functions for a multipole decomposition analysis (MDA), whereby the $\Delta L = 0$ contributions to excitations measured in the ^{64}Zn(t,^{3}He)^{64}Cu reaction can be separated from larger transfers. As an additional resource, the DWBA calculations are repeated for every state predicted by large-scale shell-model calculations, using pf-shell effective interactions KB3G [52] and GXPF1a [107], in order to study forces that break the proportionality of Ref. [32] for the ^{64}Zn(t,^{3}He) case.

3.1 Born Series

First, consider a simple review of the Born-series expansion for scattering of plane waves, which begins with the assumption that the solution to the time-independent Schrödinger equation ψ_{total} should have the form:

$$\psi_{\text{total}} = \psi_{\text{incident}} + \psi_{\text{scattered}}. \tag{3.1}$$

If there exists a region far from the beam source for the interaction site(s) and a separate region r far from the interaction region R such that $r \gg R$, then in the later region the asymptotic condition may be imposed that total solution take the form

$$\psi(\mathbf{r} \to \infty) = e^{i\mathbf{k}\cdot\mathbf{r}} + f(\mathbf{k}, \mathbf{k'})\frac{e^{ikr}}{r}, \tag{3.2}$$

where the incident beam is approximated as having exactly defined momentum $\mathbf{p} = \hbar\mathbf{k}$

(plane wave) and the scattered waves with momenta $\hbar\mathbf{k}'$ are spherical, though modulated in intensity as a function of direction by the *scattering amplitude* $f(\mathbf{k}, \mathbf{k}')$. The differential cross section is defined as it's square-modulus, $d\sigma/d\Omega = |f|^2$. For scattering of this kind from a potential V, the Hamiltonian H of the Schrödinger equation $H\psi = E\psi$ can be split so that

$$[H_0 + V(\mathbf{r})]\psi(\mathbf{r}) = E\psi(\mathbf{r}), \tag{3.3}$$

where $H_0 = -(\hbar^2/2\mu)\nabla^2$ affects the free propagation for a system of reduced mass μ. It is important to remember that ψ here doesn't describe a bound state. The energy here is a eigenvalue, forming a continuous spectrum, and is set by the incident beam $E = \hbar^2 k^2/2m$. Using the given expressions for E and H_0 and regrouping terms, one obtains

$$[\nabla^2 + k^2]\psi(\mathbf{r}) = \frac{2\mu}{\hbar^2}V(\mathbf{r})\psi(\mathbf{r}), \tag{3.4}$$

which has the form of the Helmholtz equation in classical electrodynamics. Equation 3.4 is solved by the method of Green's function, where for a linear operator $\widehat{D}$, acting such that $\widehat{D}\psi(\mathbf{r}) = \rho(\mathbf{r})$, the Green's function $G(\mathbf{r}, \mathbf{r}')$ is defined as

$$\widehat{D}G(\mathbf{r}, \mathbf{r}') = \delta(\mathbf{r} - \mathbf{r}'), \tag{3.5}$$

and the solution $\psi(\mathbf{r})$ is

$$\psi(\mathbf{r}) = \phi(\mathbf{r}) + \int d\mathbf{r}' G(\mathbf{r}, \mathbf{r}')\rho(\mathbf{r}'). \tag{3.6}$$

The function $\phi(\mathbf{r})$ is the homogeneous solution, such that $\widehat{D}\phi(\mathbf{r}) = 0$. Taking $\widehat{D} = \nabla^2 + k^2$ in Equation 3.5 and performing a Fourier transform gives two solutions for $G(\mathbf{r}, \mathbf{r}')$ (after some integration),

$$G_\pm(\mathbf{r}, \mathbf{r}') = -\frac{e^{\pm ik|\mathbf{r}-\mathbf{r}'|}}{4\pi|\mathbf{r} - \mathbf{r}'|}. \tag{3.7}$$

The full solution then is

$$\psi_{\pm}(\mathbf{r}) = \phi_{\pm}(\mathbf{r}) - \frac{1}{4\pi}\int d\mathbf{r}' \frac{e^{\pm ik|\mathbf{r}-\mathbf{r}'|}}{|\mathbf{r}-\mathbf{r}'|}\rho(\mathbf{r}'). \tag{3.8}$$

Applying the asymptotic condition stated earlier, $|\mathbf{r}-\mathbf{r}'| = \sqrt{r^2 - 2\mathbf{r}\cdot\mathbf{r}' + r'^2}$ which is approximately $r\sqrt{1-2\mathbf{r}\cdot\mathbf{r}'/r^2}$, is valid and the solution becomes

$$\psi_{\pm}(\mathbf{r}) \rightarrow \phi_{\pm}(\mathbf{r}) - \frac{1}{4\pi}\int d\mathbf{r}' \frac{e^{\pm ikr}}{r} e^{\mp i\mathbf{k}'\cdot\mathbf{r}'}\rho(\mathbf{r}') \tag{3.9}$$

$$\rightarrow \phi_{\pm}(\mathbf{r}) - \frac{1}{4\pi}\frac{e^{\pm ikr}}{r}\int d\mathbf{r}' e^{\mp i\mathbf{k}'\cdot\mathbf{r}'}\rho(\mathbf{r}'). \tag{3.10}$$

Comparing to the expected asymptotic form in Equation 3.2, the plane wave form taken as the incident part of the solution satisfies the homogeneous equation $[\nabla^2 + k^2]e^{i\mathbf{k}\cdot\mathbf{r}} = 0$ and the other term has the spherical form $e^{\pm ikr}/r$, where $\rho(\mathbf{r}') = 2\mu/\hbar^2 V(\mathbf{r}')\psi(\mathbf{r}')$. Therefore, the scattering amplitude is

$$f(\mathbf{k},\mathbf{k}') = -\frac{\mu}{2\pi\hbar^2}\int d\mathbf{r}' e^{\mp i\mathbf{k}'\cdot\mathbf{r}'} V(\mathbf{r}')\psi(\mathbf{r}'), \tag{3.11}$$

where $\psi(\mathbf{r}') = e^{i\mathbf{k}\cdot\mathbf{r}'} + f(\mathbf{k}',\mathbf{k}'')e^{ik'r'}/r'$. Its recurring substitution into Equation 3.11 generates the Born-series. The usual Born Approximation is to truncate the series to the leading term produced by the first substitution, so that the scattering amplitude is

$$f(\mathbf{k},\mathbf{k}') \approx -\frac{\mu}{2\pi\hbar^2}\int d\mathbf{r}' e^{\mp i\mathbf{q}\cdot\mathbf{r}'} V(\mathbf{r}'), \tag{3.12}$$

where $\mathbf{q} = \mathbf{k}' - \mathbf{k}$ is the momentum transfer. The above expression is something like a transition matrix element T_{fi} of the interaction $V_{fi} = V(\mathbf{r}')$ in the basis of plane wave states ($\mathbf{k}$,$\mathbf{k}'$). For multiple scattering centers in the interaction region, located by the set $\{\mathbf{r}_a\}$, this can be generalized with the substitution $V(\mathbf{r}') \equiv \langle\Phi_{\mathrm{F}}|\sum_a V_a(\mathbf{r}'-\mathbf{r}_a)|\Phi_{\mathrm{I}}\rangle$, so that the full scattering amplitude is the sum of a terms called *form-factors*,

$$f(\mathbf{k},\mathbf{k}') \approx -\frac{\mu}{2\pi\hbar^2}\sum_a \left\langle \Phi_{\rm F}\middle| e^{\mp i\mathbf{q}\cdot\mathbf{r}_a}\int d\mathbf{r}' e^{\mp i\mathbf{q}\cdot(\mathbf{r}'-\mathbf{r}_a)}V_a(\mathbf{r}'-\mathbf{r}_a)\middle|\Phi_{\rm I}\right\rangle. \tag{3.13}$$

The target-residue wavefunctions $\Phi_{\rm I}$ and $\Phi_{\rm F}$ are the solutions to their respective internal Hamiltonians. The procedure for evaluating this scattering amplitude is often called a *single-folding* procedure, accounting for the composite nature of the target by "folding" or integrating over the contribution of all two-body interactions V_a. For a composite projectile, the incident and scattered plane waves are replaced by wave function solutions of their own internal Hamiltonians. The sum is changed as $a \rightarrow a, b$, a double-sum over the target and projectile internal coordinates, and the set $V_{a,b}$ then represents all two-body interactions between all the individual constituents. Determination of the scattering amplitude in this case is likewise called a *double-folding* procedure.

These simple considerations provide a nice framework to discuss the more complex case of nucleus-nucleus scattering. What follows is not an attempt to rigorously derive the general form of the transition matrix T_{fi} for nuclear reactions. Instead, the aim is to show in simple terms where the various nuclear structure and effective interaction ingredients enter into the calculation of the differential cross section, first reviewing the more basic work of Taddeucci *et al.* [32], then reviewing the inputs for calculations performed in the present work.

3.2 A General Proportionality Between Cross Section and B(GT)

In their construction of an effective interaction $V_{\rm eff}$, Love and Franey [2, 31] expanded a general form of the bare NN-interaction V_{ij} in coefficients of Yukawa functions. They then fit the ranges R of the Yukawa functions to data on NN-scattering amplitudes at various bombarding energies. This will be discussed in greater detail below. For the present, their work provides a starting point for a discussion of the proportionality be-

tween charge-exchange differential cross sections and Gamow-Teller strength laid out by Taddeucci *et al.* [32]. The form of the free NN-interaction contains central (C), spin-orbit (LS) and tensor (T) terms,

$$V_{ij}(r_{ij}) = V^C(r_{ij}) + V^{LS}(r_{ij})\mathbf{L}\cdot\mathbf{S} + V^T(r_{ij})S_{ij}(r_{ij}), \tag{3.14}$$

where $\mathbf{L}\cdot\mathbf{S}$ is the total spin-orbit operator of the nucleus. The tensor operator S_{ij} is

$$S_{ij}(r_{ij}) = 3\frac{(\hat{\sigma}_i\cdot\mathbf{r}_{ij})(\hat{\sigma}_j\cdot\mathbf{r}_{ij})}{r_{ij}^2} - \hat{\sigma}_i\cdot\hat{\sigma}_j, \tag{3.15}$$

where subscripts i, j refer to the $i^{\underline{th}}$ target nucleon and $j^{\underline{th}}$ projectile nucleon, respectively. Love and Franey's expansion in Yukawa terms $Y(r_{ij}/R) = e^{-r_{ij}/R}/(r_{ij}/R)$ and $r_{ij}^2 \times Y(r_{ij}/R)$, retaining only those with explicit spin-isospin dependence (since GT is under investigation) is

$$\begin{aligned} V_{\text{eff}} = \sum_{ij}\Bigg(&V_\tau^C Y(r_{ij}/R_\tau) + V_{\sigma\tau}^C Y(r_{ij}/R_{\sigma\tau})(\hat{\sigma}_i\cdot\hat{\sigma}_j) + V_\tau^{LS} Y(r_{ij}/R_{LS\tau})\mathbf{L}\cdot\mathbf{S} + \\ &+V_\tau^T r_{ij}^2 Y(r_{ij}/R_{T\tau})S_{ij}\Bigg)(\hat{\tau}_i\cdot\hat{\tau}_j). \end{aligned} \tag{3.16}$$

3.2.1 The (p,n) Reaction

In their exposition, Taddeucci *et al.* [32] rely on the similarities between operators in the effective NN interaction and operators in the theory of β-decay. Specifically, for the case of investigating B(GT) with the (p,n) probe, they reduce their consideration to the relevant term in the central isovector part of the effective interaction,

$$\sum_i V_{\sigma\tau}^{\mathrm{C}}(r_{ip})(\hat{\sigma}_i\cdot\hat{\sigma_p})(\hat{\tau}_i\cdot\hat{\tau_p}), \tag{3.17}$$

which is responsible for spin-flip transitions in the target-residual system. Here, $V_{\sigma\tau}$ includes the radial dependence of the interaction in terms of the relative coordinates r_{ip}, and σ and τ are the Pauli spin and isospin matrices respectively. The subscript p denotes the incident proton and i enumerates target nucleons. This is similar to the operator of Gamow-Teller transitions in $\beta^{\pm}$-decays,

$$g_{\mathrm{A}} \sum_i \sigma_i t_i^{\pm}. \tag{3.18}$$

For a target state Φ_I and residual state Φ_F, each with good total angular momentum $J_{I,F}$, calculating the corresponding reduced transition amplitude for this operator gives the operator strength

$$\frac{g_{\mathrm{A}}^2}{2\pi}\left(\frac{1}{2J+1}\right)\left|\sum_i \left\langle \Phi_F \middle|\middle| \sigma_i t_i^{\pm} \middle|\middle| \Phi_I \right\rangle\right|^2 = B(\mathrm{GT}_{\pm}), \tag{3.19}$$

where $\widehat{J} = \sqrt{2J+1}$. This is the strength for Gamow-Teller β-decay.

An operator sum-rule for the GT operator strength is also useful to define. Ikeda *et al.* [13] first defined a GT sum-rule in 1963, in conjunction with their theoretical prediction of the (p,n)-induced GTR. It is a non-energy weighted sum-rule and can be expressed as follows, where the sums are taken over the final states F of the daughter nucleus. Also, the sum-rule contributions from the isospin-lowering (GT_-) and isopsin-raising (GT_+) parts of GT operator are explicitly separated in the sum.

$$\sum_F B(\mathrm{GT}_-) - \sum_F B(\mathrm{GT}_+) = 3(N-Z). \tag{3.20}$$

Taking their difference, as shown in Equation 3.20, gives the simple result $3(N-Z)$. This result is understandable intuitively. When $N > Z$, the difference $(N-Z)$ expresses the number of occupied neutron configurations which have a corresponding, unoccupied proton configuration so that the β decay is not Pauli-blocked. The converse is true for inverse β decay when $N < Z$. The factor of 3 accounts for the spin degeneracy due to the fact that the GT operator also has a spin-flip component. The most remarkable

feature about this sum-rule is that it is essentially model-independent. Even though the sum-rule can be understood with a simple, independent-particle model description, it should remain strictly true, regardless of how or what kind of residual interactions are incorporated in a nuclear model. Likewise, this sum-rule should remain valid regardless of what kind of charge-exchange probe samples the GT-strength, provided internal structure effects are accounted for in the case of composite probes. Attaining the correct value for the sum-rule then is an important test of new charge-exchange probes and theoretical structure calculations testing new effective interactions. These points will be discussed in futher detail below.

Taddeucci *et al.* [32] take the limit of vanishing momentum transfer q and factor the expression for B(GT) in Equation 3.19 out of the calculation of the differential cross section, with the goal of expressing it in the linear form,

$$\left.\frac{d\sigma}{d\Omega}\right|_{q\to 0} = \widehat{\sigma}_{\mathrm{GT}} B(\mathrm{GT}). \tag{3.21}$$

In direct reaction theory [108, 109], the differential cross section is proportional to the transition matrix elements $\sum \left|T(M_F, M_I, m_p, m_n)\right|^2$. This is separate from exchange-effects, where real nucleon transfers lead to the same final state, which Taddeucci *et al.* treat in the impulse approximation as well with a Dirac-delta function potential. Taddeucci *et al.* express the direct part of T in the distorted-wave impulse approximation (DWIA), in accordance with Refs. [108, 109] as the nuclear transition t-matrix,

$$T \approx \int d\mathbf{r}\chi^*_-(\mathbf{r},\mathbf{k}')\big\langle n,\Phi_F\big|\sum_i V^{\mathrm{C}}_{\sigma\tau}(r_{ip})(1-P_{ip})(\hat{\sigma}_i\hat{\tau}_i)\cdot(\hat{\sigma_p}\hat{\tau_p})\big|\Phi_I,p\big\rangle\chi_+(\mathbf{r},\mathbf{k}), \tag{3.22}$$

where the permutation operator P_{ip} has been introduced into the operator of Equation 3.17 in such a way so as to allow $\sigma\tau$ terms of the proton p and each target nucleon i to be grouped together. Note that this expression is only valid for the $\Delta L = 0$ part of the differential cross section. Also, the action of the central-volume part of the bare

NN-interaction, mainly responsible for distortion, has been implicitly included in the distorted waves $\chi_{\pm}$.

In its momentum representation, Taddeucci *et al.* take these terms in T to be separately integrable: the volume integral over $V^{\mathrm{C}}_{\sigma\tau}(r_{ip})$, the target integral over $\sum_i(\hat{\sigma_i}\hat{\tau_i})$, the projectile integral over $(\hat{\sigma_p}\hat{\tau_p})$, and the distortion integral over $\chi^*_-(\mathbf{r},\mathbf{k'})\chi_+(\mathbf{r},\mathbf{k})$. They then make various simplifications, first by taking the limit of vanishing momentum transfer ($q \rightarrow 0$) on the first three terms. It's unnecessary to reproduce them in full here. Respectively, they lead the following expressions; for the volume integral $|J_{\sigma\tau}|^2$, for target integral the B(GT) in the target system, and for the projectile integral the B(GT) in the projectile system (which is just 3). The factoring of the differential cross section then gives for the proportionality constant in Equation 3.21,

$$\widehat{\sigma}_{\mathrm{GT}} = KN_D|J_{\sigma\tau}|^2, \tag{3.23}$$

where K is a kinematic factor in the reduced masses of the entrance and exit channels. The term N_D comes from the distortion integral, which Taddeucci *et al.* factor separately by treating the distorted waves $\chi^*_-(\mathbf{r},\mathbf{k'}), \chi_+(\mathbf{r},\mathbf{k})$ in the Eikonal approximation.

In the Eikonal approximation, the projectile and ejectile trajectories are straight lines. Alternatively, this approximation is enforced by preserving the parallel part of the momenta $\mathbf{k}$ and $\mathbf{k'}$. This is achieved in practice by separating the nuclear potential into optical (U) and structural (W) terms $V = U + W$ and solving for the distortion due to U by only allowing incident plane waves to be distorted in the plane perpendicular to the motion. Doing this allows Tadduecci *et al.* to arrive at an expression for N_D that commutes with the remaining integrals [32].

Tadduecci *et al.* were inspired by the empirical emergence of the proportionality relation [18] and test the validity of their approach by comparing back to a large body of (p,n) reaction data (see Ref. [32] and references therein). Figure 3.1, reproduced from Ref. [32], shows this comparison for their DWIA calculations. The dotted curve is for the unit cross section in a proportionality they express for the Fermi strength B(F) associated

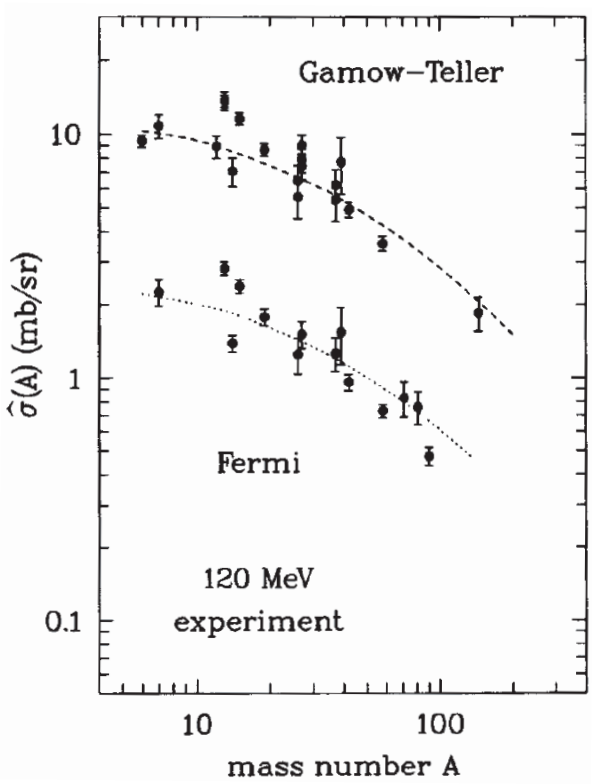

Figure 3.1: The (p,n) Fermi and Gamow-Teller unit cross sections, plotted as a function of target mass A, reproduced from Ref. [32].

with the pure isospin part $\tau_i\tau_p$ but, this is not relevant to this discussion. The dashed curve is for the GT unit cross section. In both cases, the DWIA calculations have not been normalized to the data. The scatter in the data, relative to the DWIA curve, for the GT unit cross section is $\Delta\widehat{\sigma}_{\rm GT}/\widehat{\sigma}_{\rm GT} = 22\%$. This is important since the average error in the overall normalization for the data points is only 8% and the scatter in their own calculations is not sufficient to account for the difference. Therefore, they conclude that among other possible affects, operators significantly different from the $\sigma\tau$ operator of β-decay must be responsible for breaking the proportionality of Equation 3.21.

In the development of similar proportionality relations for other charge-exchange probes, the above approximations and limitations to the proportionality of Equation 3.21 provide the basis. In summary, they are

1. This result is only valid for the partial cross section associated with $\Delta L = 0$ transitions. Analysis of measurements made with any probe must be able to

isolate this amplitude.

2. The reaction must take place under conditions such that it is well-described as a single-step transition.

3. The limit of small momentum-transfer allows one to factor B(GT) out of the radial terms in the cross section, valid for treating distortion in an Eikonal model. Experimentally, this necessitates extrapolating measurements to 0° scattering angle and reaction Q-value $Q_{\mathrm{react}} = 0$.

4. Exchange effects, where real nucleon transfer leads to the same final state, are significant. Taddeucci *et al.* finds that for (p,n) it doesn't break their proportionality, only reduces the cross sections uniformly. Nevertheless, to obtain absolute B(GT), exchange cannot be neglected and must be quantified for any new probe. It is certainly more complicated to treat in composite probes.

5. Love and Franey [2, 31] show, and Taddeucci *et al.* uses, that the $\sigma\tau$ operator is best isolated from other terms in the effective interaction at intermediate beam energies ($\gtrsim$100 MeV/nucleon). This result doesn't depend significantly on probe structure, so $\sigma\tau$ will be best isolated under this condition in general. The physical reason behind this is that the mass of the pion is roughly 140 MeV/c^2. Therefore, at the $\gtrsim$100 MeV/nucleon beam energy, the likelihood of one-pion exchange is maximized and likewise, the action of the $\sigma\tau$ operator is maximized.

3.2.2 The (^{3}He,t) and (t,^{3}He) Reactions

An investigation of a proportionality between differential cross section and B(GT) for the composite (^{3}He,t) charge-exchange probe at 140 MeV/nucleon [110] follows directly from these simpler considerations for the (p,n) reaction and is relevant for the present (t,^{3}He) work as well. Figure 3.2 (top panel) shows the value of the GT unit cross section as determined from forward-angle (^{3}He,t) scattering data (black), normalized isotope-by-isotope using B(GT$_-$) from states measured with β-decay. Clearly, a mass-dependent

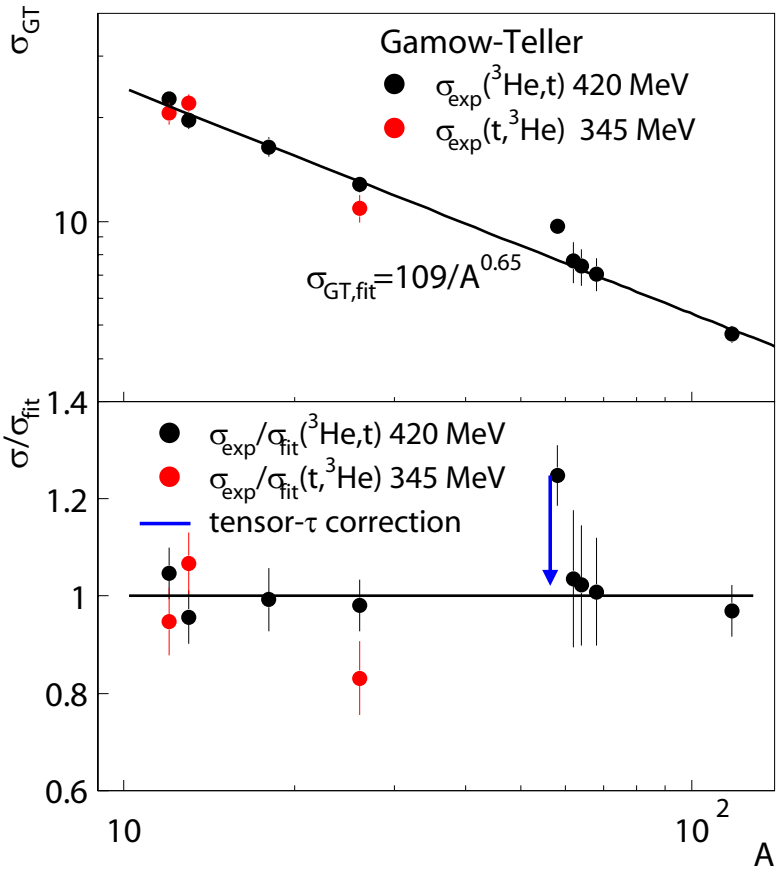

Figure 3.2: The (^{3}He,t) and (t,^{3}He) Gamow-Teller unit cross sections, plotted as a function of target mass A, based on Ref. [111].

relation between unit cross section and target mass exists:

$$\widehat{\sigma}_{\rm GT} = 109 \times A^{-0.65} \tag{3.24}$$

One major deviation in this trend is seen for the case of ^{58}Ni. In Figure 3.2 (bottom), the scatter in the value of $\widehat{\sigma}_{\rm GT}$ is plotted against the fitted trend. Deviations on the $\Delta\widehat{\sigma}_{\rm GT}/\widehat{\sigma}_{\rm GT}$ ~20% level are seen, as is the case for (p,n) in Ref. [32]. Treating the reaction in the DWBA and folding in the same effective NN interaction that Taddeucci *et al.* used [31], done here in a double-folding format to account for the composite nature of the probe, Cole *et al.* [112] show that contributions to the cross section from the tensor-τ part of the NN-interaction (V_τ^T) produce interference between the $\Delta L = 0$ GT amplitude and $\Delta L = 2$ amplitudes. The correction deduced from this study, shown in Figure 3.2 (bottom) with the blue arrow, works in the right direction and has the right

size to account for most of the deviation. Exchange effects for the (^{3}He,t) reaction were also studied [111, 112], to compare the effect of treating it exactly (e.g. [113]) or in the short-range approximation prescribed in Ref. [2]. In both references, the authors find the short-range approximation leads to an overall 40% reduction in the B(GT) but, it does not break the proportionality with cross section [111,112]. With this kind of study, which will be performed in Chapter 6 for the present ^{64}Zn(t,^{3}He) case, the effect of V_τ^T can be systematically isolated.

Additionally, measurements made using the (t,^{3}He) probe, as described in Chapter 4, to determine B(GT$_+$) in ^{12}B [112], ^{13}B, and ^{24}Na [8] have revealed a consistent trend for $\widehat{\sigma}_{\rm GT}$ (Figure 3.2 red). Since it appears that the (^{3}He,t) and (t,^{3}He) unit cross sections are consistent, the present work will rely on this for the analysis of ^{64}Zn(t,^{3}He) cross section data. In the following sections, the tools used to treat this reaction in the DWBA are discussed. This lays the groundwork for their use, in Chapter 6, in isolating $\Delta L = 0$ partial cross sections (MDA), extrapolating them to zero momentum transfer and estimating the size of tensor effects.

3.3 Radial Wavefunctions for (t,^{3}He)

First, to calculate cross sections, a set of realistic of projectile/ejectile and target/residue radial wavefunctions are calculated. This is done using the FORTRAN code WSAW, a subroutine of the FOLD code [114]. The radial behavior of each $|core> + |nucleon>$ system is described by solving for the nucleon radial distribution in Coulomb + Woods-Saxon, real and spin-orbit, potentials as follows

$$U(r) = V_{\rm C}(r) + V_o(r) + \mathbf{l}\cdot\mathbf{s}V_{\rm SO} \tag{3.25}$$

where the Coulomb potential is

Part.	Model	$E_{\rm b}$(MeV)	V_o(MeV)	V_{SO}(MeV)	$r_{o,C}$(fm)	a_o(fm)
t	$d+n(0s_{1/2})$	6.257	52.361	7.000	1.25	0.65
^3He	$d+p(0s_{1/2})$	5.490	52.259	7.000	1.25	0.65
^{12}C	$^{11}B+p(0p_{3/2})$	11.971	59.015	7.000	1.25	0.65
	$+p(0p_{1/2})$	5.869	50.522	7.000	1.25	0.65
^{12}B	$^{11}B+n(0p_{3/2})$	11.660	53.715	7.000	1.25	0.65
	$+n(0p_{1/2})$	6.160	45.794	7.000	1.25	0.65
^{64}Zn	$^{63}Cu+p(0f_{7/2})$	9.473	58.549	7.000	1.25	0.65
	$+p(0f_{5/2})$	3.105	51.881	7.000	1.25	0.65
	$+p(1p_{3/2})$	4.913	56.919	7.000	1.25	0.65
	$+p(1p_{1/2})$	2.924	54.677	7.000	1.25	0.65
^{64}Cu	$^{63}Cu+n(0f_{7/2})$	15.479	53.644	7.000	1.25	0.65
	$n(0f_{5/2})$	9.198	46.926	7.000	1.25	0.65
	$n(1p_{3/2})$	10.801	51.332	7.000	1.25	0.65
	$n(1p_{1/2})$	8.917	49.184	7.000	1.25	0.65

Table 3.1: Parameters used to calculate radial wavefunctions with the code WSAW [114], modeled using volume + spin-orbit Woods-Saxon and Coulomb potentials.

$$\begin{aligned} V_{\rm C}(r) &= \frac{e^2 Z_{\rm nucleon} Z_{\rm core}}{r} \quad \text{for} \quad r > r_{\rm C} A^{1/3} \\ &= \frac{e^2 Z_{\rm nucleon} Z_{\rm core}(3 - r^2/(r_{\rm C}^2 A^{2/3}))}{2 r_{\rm C} A^{1/3}} \quad \text{for} \quad r < r_{\rm C} A^{1/3} \end{aligned} \tag{3.26}$$

and the Woods-Saxon volume and spin-orbit potentials are,

$$V_{o,SO}(r) = \frac{V_{o,SO}}{1 + e^{(r - r_{\rm o})/a_{\rm o}}} \tag{3.27}$$

where $r_{\rm c}$ is the Coulomb radius, $r_{\rm o}$ and $a_{\rm o}$ are the Woods-Saxon radius and diffusivenesses. The single-particle binding energies E_b are calculated using the DENS subroutine of OXBASH [50], employing the Sk20 Skyrme interaction [115]. This interaction is chosen because it can be used over a large mass-range. With it, consistency is maintained for calculations involving different targets. The volume WS depths V_o are allowed to vary so that the numerical determination of the radial wavefunction converges with the given binding energy. The calculations are summarized in Table 3.1.

3.4 One-Body Transition Densities

Next, one-body transition densities (OBTD) for the overlap of the projectile-ejectile and target-residue configurations are calculated. The OBTD is a quantity introduced to solve the problem of calculating the expectation of a single-particle operator in a representation with many-body wavefunctions. A simple example of this comes from the basic case above in Equation 3.13. There, the initial and final nuclear target states would be analogous to the $\Phi_{\rm I}$ and $\Phi_{\rm F}$ states respectively. However, the interactions V_a are between individual constituents. This is solved in nuclear shell-model calculations by expanding one-body transition operators of the kind $O(\mathbf{r})$ in terms of single-particle creation and annihilation operators,

$$\left\langle \Phi_{\rm F} \middle| O(\mathbf{r}) \middle| \Phi_{\rm I} \right\rangle = \left\langle \Phi_{\rm F} \middle| \sum_{i,f} \left\langle \phi_{\rm f} \middle| \widehat{O} \middle| \phi_{\rm i} \right\rangle \hat{a}_i^\dagger \hat{a}_f \middle| \Phi_{\rm I} \right\rangle \tag{3.28}$$

$$= \sum_{i,f} \left\langle \phi_{\rm f} \middle| \widehat{O} \middle| \phi_{\rm i} \right\rangle \left\langle \Phi_{\rm F} \middle| \hat{a}_i^\dagger \hat{a}_f \middle| \Phi_{\rm I} \right\rangle, \tag{3.29}$$

where the terms $\left\langle \Phi_{\rm F} \middle| \hat{a}_i^\dagger \hat{a}_f \middle| \Phi_{\rm I} \right\rangle = \rho_{if}$, are the *one-body transition densities*. They are Slater-determinants calculated in the occupation number representation of the shell-model wavefunctions $\Phi_{\rm I}$ and $\Phi_{\rm F}$. The one-body matrix elements $\left\langle \phi_{\rm f} \middle| \widehat{O} \middle| \phi_{\rm i} \right\rangle$ are calculated in the single-particle wavefunctions $\phi_{\rm i,f}$ which are the radial wavefunctions calculated in the previous section.

The OBTDs for the ^{12}C-^{12}B overlaps are calculated in the p-shell space with the CKII [116] effective interaction using the OXBASH code [50]. Those for the ^{64}Zn-^{64}Cu systems are calculated in the pf-shell space using both GXPF1a [53] and KB3G [52] effective interactions using the NuShellX code [51]. In both codes, the OBTDs are calculated by coupling to good total angular momentum and good isospin. Dependence on spatial orientation is removed by calculating the matrix elements in the reduced form via the Wigner-Eckhart theorem. They then have the form

$$\text{OBTD} = \frac{\left\langle \Phi_{\text{F}} \middle\| [\hat{a}_i^\dagger \otimes \hat{a}_f]_{\Delta J, \Delta T} \middle\| \Phi_{\text{I}} \right\rangle}{\sqrt{2\Delta J + 1}\sqrt{2\Delta T + 1}}, \tag{3.30}$$

where $[\hat{a}_i^\dagger \otimes \hat{a}_f]_{\Delta J, \Delta T}$ is an expansion in Clebsch-Gordan coefficients coupling all single-particle creation and annihilation operators to good angular momentum and good isospin.

Experimentally, it is known that only 50% to 60% of the Gamow-Teller (non-energy weighted) sum-rule (see Equation 3.20 and subsequent discussion) is exhausted below 20 MeV of excitation in the daughter nucleus [21]. This is an important point to make now, as shell-model calculations are discussed, because the quenching is likely due to admixture of configurations outside model spaces used here [44]. Recall from Chapter 1 that missing spin-flip strength at a low excitation lead to the first proposal of the giant GT states' existence [13]. Similarly, missing strength in the region of the giant GT state(s) has been attributed to various admixtures that further move strength to higher excitation. One possible mechanism is due to interference with 1p-1h configurations from 2p-2h admixtures (e.g. Ref. [117]). This has been experimentally verified in a few cases (see Ref. [111] and references therein). Another possibility is excitation of $\Delta(1232)$-isobar nucleon-hole states [118].

Experimentally, it has also been seen that the quenching is universal, meaning the reduction factor is independent of excitation energy. Consequently, structure calculations confined to a smaller model space i.e., ones not including unusual configurations like the ones mentioned above, can still be compared to data by simply applying the phenomenological quenching factor to their calculated GT strengths. The normal practice in this text will be to account for the quenching post-calculation by scaling B(GT) with the universal (averaged value over all target masses) quenching factor $\sim (0.74)^2$ [102, 112].

As an example, the OBTDs for the ground-state to ground-state transition of the ^{12}C(t,^{3}He)^{12}B reaction are shown in Table 3.2. For convenience in using them as inputs for the later steps in the calculation, they are expressed using the "Z-coefficient" convention of Raynal/ALLWORLD *et al.* [119, 120]:

ϕ_f	ϕ_i	$Z_{j,j'}^{\Delta J,\Delta T}$
$\pi(0s_{1/2})$	$\nu(0s_{1/2})$	0.707
$\nu(0p_{1/2})$	$\pi(0p_{1/2})$	0.07326
$\nu(0p_{1/2})$	$\pi(0p_{3/2})$	0.69147
$\nu(0p_{3/2})$	$\pi(0p_{1/2})$	0.32622
$\nu(0p_{3/2})$	$\pi(0p_{3/2})$	0.08220

Table 3.2: One-body transitions densities for ^{12}C to ^{12}B, ground state-to-ground state transition.

$$Z_{j,j'}^{\Delta J,\Delta T} = \frac{C(T_i, T_{im}, \Delta T, \Delta T_m | T_f, T_{fm})\sqrt{2\Delta T + 1}}{\sqrt{2J_i + 1}\sqrt{2T_f + 1}} \times \text{OBTD} \tag{3.31}$$

for Clebsch-Gordon coefficients C. The OBTDs for both the target-residue overlaps and the projectile-ejectile overlaps must be calculated. However, in the projectile-ejectile system of (t,^{3}He), the OBTD is unity since the single-particle radial wavefunctions $\phi_{i,f}(\mathbf{r})$ are essentially identical. It's entry in Table 3.2 then is just the leading coefficient in Equation 3.31.

3.5 Form Factors

The next step in calculating (t,^{3}He) differential cross sections is to calculate the relevant form factors. This is done using the code FOLD [114] which performs the double-folding procedure mentioned previously. In this procedure, the product of the OBTDs of the target-residue system and of the projectile-ejectile system is folded (integrated) over an effective nucleon-nucleon interaction V_{eff}. For both ^{12}C(t,^{3}He) and ^{64}Zn(t,^{3}He) reactions, the Love and Franey effective interaction [2, 31], fitted using data on NN-scattering amplitudes at 140 MeV/nucleon, is used in the folding procedure. The free NN-interaction contains central (C), spin-orbit (LS) and tensor (T) terms as stated earlier in Equation 3.14. Recall there the discussion, that in constructing an effective interaction, authors Love and Franey [2, 31] expand each term, using Yukawa functions $Y(r_{ij}/R)$ and $r_{ij}^2 \times Y(r_{ij}/R)$ as the expansion coefficients. The effective interaction is then fit to NN-

scattering data so as to reproduce the long-range behavior of the one-pion exchange potential (OPEP). For the (t,^{3}He) charge-exchange reaction that populates a Gamow-Teller state, only a specific term with explicit isospin dependence need be retained, such that the more general Equation 3.16 reduces to

$$V_{\text{eff}} = \sum_{ij} V_{\sigma\tau}^{C} Y(r_{ij}/R_{\sigma\tau})(\hat{\sigma}_i \cdot \hat{\sigma}_j)(\hat{\tau}_i \cdot \hat{\tau}_j), \tag{3.32}$$

where subscripts i, j refer to the $i^{\underline{th}}$ target nucleon and $j^{\underline{th}}$ projectile nucleon, respectively. The ranges R_X are the various fitted ranges, reported in tabular form by Love and Franey [2, 31], for each bombarding energy they investigated. In addition to the above form, an approximate treatment exchange interaction is also added. This is modeled in the zero-range approximation by taking exchange terms to be of the kind $V_{\text{exch}} = V_o\delta(\mathbf{r}_{ij})$ which may not be the most realistic option [113]. However, this choice greatly eases the computational difficulty, as it has an analytic Fourier transform and makes a very simple contribution to the form factors. Also, as mentioned above, the effect of this approximation is only to reduce the overall B(GT) by a common factor of about 40% [111, 112].

In summary, form factors for each relative angular momentum transfer ΔJ_R capable of coupling the initial and final J^π of projectile and target states must be calculated. In both cases with the ^{12}C and ^{64}Zn targets, only transitions from their ground states are calculated. Both are even-even nuclei so their ground states are $J^\pi = 0^+$. Charge-exchange excitation of Gamow-Teller states in their residues will then be $J^\pi = 1^+$ so in the target system, $\Delta J_{\text{tar}} = 1$. Assuming no excited states for the triton or ^{3}He particles, in the projectile system the angular momentum transfer is $\Delta J_{proj} = 1$. Adding these by the usual triangle inequality, the possible relative angular momentum transfers are $\Delta J_{\text{rel}} = 0, 1, 2$. However, $\Delta J_{\text{rel}} = 1$ violates conservation of parity, so the two form factors, associated with $\Delta J_{\text{rel}} = 0, 2$, are the only ones calculated.

3.6 Distorted Waves

The last remaining step in calculating the (t,^{3}He) differential cross section is to account for distortion to incident and outgoing projectile-ejectile waves. The Coulomb interaction has an infinite range so that assuming the interaction site is far from the beam source and $\phi(\mathbf{r})$ is a plane wave is not sufficiently accurate. Realistic incoming waves $\chi_{\pm}$are first distorted by the Coulomb and nuclear fields before interacting with the target nucleus. The method of Green's functions specified in Equations 3.5 and 3.6 is generalizable to arbitrary incident and scattered waves, taking the form of the *Lipmann-Schwinger* equation [121]. In the DWBA, the Coulomb and average nuclear (optical) part U of the potential is separated such that $V = U + iW$, leaving the residual part W to be solved separately and assuming that the effect of U on the bare incident wave $\phi(\mathbf{r})$ doesn't alter the projectile's internal structure. The residual part is that part already solved by previous calculations discussed in this chapter. Comparison to Equation 3.6 shows the solution for the distorted waves $\chi_{\pm}$ is

$$\chi_{\pm}(\mathbf{r}) = \phi_{\pm}(\mathbf{r}) + \int d\mathbf{r}' G_{\pm}(\mathbf{r}, \mathbf{r}')\rho_{\pm}(\mathbf{r}'), \tag{3.33}$$

where now $\phi(\mathbf{r})$ is an arbitrary incident wave and $\rho(\mathbf{r}') = 2\mu/\hbar^2 U(\mathbf{r}')\phi(\mathbf{r}')$. The potential $U(\mathbf{r}')$ has Coulomb and average nuclear parts, the average part being treated in the optical model by Woods-Saxon potentials as

$$U(r') = V_{\mathrm{C}}(r') - V_R(r') - iV_I(r'), \tag{3.34}$$

where the Coulomb term $V_{\mathrm{C}}(r')$ has the same form as in Equation 3.26 and both real and imaginary Woods-Saxon potentials $V_R(r')$ and $V_I(r')$ have the same form as that in Equation 3.27. The optical model parameters for this potential, for both exit and entrance channel, are summarized in Table 3.3. The parameters for the entrance and exit channel of the ^{12}C(t,^{3}He)^{12}B reaction are taken from Ref. [122]. No elastic scattering data specifically on the ^{64}Zn target is available near incident beam energies of 115

Coulomb and Optical Model Parameters

Channel	r_C	V_R	r_R	a_R	V_I	r_I	a_R	χ^2
t+^{12}C	1.25	16.60	1.590	0.705	32.10	0.989	0.868	-
^{3}He+^{12}B	1.25	19.40	1.590	0.705	37.80	0.989	0.868	-
t+^{64}Zn	1.25	29.89	1.320	0.840	37.77	1.021	1.018	-
^{3}He+^{64}Cu	1.25	35.16	1.320	0.840	44.43	1.021	1.018	2.48

Table 3.3: Coulomb and Woods-Saxon optical model parameters, provided to the DWBA code DWHI, for calculating distortion and kinematics in ^{12}C and ^{64}Zn(t,^{3}He) reactions.

MeV/nucleon with tritons or ^{3}He particles. Therefore, as an approximation, the optical potential parameters from ^{3}He - ^{58}Ni elastic scattering data at 147 MeV/nucleon incident ^{3}He energy is used for the exit channel [122]. For the entrance channel, the t - ^{64}Zn parameters are estimated from the ^{3}He - ^{58}Ni values by scaling the real and imaginary Woods-Saxon well-depths by 85% [123].

The DWBA code DWHI is used to solve for the distorted waves, account for kinematics and reaction Q-value, and evaluate the differential cross section. This is done with complete scattering amplitude, finally determined by summing the folded form factors $F(\Delta J_{\rm rel})$ from the previous section and calculating their expectation values in the distorted waves $\chi_\pm$,

$$f(\mathbf{k},\mathbf{k}') = \frac{\mu}{2\pi\hbar^2}\sum_{\Delta J_{\rm rel}}\left\langle \chi_+ \middle| F(\Delta J_{\rm rel}) \middle| \chi_- \right\rangle. \tag{3.35}$$

The differential cross section then is

$$\frac{d\sigma}{d\Omega} = \left(\frac{\mu}{2\pi\hbar^2}\right)^2 \left| \sum_{\Delta J_{\rm rel}}\left\langle \chi_+ \middle| F(\Delta J_{\rm rel}) \middle| \chi_- \right\rangle \right|^2. \tag{3.36}$$

Figure 3.3 (left) shows the completed example calculation for the ground-state to ground-state transition in the ^{12}C(t,^{3}He)^{12}B reaction. The ground state of ^{12}B is a $J^\pi = 1^+$ and a strong Gamow-Teller state. However, there is a smaller excitation of the amplitude leading to $J^\pi = 2^+$, which the tensor-τ interaction will permit interference with. This will be discussed more below in regards to the proportionality breaking. The normalization

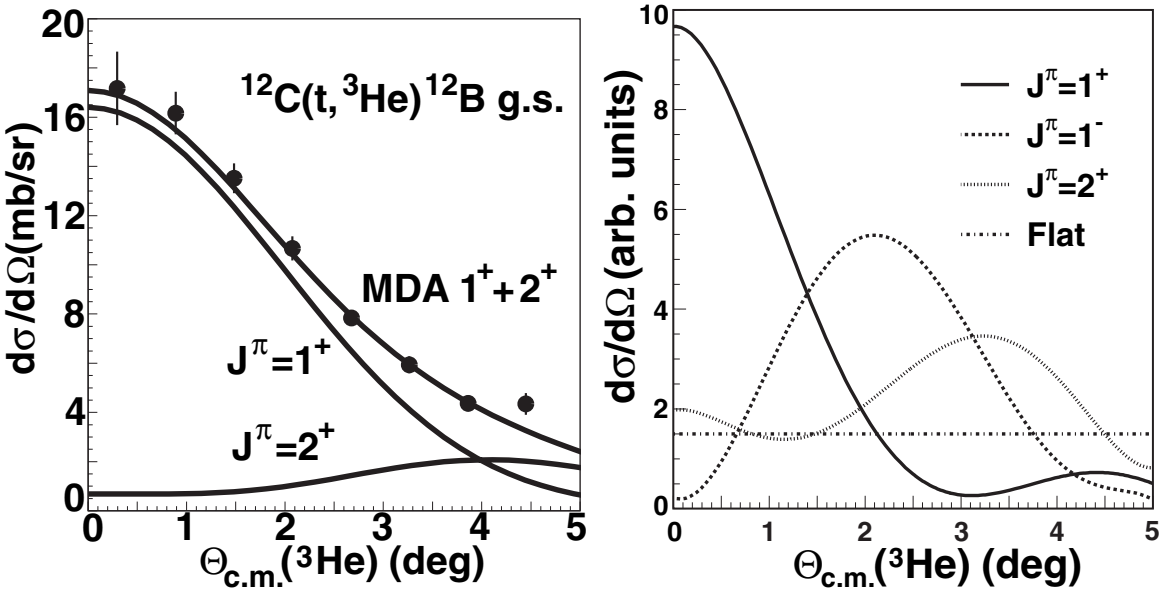

Figure 3.3: (Left) An example of the measured ^{12}B ground state differential cross section, compared to the cross section calculated as specified here. The total cross section is decomposed into the respective contributions from form factors leading to $J^{\pi} = 1^{+}$ and 2^{+} states. (Right) The library of ^{64}Zn(t,^{3}He)^{64}Cu differential cross sections, calculated for use in a multipole decomposition analysis of the ^{64}Cu spectrum.

of both partial cross sections have been scaled to fit the data. Otherwise, the calculation described in this chapter consistently over-predicts absolute cross sections (60%), due to the previously mentioned exchange effects [111]. The shape is all this work is concerned with however, as is explained next concerning the method of multipole decomposition analysis.

3.7 Multipole Decomposition Analysis

The result developed so far has specifically focused on the amplitudes contributing to the cross section of Gamow-Teller excitations. In the experimental measurement however, it is not possible to do so selectively, particularly for the main case of interest, the ^{64}Zn(t,^{3}He) reaction. Therefore, the above procedure to calculate form factors is repeated for this reaction, adding form factors for larger angular momentum transfers. The results are shown in Figure 3.3 (right), where differential cross sections associated with Gamow-Teller ($J^{\pi} = 1^{+}$), dipole ($J^{\pi} = 1^{-}$), and quadrupole ($J^{\pi} = 2^{+}$) transitions are shown.

The flat distribution is included in this set for representing higher angular momentum transfers and transitions to the continuum. Later, in Chapter 6, these distributions will be used to fit measured angular distributions and isolate the Gamow-Teller partial cross section. This is the cross section used in Equation 3.21, divided by the unit cross section in Equation 3.23, that determines the measured B(GT).

3.8 Proportionality Breaking

Since the proportionality used to determine the measured B(GT) is not exact, it is valuable to study sources that break it. As mentioned earlier, in the discussion of empirical evidence of the (^{3}He,t) and (t,^{3}He) unit cross sections, the authors of Refs. [111,112] have done such investigations for ^{58}Ni and ^{26}Mg cases, respectively. The same methods are applied in this work, to determine the source and quantify the size of any proportionality breaking. In both previous works [111, 112], the tensor-τ part V_τ^T of the effective NN-interaction was determined to be the main source of the proportionality breaking. This determination is made possible by the convenient feature of the FOLD code [114] wherein the V_τ^T part of the interaction can be manually set to zero. Formally, this should be done on the level of the interaction used to determine the OBTDs, removing terms that could contribute to $\Delta L = 2, \Delta S = 1$ amplitudes. It is found however, that the former step produces the same result. Therefore, the differential cross sections calculated using the procedure described above can be quickly repeated with and without the tensor interactions included, making for easy comparison. The result of this portion of the study is likewise withheld until Chapter 6 so it can be discussed immediately following the ^{64}Zn(t,^{3}He) data analysis.

Chapter 4

Experiments

Several experiments spread over a period of a few years have contributed to this work in important ways, with the results of each building on past experience and motivating future measurements. Three smaller experiments were done in order to develop the triton beam that is then used to perform the fourth experiment, measuring the differential cross section of states in ^{64}Cu via the ^{64}Zn(t,^{3}He) reaction. This chapter provides an account of all experimental equipment, configurations and measurement techniques used in the four experiments. Additionally, the analysis and conclusions reached for the first three measurements are included here, since these are foundational for the ^{64}Zn(t,^{3}He) measurement. The first measures triton production via fast-fragmentation of ^{18}O ions. The second measures triton production via fast-fragmentation of ^{16}O ions. The third examines techniques to pilot the triton beam in a dispersion-matched mode to the target of the S800 spectrometer for use in (t,^{3}He) reaction spectroscopy. The ^{64}Zn(t,^{3}He) measurement itself is described here, but the detailed analysis and results are treated separately in following chapters.

4.1 Equipment Overview

All measurements are taken at National Superconducting Cyclotron Laboratory, Michigan State University, using the Coupled Cyclotron Facility [47], A1900 Fragment Separa-

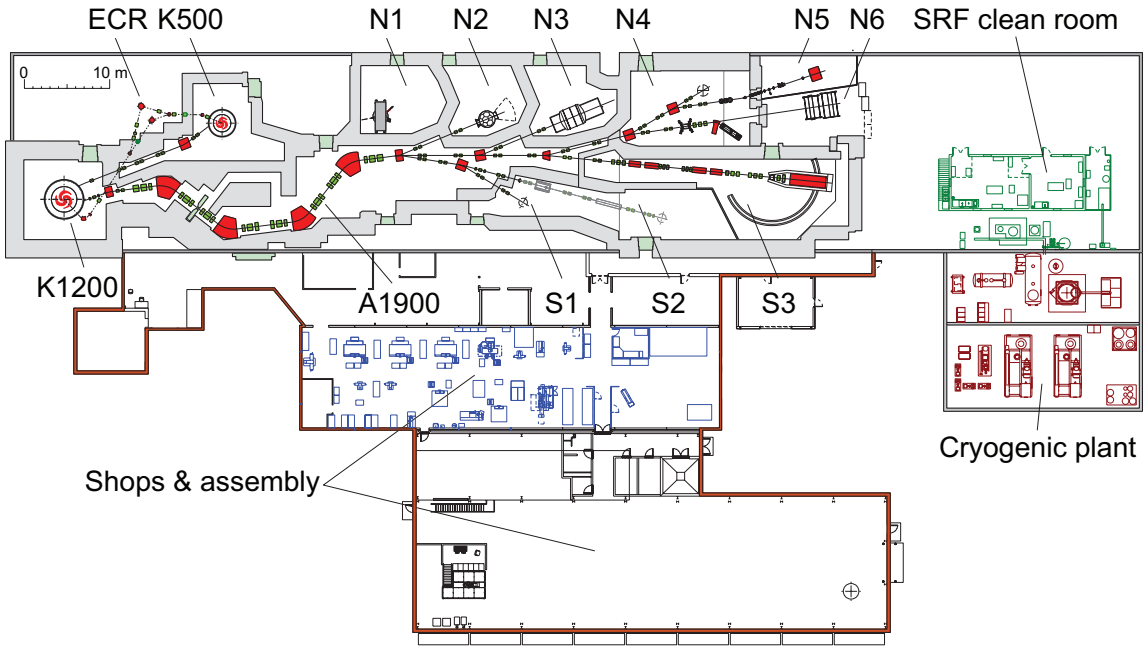

Figure 4.1: Floor plan overview of NSCL experimental facilities as of the beginning of calendar year 2006.

tor [124] and S800 spectrograph [125]. The project to couple the cyclotrons was completed during calendar year 2001. The A1900 Fragment Separator and S800 spectrograph were commissioned soon after. Figure 4.1 provides a overhead layout of NSCL experimental facilities, as of the beginning of calendar year 2006. This schematic is representative of the general configuration of all equipment used, the first of the three triton beam development experiments having taken place mid-2003 and the final measurement of the ^{64}Zn(t,^{3}He) reaction taking place at year's end 2005.

4.1.1 K500⊕K1200 Coupled Cyclotrons

The Coupled Cyclotron Facility (CCF) at NSCL consists to two superconducting cyclotrons, the K500 and K1200 cyclotrons seen upper-left in Figure 4.1, which are coupled to increase the maximum energy of accelerated primary beams. Ions in an intermediate charge state are supplied first from an Electron Cyclotron Resonance (ECR) source and axially injected into the smaller K500 cyclotron. These ions are accelerated to an intermediate velocity by the K500, then extracted along the plane of acceleration into a beamline

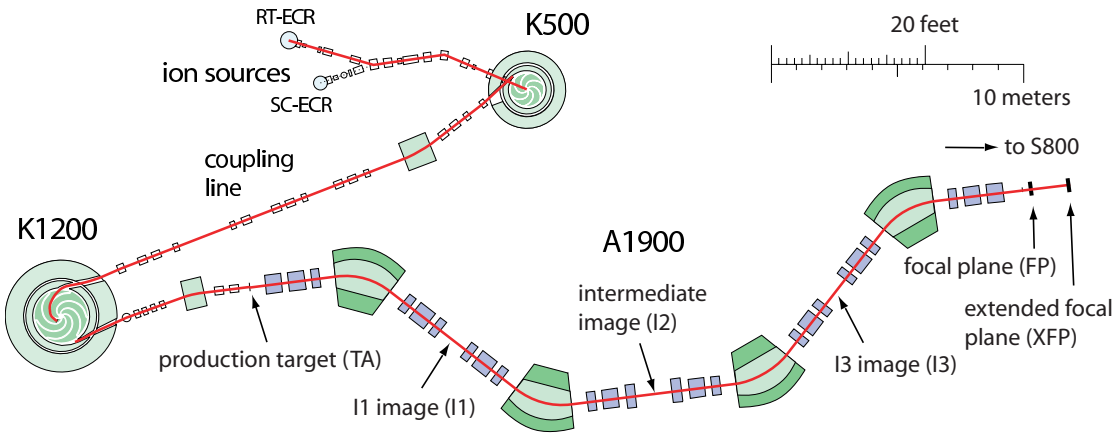

Figure 4.2: Schematic overview of the A1900 Fragment Separator

coupling to the K1200 cyclotron. Ions are then injected into the K1200 cyclotron in the plane of acceleration and stripped to their final charge state. This then makes it possible to use the greater bending power of the larger K1200 cyclotron to accelerate ions to final velocities in excess of half the speed of light. Ions forming the primary beam are finally extracted from the K1200 accelerating plane into a beamline for transport to a fragmentation target station, for production and separation of secondary beams in the A1900 Fragment Separator, seen upper-center in Figure 4.1.

4.1.2 A1900 Fragment Separator

The A1900 Fragment Separator is a two-stage projectile fragmentation spectrometer, designed to produce radioactive secondary beams by magnetic separation of collision products from a fast primary beam. The A1900 is composed of four 45° dipole bending magnets and 40 higher-order multipole magnets for physical correction of optical aberrations. See the upper-center region of Figure 4.2 for reference. The maximum magnetic rigidity ($B\rho$) of the A1900 is 6 T·m and it's large-bore (10 cm and larger) quadrupole magnets and large vertical gap (9 cm) dipoles allow an $d\Omega = 8$ msr solid-angle acceptance, though differing depending on the specific reaction. The maximum momentum acceptance is $dp/p = 5.5\%$, allowing for up to 90% of projectile fragments produced, depending on specific fragment, to be transmitted to the A1900 focal plane for identi-

fication and or transmission to experimental end-stations. The intermediate dispersive image (A1900 I2) at the center of the A1900 features remote retractable collimators and can be instrumented with position and timing-sensitive detectors for event-by-event particle tracking. The A1900 focal plane (A1900 FP) is located following the last multipole magnet of the Separator and is positioned as an experimental end-station for A1900-only measurements. A vacuum chamber located at the focal plane is equipped with remote retractable drives which can be instrumented with position and timing-sensitive detectors and detectors for measuring particle energy-losses and total kinetic energies. Following the focal plane station, the A1900 is also equipped with an Extended focal plane (A1900 XFP) detector suite, a limited version of the focal plane station, but optimally located to identify particles delivered to other experimental end-stations.

Reference List of A1900 Detectors with Main Features

Below is a list of only those A1900 detectors used during some or all of the four experiments. It is provided as a reference when reading following sections about the measurements and analysis. It is not meant to provide an exhaustive list of all detectors available in the Fragment Separator.

1. Faraday Cups (FC)

    - circular copper mesh, 25 mm diameter
    - located on remote retractable drives at fragmentation target
    - output signal is the current induced by unreacted primary beam
    - sensitive from 10 epA to 100 eμA, under 5 W power deposition
    - intercepting method to monitor primary beam intensity

2. Faraday Bars (FB)

    - machined copper bar

- located on the inside walls of the A1900's first dipole
- output signal is the current induced by unreacted primary beam
- sensitive from 1 enA to 100 eμA, under 4 kW power deposition
- non-intercepting method to monitor primary beam intensity

3. Viewers
   - 1/8"-thick ^{nat}Al plate stock coated with ZnO phosphor
   - located on remote retractable drives at image planes
   - output signal is visible light emission, monitored by camera
   - sensitivity qualitative, depends on camera type and gain, ion rate and charge, $\sim$1-2 mm position resolution
   - characterize beam spot size, real-time tuning diagnostic
4. Thin Plastic Scintillators (tSCI)
   - 25.8 or 198.5 mg/cm^2 thick Bicron^{TM} BC-400 plastic ($^{12}C_9H_{10}$)
   - located on remote retractable drives at I2, FP, and XFP
   - output signal is timing and voltage pulse from two gain-matched photo-multiplier tubes
   - timing relative to acquisition start, voltage amplitude proportional to energy deposition, position inferred from phototubes' relative signals with 30 mm resolution
   - measure timing, rate, position for momentum correction
5. Thick Plastic Scintillator (SCI)
   - 19.8 g/cm^2 thick Bicron^{TM} BC-400 plastic ($^{12}C_9H_{10}$)
   - located on remote retractable drive at FP

- output signal is timing and voltage pulse from two gain-matched photo-multiplier tubes
- timing relative to acquisition start, voltage amplitude proportional to energy deposition
- measure timing and particle total energy

6. Silicon PIN Detectors (PIN)
   - 116.1 g/cm^2 thick, doped-silicon *npn*-type wafer diode
   - located on remote retractable drive at FP and XFP
   - output signal is timing and voltage pulse from collision-induced promotion of conduction electrons across band-gap
   - timing relative to acquisition start, voltage amplitude proportional to energy deposition
   - measure timing and particle energy loss
7. Parallel Plate Avalanche Counters (PPAC)
   - 100 mm $\times$ 100 mm or 400 mm $\times$ 100 mm, HV gas-filled capacitor with segmented anodes
   - located in pairs on remote retractable drives at I2, FP
   - output signal is anode current created by secondary electron showers in the fill gas
   - single-event sensitivity below 30 kHz count rate
   - measure event-by-event x/y positions

4.1.3 S800 Spectrograph

The S800 spectrograph is located in the S3 end-station at NSCL, seen at a side-view in Figure 4.3. The setup has two important parts; the Analysis Line and the spectrograph

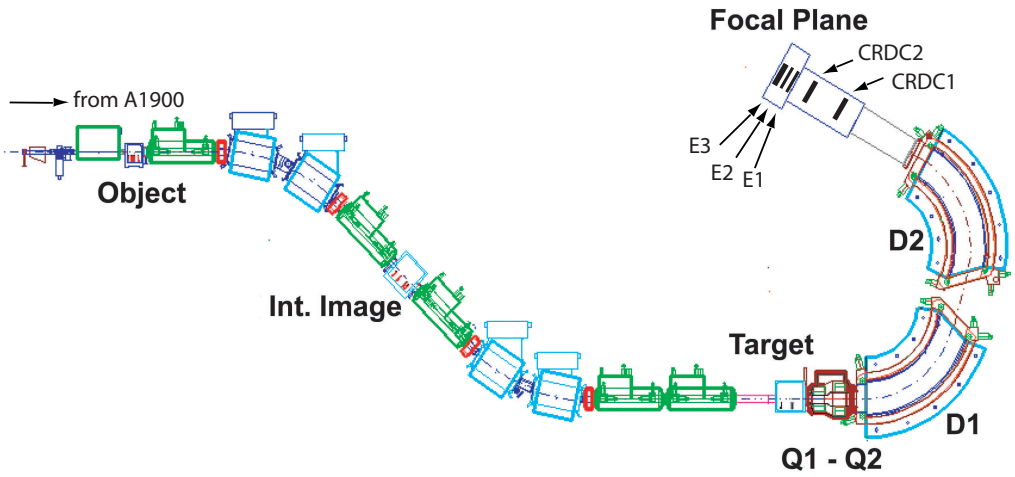

Figure 4.3: Schematic overview of the S800 spectrograph

itself. The Analysis Line is a two-stage, vertical spectrometer preceding the spectrograph. It is designed specifically to tune large-emmitance secondary beams in a focused or dispersion-matched mode and has a maximum magnetic rigidity of 4.8 T·m. The spectrograph is a vertical recoil spectrometer mounted on a platform allowing it to be rotated up to 60° off the beam axis. It is composed of a large-bore doublet of two focusing quadrupole magnets following the target position and two large-gap dipole magnets which make up the sector field. The angular acceptance is $d\Omega = 20$ msr and the momentum acceptance is $dp/p = 5\%$. The object position has highly variable geometry to accommodate coincidence detection systems. Small target stations and external detector systems can be deployed or the Large Scattering Chamber, a 6"×6"×6" vacuum chamber with mounts for retractable drives and benches for large, in-vacuum detectors. The S800 focal plane (S800 FP) is instrumented with position and timing-sensitive detectors and detectors for measuring particle energy-losses and total energy. The spectrograph energy resolution can be up to 1 part in 10,000 depending on optical settings. This is achieved in the absence of higher-order multipole magnets by ray-tracing particle trajectories through the spectrograph using magnetic field maps and calibration measurements made with a series of sieve-slit plates in the focal plane.

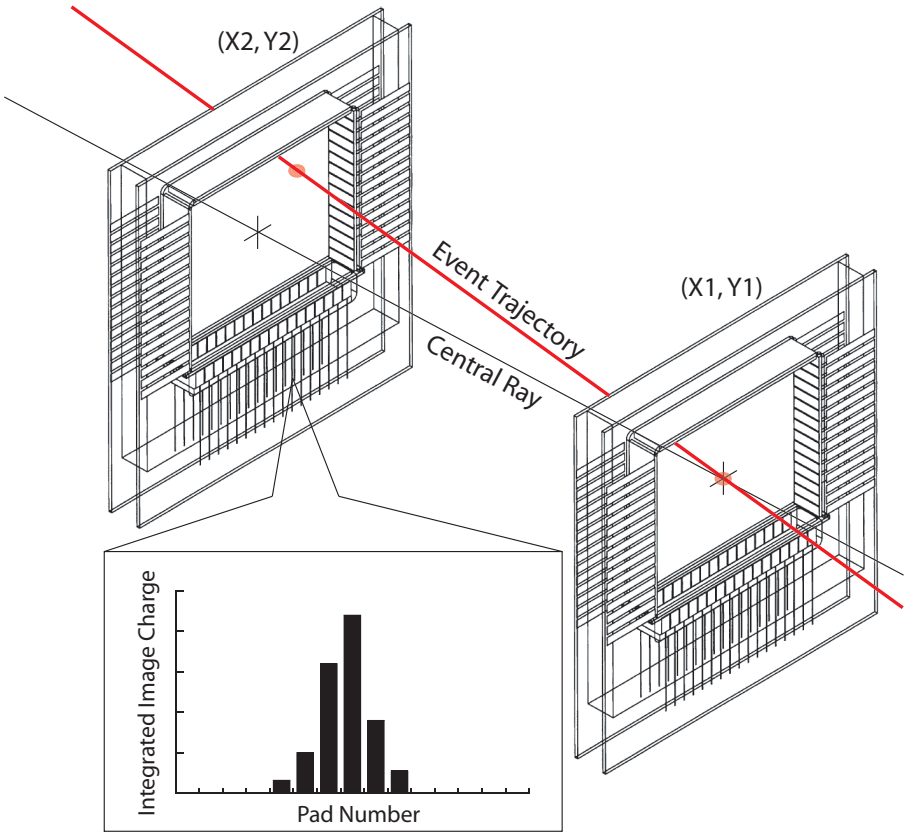

Figure 4.4: Schematic view of the S800 focal plane CRDCs, adapted from figures in Ref. [126]. The central ray of the S800 is represented by the black line and an example event by the red curve. The insert at lower-left shows an example of the integrated image charge on the segmented cathode pads for an event.

Reference List of S800 Detectors with Main Features

Below is a list of only those S800 detectors used during some or all of the four experiments, provided as a reference when reading following sections about the measurements and analysis.

1. In-Beam Scintillators (IBM)

   - 103.2 mg/cm^2 thick Bicron™ BC-400 plastic ($^{12}C_9H_{10}$)
   - on remote retractable drives at Analysis Line Object and S800 Target
   - output signal is timing and voltage pulse from one photo-multiplier tube

- measure rate

2. Cathode Readout Drift Chambers (CRDC)

   - gas-filled, HV single-wire drift detector with segmented cathode readout, 30 cm $\times$ 59 cm active area
   - two CRDCs separated by 1073 mm located in S800 focal plane
   - output signals are drift time of secondary electrons to the anode wire and current-integrated total charge on cathode pads induced by the anode current
   - drift time to anode relative to acquisition start gives y-position, center-of-charge on cathode pads calculated in software gives x-position
   - measure event-by-event x/y positions

3. Focal Plane Scintillators (E1, E2, and E3)

   - 30 cm $\times$ 59 cm Bicron™ BC-400 plastic ($^{12}C_9H_{10}$), 5 cm (E1), 10 cm (E2), and 20 cm (E3) thick
   - located in S800 focal plane
   - output signals are timing and voltage from two phototubes on each detector, voltage amplitude proportional to energy deposition
   - measure timing, particle energy loss (E1,E2) and total energy (E3)

Figure 4.4 shows a schematic view of the CRDC detectors, adapted from figures in Ref. [126]. Each CRDC provides a 2-dimensional measurement of the event trajectory in the plane perpendicular to the direction of propagation. In the non-dispersive (Y) direction, this is done by applying an anode voltage and measuring the time difference between the DAQ trigger and the arrival of secondary electrons drifting in through the fill gas to be collected on the anode wire. The dispersive direction is measured indirectly by measuring the image charges formed on the segmented cathode lead. In the lower-left hand insert in Figure 4.4 provides a basic example. Image charge is integrated from

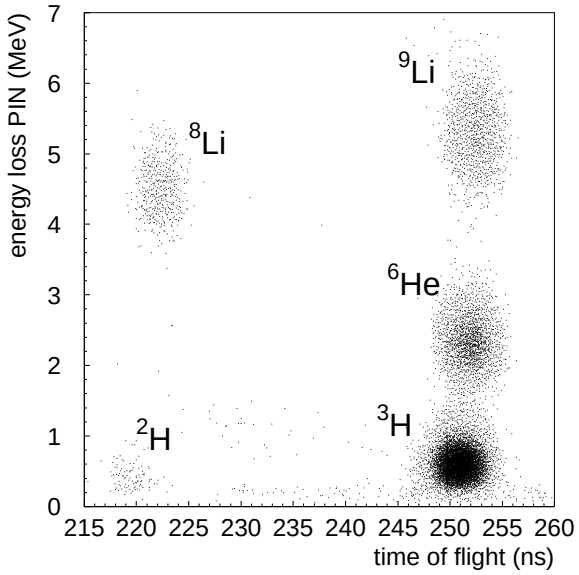

Figure 4.5: Typical particle identification spectrum measured in the focal plane of the A1900 during the triton production experiments: the energy loss in the PIN detector is plotted versus TOF. The different species can be clearly separated.

each cathode pad for a set time interval following the DAQ trigger. The distribution of integrated image charge over the cathode pads contains information about the location of the event, as seen in the insert. This dispersive location is determined by fitting the distribution with a Gaussian function and taking the peak location as the position. The advantage of this technique includes the possibility of determining the dispersive location to an accuracy that is finer than the pad segmentation size [126]. From the pair of position measurements in the CRDC planes, the associated dispersive and non-dispersive angle of each event trajectory is calculated.

4.2 Development of a Secondary Triton Beam

Motivation

The (t,^{3}He) reaction was recently studied on ^{12}C, ^{26}Mg and ^{58}Ni targets [111, 112] and was established as a valuable addition to (n,p) [28, 34] and (d,^{2}He) [42, 127] reactions for extracting Gamow-Teller strength distributions. These (t,^{3}He) experiments were per-

formed at the NSCL using a secondary 115-MeV/nucleon triton beam however, it was produced from a 140-MeV/nucleon primary ^{4}He-beam [5,6,128,129] from the lone K1200 Cyclotron, prior to the CCF upgrade. Using the A1200 Fragment Separator and S800 spectrograph, energy resolutions for the (t,^{3}He) reaction varied from 200 keV to 300 keV (FWHM) and triton-beam intensities achieved were $\lesssim 1 \times 10^6$ pps. Coupling the K500 Cyclotron to the K1200 as a pre-accelerator required changes to the injection and stripping scheme of the K1200 such that ^{4}He is not available as primary beam from the K500⊕K1200 system [47]. Therefore, to continue investigations with the (t,^{3}He) probe at NSCL, it became necessary to find an alternative method to produce a secondary triton beam and desirable to improve the efficiency of (t,^{3}He) experiments by developing higher intensity beams.

An alternative way to produce a secondary triton beam and to improve the triton-beam intensity is investigated using fragmentation of primary beams of ^{16}O (150 MeV/nucleon) and ^{18}O (120 MeV/nucleon). These are the lightest available beams that can be accelerated with the CCF [47]. Since ^{18}O is more neutron-rich than ^{16}O, a higher triton yield was expected, but since the goal is to reach triton energies in excess of 100 MeV/nucleon, the higher ^{16}O beam energy could be advantageous. Fragmentation methods for producing secondary beams of unstable particles have been widely employed [130], but parameterizations used to predict yields of light fragments from heavy-ion beams [131] in simulation codes of fragment separators such as LISE [132] are not necessarily reliable, since many intermediate channels can contribute. In fact, such calculations performed for the current work based on the EPAX2.15 parameterization [131], underestimated the measured rates by a factor of about 30.

The energy of the secondary triton beam is also constrained, being limited by the capability to transport the tritons from the production point to the the S800 spectrograph [125]. Depending on the ion-optical tune, the $B\rho$ value achievable in the S800 Analysis Line ranges from 4.8 to 5.0 T·m, corresponding to triton energies of 115 to 125 MeV/nucleon. In order to obtain high-resolution (t,^{3}He) data, the Analysis Line and spectrograph must be operated in dispersion-matching mode. This limits the opti-

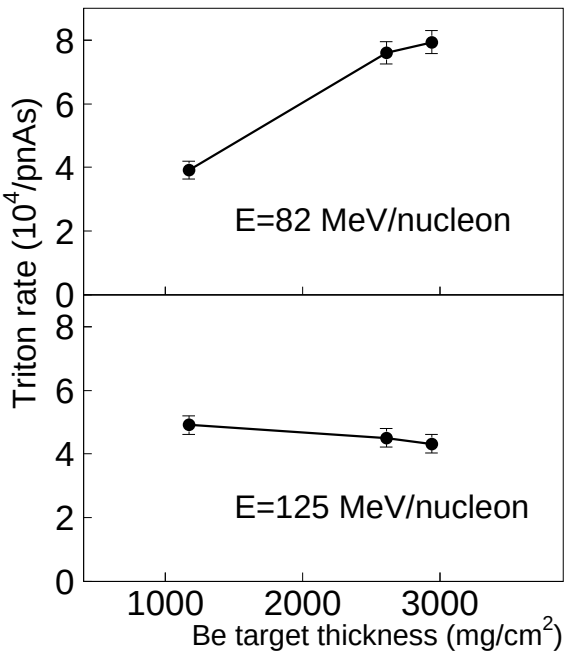

Figure 4.6: Triton production rate using an ^{18}O primary beam as a function of production target thickness for triton energies of 82 MeV/nucleon (top) and 125 MeV/nucleon (bottom). The lines are to guide the eye. Error bars are mostly systematic and dominated by uncertainties in the primary beam intensity.

cal properties (phase-space correlations) and momentum spread of the triton beam to $dp/p_0 = 5 \times 10^{-3}$ [125], where p_0 is the central beam momentum and dp the full momentum spread. After optimization based on all the above considerations, the ^{24}Mg(t,^{3}He) reaction was used as a test case to determine the excitation-energy resolution achievable.

4.2.1 Triton Production via Fragmentation of ^{18}O

A 120 MeV/nucleon $^{18}O^{8+}$ beam produced in the NSCL CCF bombarded a Be production target placed at the entrance of the A1900 fragment separator [124]. Three production targets with thicknesses of 1170 mg/cm^2, 2609 mg/cm^2 and 2938 mg/cm^2 were used. Triton yields at magnetic rigidities of 4 T·m and 5 T·m (corresponding to triton energies of 82 MeV/nucleon and 125 MeV/nucleon, respectively) were measured, so that a rough dependence of yield on triton energy could be investigated. The momentum acceptance was limited to $dp/p_0 = 5 \times 10^{-3}$ by placing a slit at the intermediate image of the A1900.

The secondary particles were detected in the A1900 focal plane and identified by mea-

suring the time-of-flight (TOF), relative to the radio-frequency signal (RF) of the K1200 cyclotron, and the energy losses in a detector stack consisting of a 100-mm thick plastic scintillator and a 0.5-mm thick silicon PIN detector. Tritons were cleanly separated from other particles produced in the production target, as shown in Fig 4.5. The relative contribution from contaminants increased at lower magnetic rigidities. For $E_t \geq 110$ MeV/nucleon, it was found that tritons dominate the production yield ($\geq 85\%$). Although further suppression of background was possible by inserting a wedge in the intermediate image of the A1900 and making use of the difference in energy loss for the various secondary products, it also slightly reduced the triton rate.

Results

In Figure 4.6, the results for the triton production rates with the ^{18}O beam are presented. A maximum intensity of 7.9×10^4/pnAs (i.e. per particle nano-Ampère of the primary beam, per second) was achieved using the 2938-mg/cm^2 thick $^{\text{nat}}$Be production target and selecting tritons with an energy of 82 MeV/nucleon. The highest rate achieved at the triton energy of 125 MeV/nucleon is 5.0×10^4/pnAs. The reduction in triton rate at the higher triton energy is due to the fact that the energy per nucleon of the triton beam is slightly larger than that of the ^{18}O primary beam, and the high-energy tail of the energy distribution has been selected.

4.2.2 Triton Production via Fragmentation of ^{16}O

Triton-production rates using a 150 MeV/nucleon primary ^{16}O beam were measured in a similar manner, but with smaller steps in magnetic rigidity (i.e. triton energy). At this beam energy, a greater optimum thickness of $\sim$4000 mg/cm^2 for the production target was predicted by calculations with EPAX2.15 [131] in code LISE [132]. Therefore, rates were measured using a wider variety of Be-target thicknesses than in the ^{18}O measurement, ranging from 1480 to 5524 mg/cm^2. Target thicknesses in steps of approximately

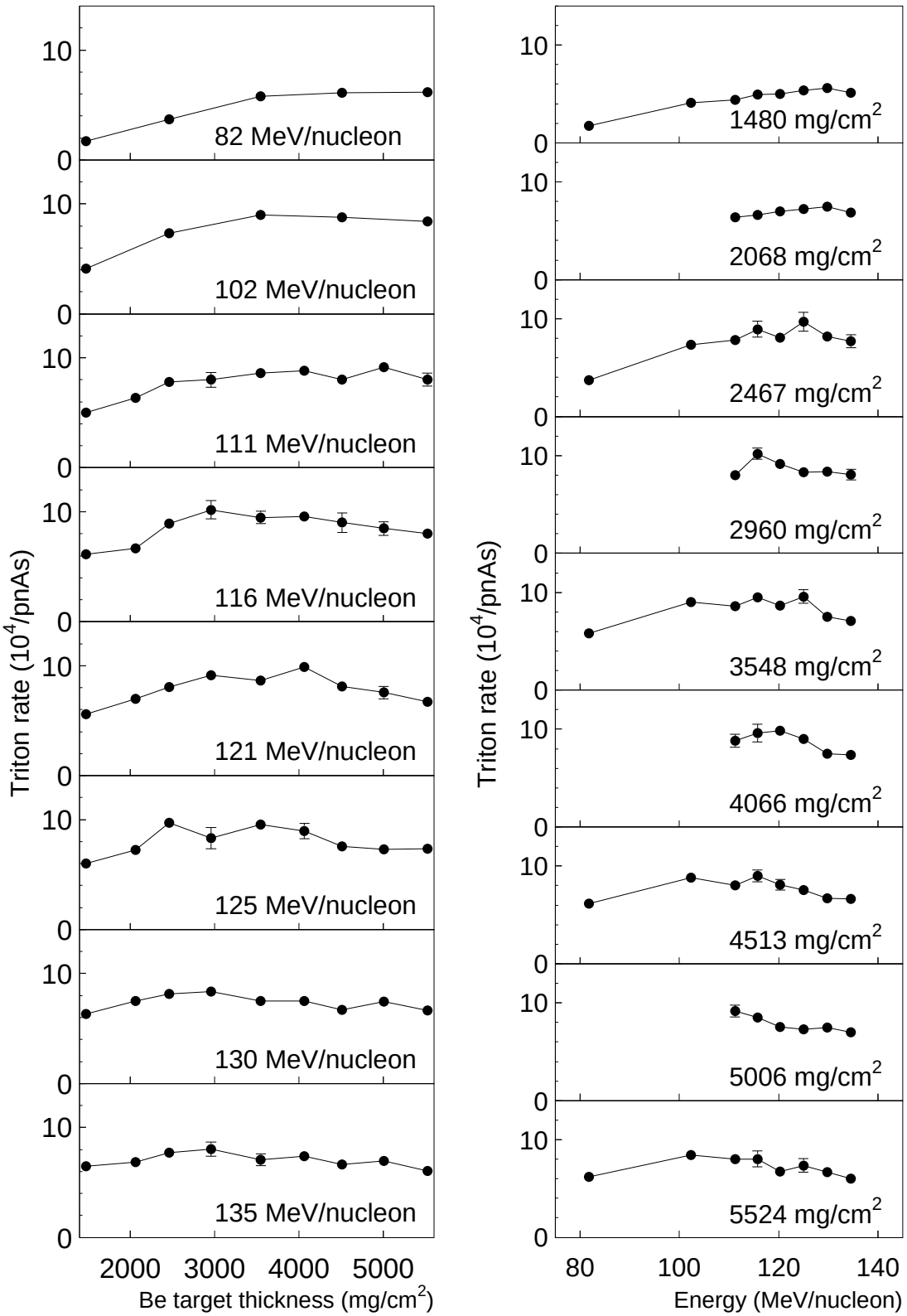

Figure 4.7: Triton production rate from fragmentation of a ^{16}O primary beam; (Left) versus primary target thickness, with triton energies indicated in each panel, and (Right) versus triton energy, with the thickness of each of ^{nat}Be production target used indicated in each panel.

500 mg/cm^2 could conveniently be achieved by using combinations of targets placed in the two ladders of the A1900 target box.

In Figure 4.7 (left) the triton production rate as a function of target thickness is shown for different triton energies. In Figure 4.7 (right), the rates are plotted as a function of triton energy for the different target thicknesses used. Systematic errors were due to uncertainties in primary beam intensities. These were estimated on a run-by-run basis from a measurement of the current in a Faraday cup inserted in front of the target before and after each run. Another component to the error is due to the slight difference in transmission through the A1900 for tritons generated in the primary production targets located in different ladders. See below for more details.

Analysis of Systematic Error in Triton Production Rates

During preparation for the full test experiment for the (t,^{3}He) probe, the triton rates shown in Figure 4.7 were investigated to determine if observed structure in the production rates could be attributed to systematic errors. To accomplish this, the properties of the triton beam were studied by simulating the acceptance and transmission of the A1900 Fragment Separator with the ion-optics code MOCADI [133]. The MOCADI input consists of transfer matrix representations of each of the 40 multipole magnets, calculated to third-order in optical aberrations, and measured values for the inter-magnet drift distances and bore-diameters.

Recall that for the ^{16}O fragmentation experiment, two separate target ladders were used, with an array of production targets on each, that allowed for total thicknesses between 1480 mg/cm^2 and 5524 mg/cm^2 in 500 mg/cm^2 increments. The two ladders holding the production targets are separated by 12.6 cm which means the phase-space volume of the triton beam has two components, each with different optical properties. The magnetic field of the first A1900 triplet, which determines the A1900 object location, is manually tuned to maximize the total transmission of tritons. In Figure 4.8, the dispersive angle (momentum) of tritons is plotted versus their corresponding dispersive position

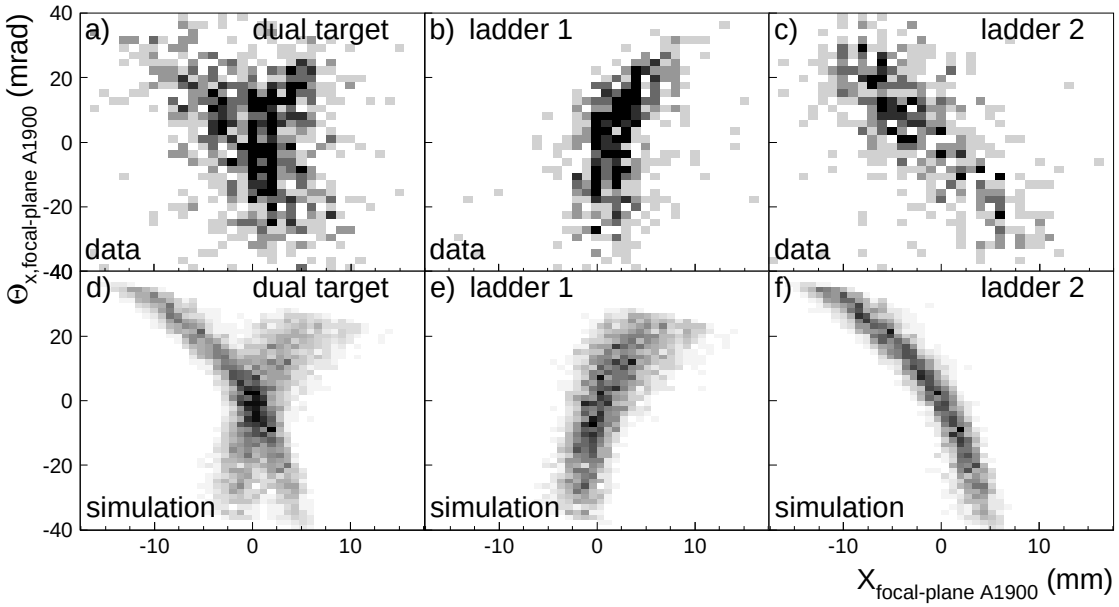

Figure 4.8: Phase-space selection plots of triton beams, with dispersive angle plotted versus dispersive positions (i.e. momentum vs. position) for (a, b, c) measurements using different target configurations in the ^{16}O fragmentation experiment, and (d, e, f) simulation with the ion-optical code MOCADI for the same settings.

using data taken with a pair of PPACs at the A1900 focal plane. The two-component nature of the beam's phase-space is seen in Figure 4.8 a) and d), for data and simulation with dual targets respectively. The two contributions are isolated by individual measurement in Figure 4.8 b) and d) and decomposed in simulation in Figure 4.8 e) and f). In general, a source of rays located at the object of a thin-lens-like system leads to a phase-space profile for rays at the focal point that is vertical (focus condition). By matching the observed correlations with simulation, it is determined that the manual triplet tune that maximizes the triton intensity at the A1900 focal plane places the A1900 object location between the two target ladders: 2.0 cm downstream of ladder 1 or 10.6 cm upstream of ladder 2.

Results

The mixed phase-space created by producing the tritons with two separate targets may pose only minor difficulty operating the S800 spectrograph in focus-mode optics. How-

ever, this state spoils the conditions necessary to operate the beamlines in a dispersion-matching mode which is necessary for high resolution with the (t,^{3}He) reaction. A good dispersion-matched beam would be characterized by a strong correlation between dispersive position and angle at the S800 target. If a dual target scheme is used, it would only be possible to produce such a correlation for one of the beam's phase-space components. That would leave the other component as a sizeable portion of the beam that is poorly dispersion-matched. At $dp/p_0 = 5 \times 10^{-3}$ momentum acceptance, the spread in triton energies at the S800 target is ∼3.5 MeV, which for the poorly matched component would also be the resolution. Therefore, it is important to locate all of the production target material on a single ladder at the A1900 object.

In summary, maximum rates ($8 - 10 \times 10^4$/pnAs) were achieved for triton energies between 116-125 MeV/nucleon (∼80% of the energy per nucleon of the primary beam) using Be target thicknesses between $3 - 4 \times 10^3$ mg/cm^2. At the lowest triton energies, the highest rates are achieved with the thickest Be targets. The optimum target thickness slowly becomes smaller with increasing triton energy. Acceptance effects stemming from the dual target configuration are estimated to be about 5% and are responsible for the deviations seen from smooth trends in Figure 4.7 (left).

In comparison to the experiment using ^{18}O at 120 MeV/nucleon as the primary beam, the maximum triton production rate is very similar, but is achieved at a much higher triton energy. For the production of tritons of an energy of 125 MeV/nucleon, the maximum rate achieved with the primary ^{16}O beam at 150 MeV/nucleon is about twice that obtained with the primary ^{18}O beam at 120 MeV/nucleon. For the production of tritons of 82 MeV/nucleon, the results are more or less reversed.

4.2.3 First Experiment with the Secondary Triton Beam

The secondary triton beam produced from a primary ^{16}O beam was subsequently used to study the (t,^{3}He) reaction, focusing on the transport of the beam from the A1900 to the target located at the entrance of the S800 spectrometer [125] and the excitation energy

resolution obtained in the reaction. A 9.86-mg/cm^2 thick, 99.92% isotopically-enriched ^{24}Mg target was used.

Since the triton beam produced at the A1900 fills a relatively large phase space, the transmission to the S800 target location was limited by the inner dimensions of the beam-line magnets and transmission lines. To study the transmission of the secondary triton beam, two retractable 1-mm thick in-beam scintillators (IBSs) were installed, one at the object of the S800 analysis line, the other at the target position of the S800. This transmission study was performed at relatively low triton-beam intensity ($\sim 10^5$ pps) to ensure that efficiencies for detection of the tritons in the IBSs exceeded 95%. The optimal transmissions from the A1900 focal plane to the object in the analysis line and from the object to the S800 target position were $\sim$ 60% and $\sim$ 85%, respectively, resulting in a total transmission of $\sim$ 51%. This transmission was achieved at a triton-beam energy of 115 MeV/nucleon ($B\rho = 4.8$ Tm). At higher energies the current in some of the beam-line magnets could not be increased sufficiently to obtain optimal conditions for dispersion matching and led to a lower transmission. Final experiments were performed using a 3526-mg/cm^2 thick production target to produce a 115 MeV/nucleon triton beam with an intensity of 4.8×10^4/pnAs at the S800 target (including transmission efficiency). The primary ^{16}O beam intensity available was 100 pnA or higher, resulting in triton beam intensities of $\gtrsim 5 \times 10^6$ pps.

The ^{3}He particles produced in the ^{24}Mg(t,^{3}He) reaction were detected in the focal-plane detector system of the S800 [126]. It consisted of two scintillators preceeded by two two-dimensional cathode-readout drift chambers (CRDCs), used to determine the positions and angles in the dispersive and non-dispersive directions. The first scintillator served as the event trigger and the start of the TOF measurement. The TOF stop signal was given by the cyclotron RF. ^{3}He particles were identified by combining the TOF measurement and the $\Delta E - E$ response in the two scintillators. The ion-optical code COSY Infinity [134] was used to calculate the ion-optical transfer matrix of the S800 spectrometer [135] from the measured magnetic field maps. Matrix elements up to fifth order were used in the reconstruction of $\delta = (E - E_0)/E_0$; E_0 is the kinetic energy of the particle

following the central-ray trajectory through the spectrometer and E the energy of the measured particle. The track angles were also obtained in the ray-tracing procedure and used to calculate the ^{3}He scattering angle ($\Theta_{^3\mathrm{He}}$). From these reconstructed parameters, the excitation energy in ^{24}Na was obtained from a missing-mass calculation.

Results

In Figure 4.9a,b the reconstructed ^{24}Na excitation-energy spectra are shown for $0^\circ < \Theta_{^3\mathrm{He}} < 4^\circ$ and $0^\circ < \Theta_{^3\mathrm{He}} < 1^\circ$, respectively. The Gamow-Teller transition to the 1^+ state at $E_x(^{24}\mathrm{Na})$=1.35 MeV was used to determine the energy resolution. Minor contributions from transitions to $J^\pi = 2^+$ and $3^{(+)}$ states, both located at 1.34 MeV [136], do not affect the width of the peak significantly.

The excitation-energy resolution at forward scattering angles was determined to be 190$\pm$15 keV (FWHM) (Figure 4.9b). Due to the kinematic correlation between ^{3}He angle and energy associated with the recoil of the ^{24}Na residual, and the finite resolution of the ^{3}He angle measurement, the resolution slightly worsens with increasing scattering angle. When integrating over ^{3}He scattering angles between 0° and 4° the energy resolution was 220 ± 10 keV (Figure 4.9a). The angular resolution was 0.5° (FWHM), measured using the H(t,^{3}He)n reaction (with a CH_2 target) for which the kinematic correlation between ^{3}He angle and energy is strong.

Part of the energy spread is due to the difference in energy loss of the triton and ^{3}He in the target (50 and 210 keV loss over the full thickness of the ^{24}Mg target, respectively). The energy straggling in the target contributes $\sim 25-50$ keV, depending on the location where the (t,^{3}He) reaction takes place in target . Using a simple folding procedure, it was determined that the intrinsic energy resolution (i.e. not related to energy-loss and straggling effects) was 170 ± 15 keV. Under 'optimal' circumstances (object size of 0.5 mm), the energy resolution of the S800 is 1 part in 10000 [125], corresponding to $\sim$ 35 keV for (t,^{3}He) experiments at 115 MeV/nucleon. From the ratio of optimal and deduced experimental resolutions and the known energy dispersion of the S800 spectrometer [5

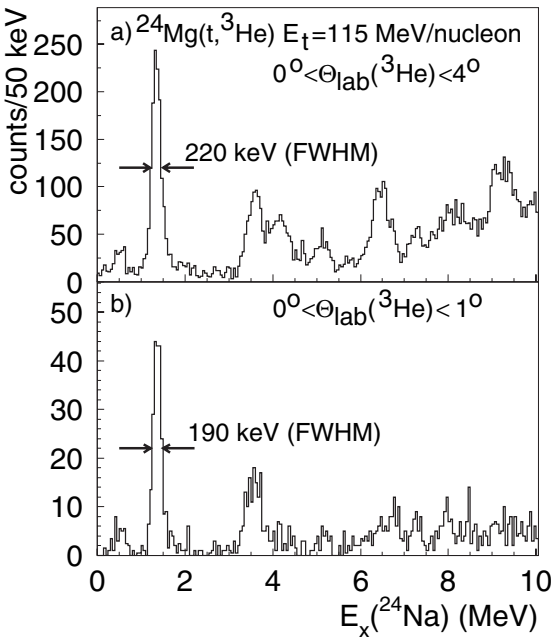

Figure 4.9: ^{24}Mg(t,^{3}He) excitation-energy spectra for ^{3}He angular ranges of a) 0°-4° and b) 0°-1° using a secondary triton beam of 115 MeV/nucleon produced with a primary ^{16}O beam of 150 MeV/nucleon.

cm/%($\frac{\delta E}{E_0}$)], it is concluded that the incoherent object size of the secondary triton beam was about 2.5 mm during the experiment. This size is consistent with the size of the beam spot observed using a viewer at the object.

There were several difficulties which should be mentioned, which made this measurments challenging. First, the neutron radiation levels due to primary beam losses in the cyclotrons damaged computer control hardware inside the K1200 shielding vault. This created several interuptions during the experiment and sensitive equipment has since been moved outside to improve operations. Related to this, the heat desposition due to these losses ultimately ended the experiment, melting a segment of the K1200 main deflector and obtructing the beam extraction. Currently, intensity gains for the triton beam are loss-limited by the extraction efficiency of the ^{16}O primary beam from the K1200 cyclotron. Also, one of the two CRDC detectors had some construction defects and had a sizable dead-region. This limited the range of excitation energies that could be observed in ^{24}Na.

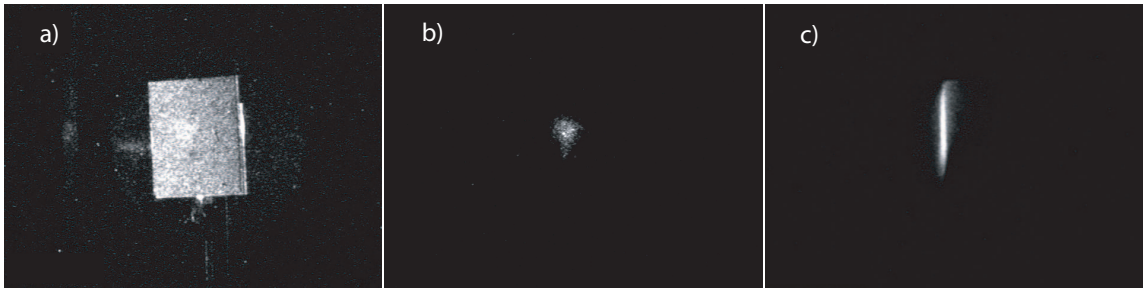

Figure 4.10: Screen shots of a ^{16}O pilot beam a) with and b) without lighting at the target position and c) of the triton beam, momentum-dispersed over the Zn target.

4.3 Measurment of the ^{64}Zn(t,^{3}He)^{64}Cu Reaction

Many of the settings for the CCF, A1900 and S800 devices used in the ^{24}Mg test experiment are used for the ^{64}Zn case. The triton beam was produced from the 150 MeV/nucleon $^{16}O^{8+}$ primary beam on a single, thick (3500 mg/cm^3) ^{nat}Be production target, in accordance with previous findings for the optimal production settings [7]. The A1900 Fragment Separator [124] is set to magnetic rigidity $B\rho = 4.8$ T·m and momentum acceptance $dp/p = 0.42\%$ to select 115 MeV/nucleon tritons with an 0.84% (∼3.5 MeV) energy spread. The isotopic purity of the triton beam was 85% and the average intensity at the reaction target was $\approx 3\times10^6 s^{-1}$. The Analysis Line of the S800 spectrograph was operated in the dispersion-matching mode [137] to maximize the resolution. The S800 acceptance transfered events within ±40 mrad for both dispersive and non-dispersive event angles, as reconstructed at the target. Figure 4.10 a) and b) shows camera screen-captures of the unreacted ^{16}O pilot beam spot in focus mode and attenuated to a factor $\times10^6$ below maximum. The ^{16}O pilot beam is used first to provide a rough check of the beamline optics, since its higher charge makes its image on the viewer easier to see. Panels a) and b) respectively are pictures taken with and without lighting in the target chamber to show the viewer profile. Figure 4.10 c) shows the triton beam spot in the dispersion-matched mode, attenuated 33% below maximum intensity. The beam spot height is ∼5 cm, which is consistent with dispersion in the triton beam and the energy resolution achieved in the S800 focal plane, due to the dispersion-matched tune of the

Analysis Line.

The target used is self-supported a 9.84 mg/cm^2, 99.6% pure ^{64}Zn foil. Unreacted tritons cannot be bent into the S800 acceptance so as to directly normalize measured cross sections by counting particles of unreacted beam. Therefore, the triton intensity was indirectly monitored by calibrating an IBS placed at the S800 target position with the Faraday Bar current in the D1 dipole of the A1900. The ^{12}C(t,^{3}He) reaction was also measured, using a $^{12}CD_2$ plastic target, for a known reference cross section. The strong GT transition of known cross section, from the ^{12}C 0^+ ground state to the ^{12}B 1^+ ground state, provides a consistency check on the indirect normalization for the measured ^{64}Cu spectrum.

Reaction products are momentum analyzed by the S800 and their full momentum is determined in the S800 focal plane [126] using two CRDCs as tracking detectors and two plastic scintillators ($E1$ and $E2$) to measure energy losses and event time-of-flight (TOF). The $E1$ signal is the data acquisition and TOF start. The CCF RF signal is the TOF stop. Ion energy loss in $E1$ and event TOF allow for unambiguous identification of ^{3}He events in the S800 focal plane. The full data analysis and results are the subject of following chapters.

Conclusion

In conclusion, a high-quality secondary triton beam has been produced from fragmentation of a 150 MeV/nucleon ^{16}O primary beam. The dispersion-matching tune and transmission of the triton beam was studied and the ^{24}Mg(t,^{3}He) reaction was measured as a successful test case. For easy comparison with results from the test experiment, some basic findings from the ^{64}Zn analysis are included here. The excitation energy resolution obtained in the ^{64}Cu spectrum is 280 keV (FWHM) and the scattering angle resolution is $\sim$10 mrad (FWHM). From these, absolute differential cross sections for states in ^{64}Cu are determined. The method of indirect normalization attempted using the A1900 Faraday Bar was unsuccessful so the spectrum is normalized by comparison with the ^{12}C

reference measurement. See Chapter 5 for complete details of the analysis procedure and Chapter 6 for the extraction of Gamow-Teller strength in ^{64}Cu.

Chapter 5

Data Analysis

This chapter provides an account of the data analysis procedure. The objective will be to overview the transformation of raw data in the event file into a measured absolute cross section for the ^{64}Zn(t,^{3}He)^{64}Cu reaction. There will be short discussions about additional reactions, taking place with ^{64}Zn, $^{12}CD_2$, and mask target settings, which aid the ^{64}Zn analysis.

For the reader's reference, the analysis procedure is carried out using the Physics Analysis Workshop (PAW) software, version 2.14/04, which is part of the CERN Program Library. PAW executes elementary operations on data in event files from the S800 DAQ based on a user-defined subroutine. However, there are no special functions defined in PAW that affect the analysis. Any analysis package and programming language capable of basic operations should be able to reproduce this result. Therefore, it is the author's intent to make the account presented here transparent to the use of this software, as much as it is possible.

Discussion begins by providing an abbreviated scheme for the many event parameters in the data stream, restricting discussion only to those needed to determine the cross section in ^{64}Cu. The main calibration task in the analysis is to convert center-of-charge (dispersive position) and electron drift time (non-dispersive direction) for event trajectories in the CRDCs into physical lengths using the masked settings for the detectors. Next, the ^{3}He events stemming from reactions on ^{64}Zn will be separated from other reactions

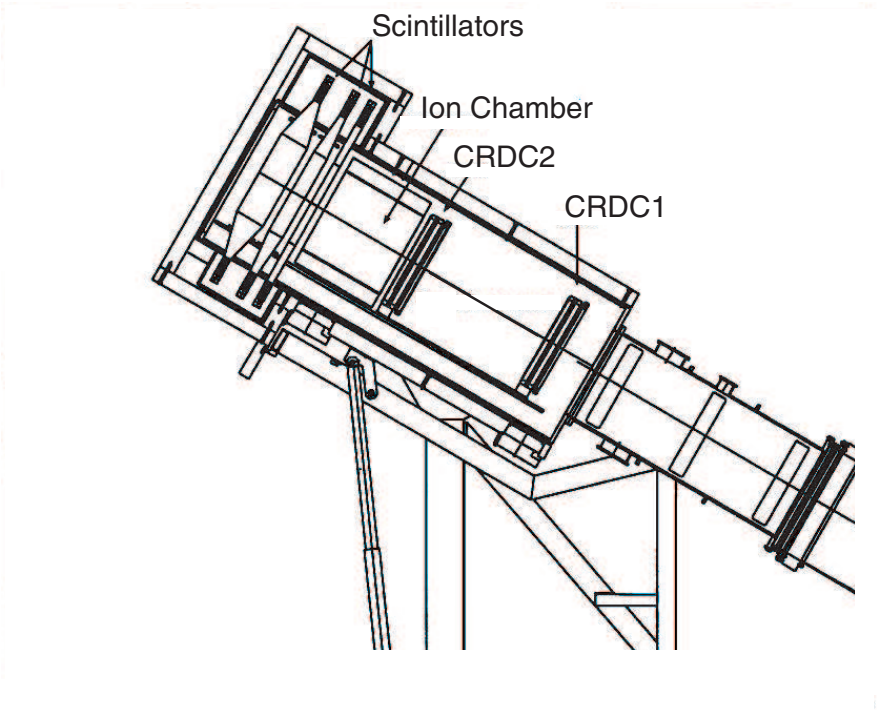

Figure 5.1: Schematic cut-away view of the S800 focal plane detector suite, reproduced from Ref. [126]

in the data stream, with detailed consideration of background sources and background subtractions. Reconstruction of the reaction kinematics at the S800 target position is discussed briefly and interested readers should refer to Refs. [134, 138] for more details. Finally, the $^{12}CD_2(t,^3He)$ reaction to the ^{12}B ground state is examined, for its use as a reference cross section in the absolute cross section normalization.

5.1 Declaration of Parameters

Discussion of the data analysis procedure is aided by defining relevant parameters and signals associated with the S800 focal plane detector suite. Figure 5.1, reproduced from Ref. [126], shows a cut-away view of the S800 focal plane chamber. Fast, beam-like reaction products leave the magnetic sector fields of the S800 spectrograph through the beam pipe at the lower, right hand side of the diagram. The beam direction is indicated near the center of the drawing, showing that particles travel from lower right to the upper left hand sides. Particles entering the focal plane encounter detectors in the following order:

Cathode-Readout Drift Chamber 1 (CRDC1), CRDC2, a Frisch-grid Ion Chamber (IC), and three plastic scintillator paddles (E1, E2, and E3). The specific function of each detector was described in Chapter 4. The concern here is to define each detector's output as it is used for the analysis. The CRDCs measure horizontal ($Y_{1,2}$) and vertical ($X_{1,2}$) positions of impinging particles. Note the reversal of the typical usage of "X" and "Y" as Cartesian coordinates. The dispersive direction (of magnetic deflection) in the coordinate system of a spectrometer is here labeled "X" according to a standard convention. However, the S800 is a vertical spectrometer, so further discussion will use the terms "dispersive" and "non-dispersive" direction to avoid confusion. The ion-chamber does not produce a usable signal in the case of the (t,^{3}He) reaction, since the typical beam-like products are isotopes of hydrogen or helium, which suffer very small energy losses in the fill gas. Each scintillator is read out by two photo-multiplier tubes, one at each end along the vertical length of the scintillator bar. Each phototube provides an energy loss ($\Delta E1_{up,down}$, $\Delta E2_{up,down}$, and $\Delta E3_{up,down}$), and timing signal. In this analysis, only the the E2 energy loss signal from the phototube in the down position is used and is hereafter referred to simply as $\Delta E2$. The timing signal of the E1 scintillator serves as the master trigger for the data acquisition electronics. The time difference between the E1 timing signal and the radio frequency (RF) timing signal of the K1200 cyclotron are taken to assign a relative time-of-flight (TOF_{RF}) to each event. The following then summarizes the list of all the event parameters used in the analysis; (X_1, Y_1, X_2, Y_2, $\Delta E2$, TOF_{RF}). This set of parameters is sufficient to determine the full momentum of each particle registered in the S800 focal plane and by reconstruction determine the cross section in the target-like residue.

5.2 Mask Calibrations

The first step of the analysis is to calibrate the position measurements taken with the two CRDCs. The angles (momentum) of particle trajectories are determined from knowledge of the two positions measurements in terms of physical units. The analysis of spectrograph

data uses software-based, ion-optical reconstruction, rather than physical incorporation of high-order multipole magnets to correct optical aberrations in ion trajectories. Therefore, accurate knowledge of x/y positions and associated angles for each event in the focal plane is crucial for reconstructing events at the reaction target. The calibration is accomplished by periodically taking data with an aluminum sieve-slit (or "mask") plate inserted before one of the CRDCs. Their are two such plates in the focal plane, one for each CRDC, and are used to individually calibrate each CRDC in turn. The plates are both 62.50 cm tall by 35.15 cm wide by 6.35 mm thick and are mounted 70 mm upstream of their respective CRDCs on remote, retractable drives. There is one minor caveat to this calibration procedure which is otherwise a standard procedure for the analysis of all S800 data sets. In the case of the (t, ^{3}He) reaction at 115 MeV/nucleon and forward angles, the ejectile ^{3}He ion also has an energy of approximately 115 MeV/nucleon. Consequently, it's range in aluminum is roughly 36 mm [132], so it will pass through the mask plate whether or not it is incident on a hole/slit in the plate.

Figure 5.2 shows an example mask spectrum, taken during the experiment to calibrate CRDC1. A 1 mm thick, in-beam plastic scintillator (IBS) is used as the reaction target. This greatly increases the ^{3}He intensity in the focal plane and reduces the time needed to measure the mask spectrum since the IBS is is primarily composed of $^{12}CH_2$, which has a large reaction cross section, and is much thicker than the ^{64}Zn or $^{12}CD_2$ foils. The reactions on the scintillator are dominantly on hydrogen in the plastic which produces a characteristic crescent-shape, due to the residual neutron's large recoil energy, centered at $X_1 \approx$ pad 50 and $Y_1 \approx 650$ ns. Another notable feature in the spectrum is the nearby vertical band at $X_1 \approx$ pad 35 which corresponds to the location of one of the slits on the mask plate. Resolving this feature alone is not enough information to calibrate the CRDC. Instead, events which pass through an aperture are distinguished from those which punch through the mask plate by their different energy losses in the E2 scintillator.

Figure 5.3 again shows the dispersive position in CRDC1, as in Figure 5.2 however, on the y-axis the energy loss in E2 is plotted instead. The cause for the slope in the distribution is the location of the phototube converting the scintillation light which is

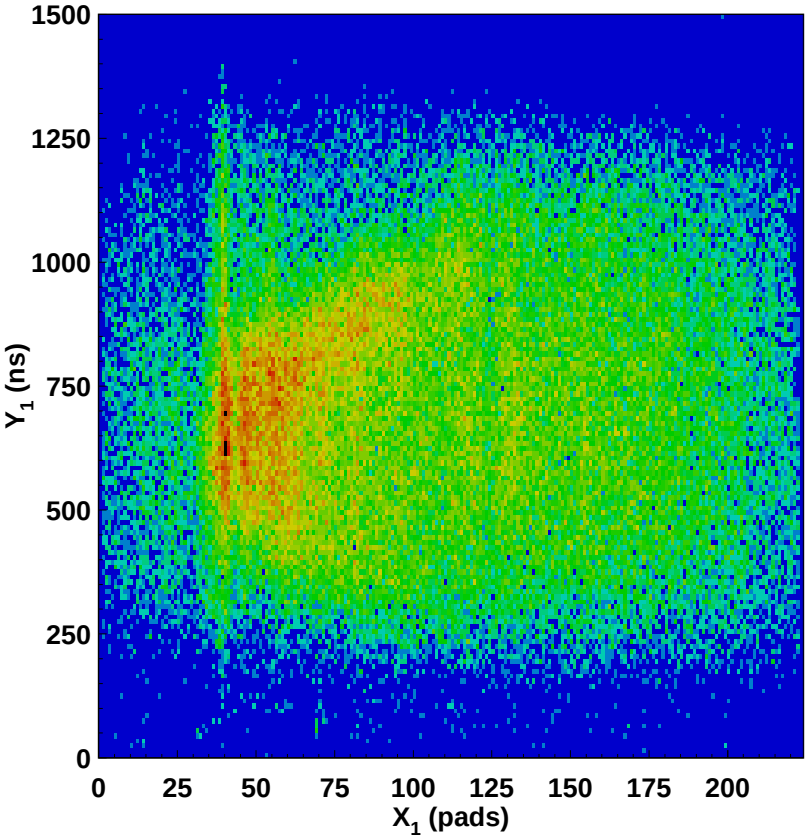

Figure 5.2: The drift time of electrons (Y_1 (ns)) plotted versus pad position (X_1 (pads)) in CRDC1 with a 6.35 mm thick aluminum sieve-slit plate mounted 70 mm upstream over the active area of the detector.

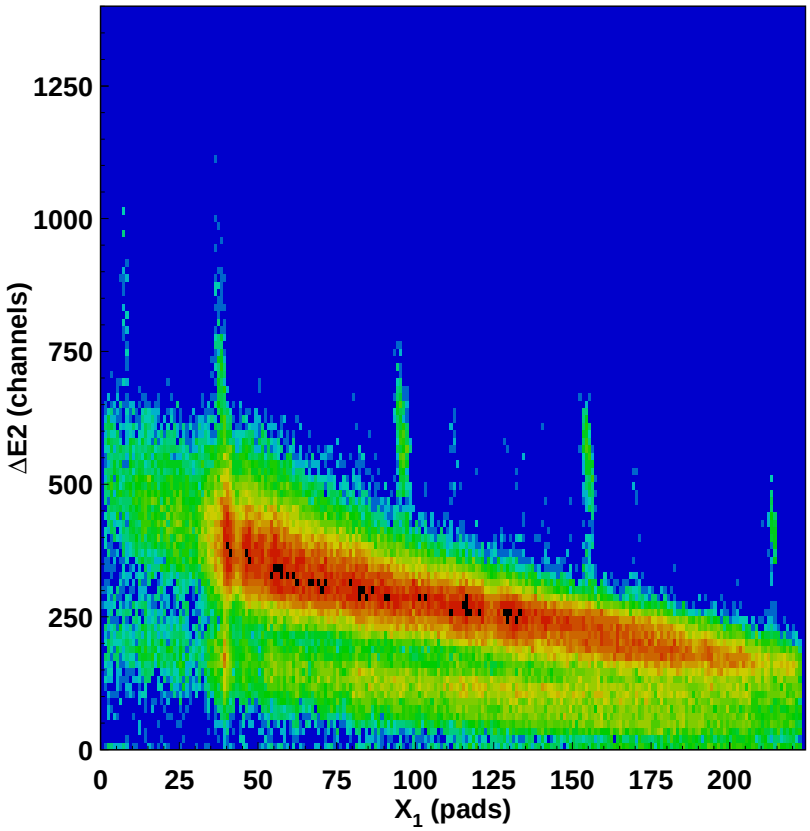

Figure 5.3: Relative energy loss (ΔE2 (channels)) plotted versus dispersive position (X_1 (pads)) in CRDC1 with the 6.35 mm thick aluminum mask installed.

located on the end of the E2 scintillator, corresponding to CRDC positions at the left side of Figure 5.3. The reduction in measured energy loss across the position spectrum then is due to light attenuation in the scintillator bar. There are also two prominent horizontal bands which correspond to different particle charges (Z), the lower band being hydrogen (Z=1, probably deuterons) and the upper band being helium isotopes (Z=2, mostly ^{3}He).

Give particular attention to the narrow, weaker vertical distributions, above the Z=2 horizontal band. They are located approximately above channel $\Delta E2$=650 on the left, to above channel $\Delta E2$=250 on the right and at pads X_1 ≈5, 35, 100, 160, and 215. These roughly correspond to the location of slits in the mask that are spaced across the plate in the dispersive direction. Particles passing through a slit do not suffer an energy loss and therefore will have more energy to deposit when they encounter the scintillator. Applying

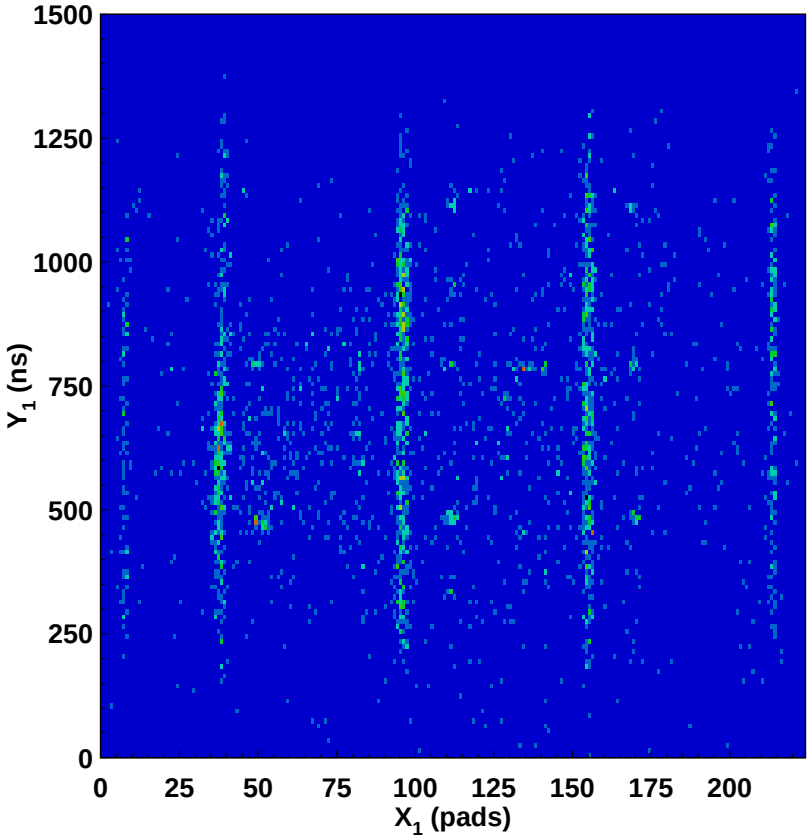

Figure 5.4: The uncalibrated horizontal position (Y_1 (channels)) plotted versus the uncalibrated vertical position (X_1 (pads)).

a gate on this region and setting this as as a filling condition for the spectrum (Figure 5.2) distinguishes particles passing through apertures in the mask from events punching through the mask plate.

Figure 5.4 displays the mask spectrum resulting from applying this energy loss gate. The five slits spaced along the dispersive direction are now clearly visible. Also, the image of several of the rows of holes in the mask are clearly seen, spaced horizontally at approximately Y_1=450, 800, and 1150 ns. The "L"-shaped configuration of holes in the spectrum, just right of center at (X_1 (pad), Y_1 (ns))=(130, 750), is visible but rather faint, partially due to low statistics. Comparison of this spectrum to the design specifications of the mask plate provides a rough calibration of CRDC1 position spectrum. An identical procedure is followed to determine a rough calibration of CRDC2 positions as well, converting from units of (pad, ns) to (mm, mm) linearly:

Run No. of 187	Dispersive		Non-Dispersive	
	m_1(mm/pad)	b_1(mm)	n_1(mm/ns)	c_1(ns)
30	2.54	-281.33	-0.164	132.43
77	2.54	-282.18	-0.166	130.03
109	2.54	-281.70	-0.161	128.10
141	2.54	-281.43	-0.160	126.93
171	2.54	-282.11	-0.163	127.40
Average	2.54	-281.75	-0.163	128.72

Table 5.1: Results of the five CRDC1 calibrations.

Run No. of 187	Dispersive		Non-Dispersive	
	m_2(mm/pad)	b_2(mm)	n_2(mm/ns)	c_2(ns)
31	2.54	-281.73	0.162	-141.06
78	2.54	-281.66	0.167	-141.46
110	2.54	-282.53	0.168	-142.15
142	2.54	-282.12	0.168	-142.52
172	2.54	-282.34	0.165	-139.00
Average	2.54	-282.07	0.167	-141.45

Table 5.2: Results of the five CRDC2 calibrations.

$$X_{1,2}(\text{mm}) = m_{1,2}(\text{mm/pad}) \times X_{1,2}(\text{pad}) + b_{1,2}(\text{mm}) \tag{5.1}$$

$$Y_{1,2}(\text{mm}) = n_{1,2}(\text{mm/ns}) \times \Big(Y_{1,2}(\text{ns}) - c_{1,2}(\text{ns}) \Big) \tag{5.2}$$

Based on this rough calibration, tentative Cartesian angles at the focal plane (A_{FP},B_{FP}) are assigned to each trajectory. Using these angles, trajectories are then traced onto the mask plane, 70mm upstream for each CRDC. The resulting position spectrum at the mask plane is again compared to the mask design. Corrections to the calibration parameters $m_{1,2}$, $n_{1,2}$, $b_{1,2}$, and $c_{1,2}$ are determined iteratively by repeating this process. Tables 5.1 and 5.2 summarize the result of five separate calibrations of the each CRDC. The regularity of the calibration for the dispersive direction in each detector is expected since the physical size of a pad is 2.54 mm and 224 pads are evenly spaced across the dispersive axis of the detector. However, the calibration of the non-dispersive direction is set by the drift time of secondary electrons in the fill gas, which is changed by pressure instabilities

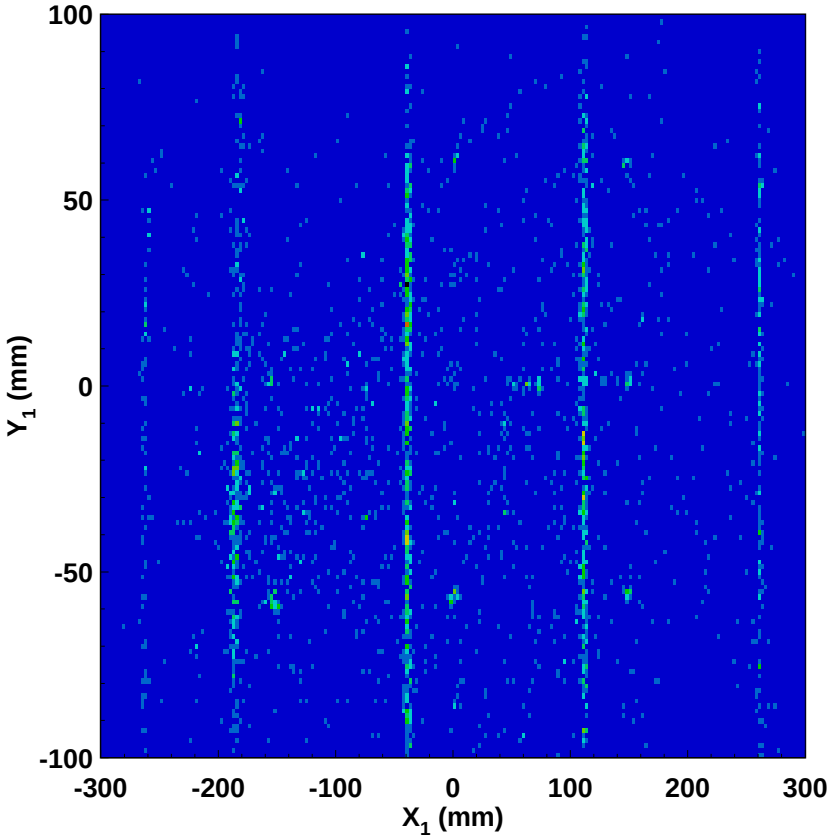

Figure 5.5: The horizontal position (Y_1 (mm)) plotted versus the calibrated vertical position (X_1 (mm)).

in the gas handling system, so it is important to regularly calibrate the non-dispersive direction. Nevertheless, the electron drift time in the fill gas of both CRDCs was remarkably regular over the course of this experiment. Charge-states in the data, which are discussed later, are used to monitor changes to the drift time on a run-by-run basis and verify the stability observed in the mask data. Therefore, the average calibration is applied to all other data taken.

Figure 5.5 shows the result of the full calibration for one of the CRDC1 mask runs. The calibration procedure was repeated to ten iterations, though for most mask runs the values for the calibration parameters are sufficiently converged after 3-4 iterations. Comparing this mask spectrum to the single-iteration spectrum displayed in Figure 5.2 shows qualitatively the result of multiple iterations in the calibrations procedure. Both the slit and holes features in the spectrum are narrower and the horizontal leg of the "L"

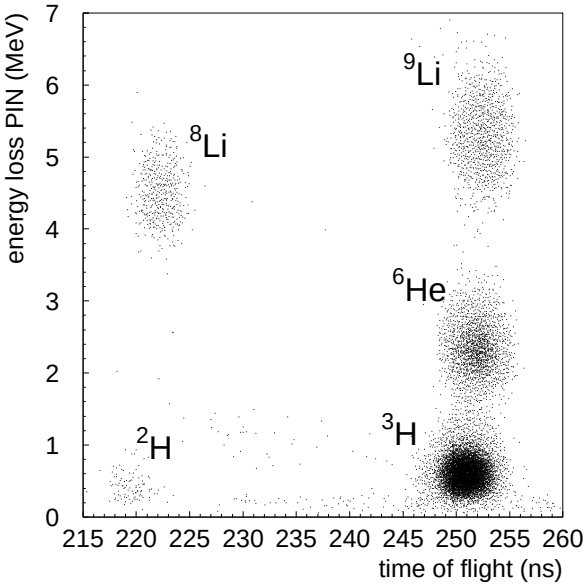

Figure 5.6: The particle identification (PID) spectrum measured in the focal plane of the A1900 Fragment Separator during the triton production experiments: the energy loss in the PIN detector is plotted versus TOF.

configuration of holes, just right of the origin, is now clearly seen. The results for other mask runs, for both CRDCs, are similar.

5.3 Particle Identification

The dispersive position measured in the focal plane dominantly determines the energy of an event in the spectrograph. Corrections to this due to optical aberrations in particle trajectories through the spectrograph are calculated from their angles and non-dispersive positions using a transfer matrix representation of the spectrograph. However, events must first be identified and separated based on which reaction channel they belong to before the data set is useful for spectroscopy.

Recall that the incident triton beam is 85% pure, as seen in the PID spectrum from the A1900 Fragment Separator focal plane in Figure 5.6. The five isotope species seen there; ^{2}H, ^{3}H (t), ^{6}He, and ^{8,9}Li, can make reactions at the S800 target position. Also, the ^{64}Zn and $^{12}CD_2$ foils are are fixed with plastic ($^{12}CH_2$) in a thick aluminum frame around their perimeters. During this experiment, the momentum-dispersed beam spot is

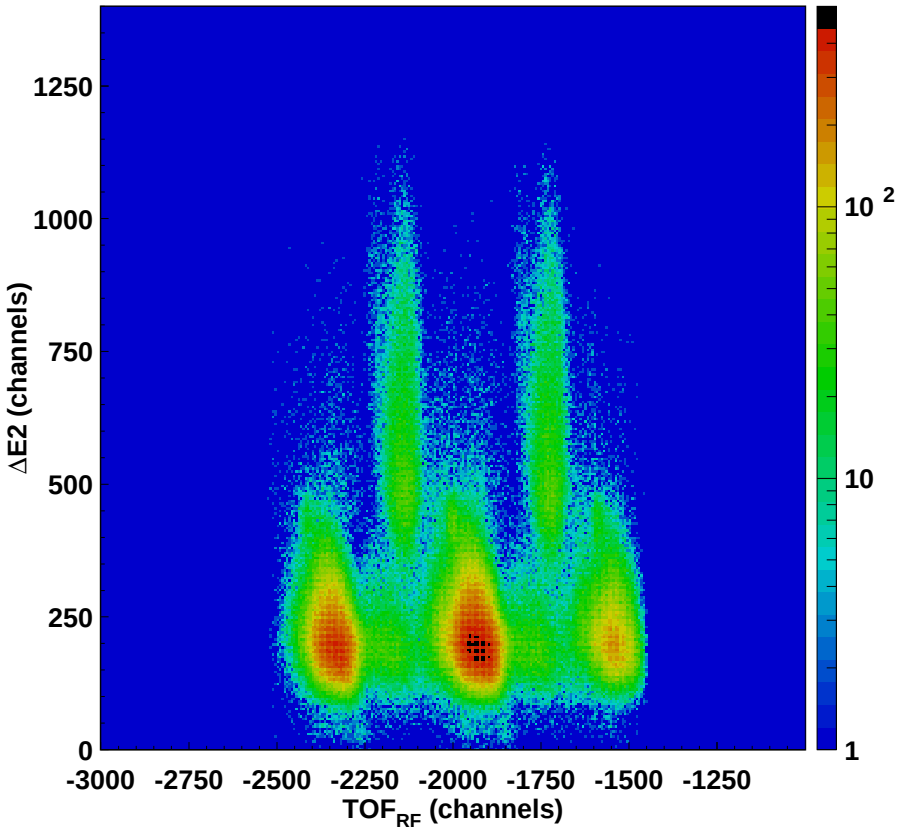

Figure 5.7: Relative energy loss signal (ΔE2 (channels)) plotted versus the raw, relative time-of-flight signal (TOF$_{RF}$ (channels) for particles detected in the S800 focal plane.

approximately 5 cm tall by 1 cm wide, so reactions between the particles in the tail of the beam's spatial distribution and the mounting frame occurred. Therefore, these five isotopes in the incident beam and the materials at the target position (^{64}Zn + ^{27}Al + $^{12}CH_2$) or ($^{12}CD_2$ + ^{27}Al + $^{12}CH_2$) form possible combinations of reaction channels and background sources.

Many of the possible reactions are eliminated from consideration by momentum selection with the spectrograph's magnetic field. For astrophysical purposes, the Gamow-Teller strength determined from Charge-Exchange at low-lying excitation energies is most relevant. For this purpose, the spectrograph's magnetic field is set so that ^{3}He particles with approximately the same energy per nucleon as the beam are included in the momentum acceptance. The triton beam energy was determined to be 114.8 MeV/nucleon based on the magnetic rigidity of the A1900 Fragment Separator. The ground state reaction

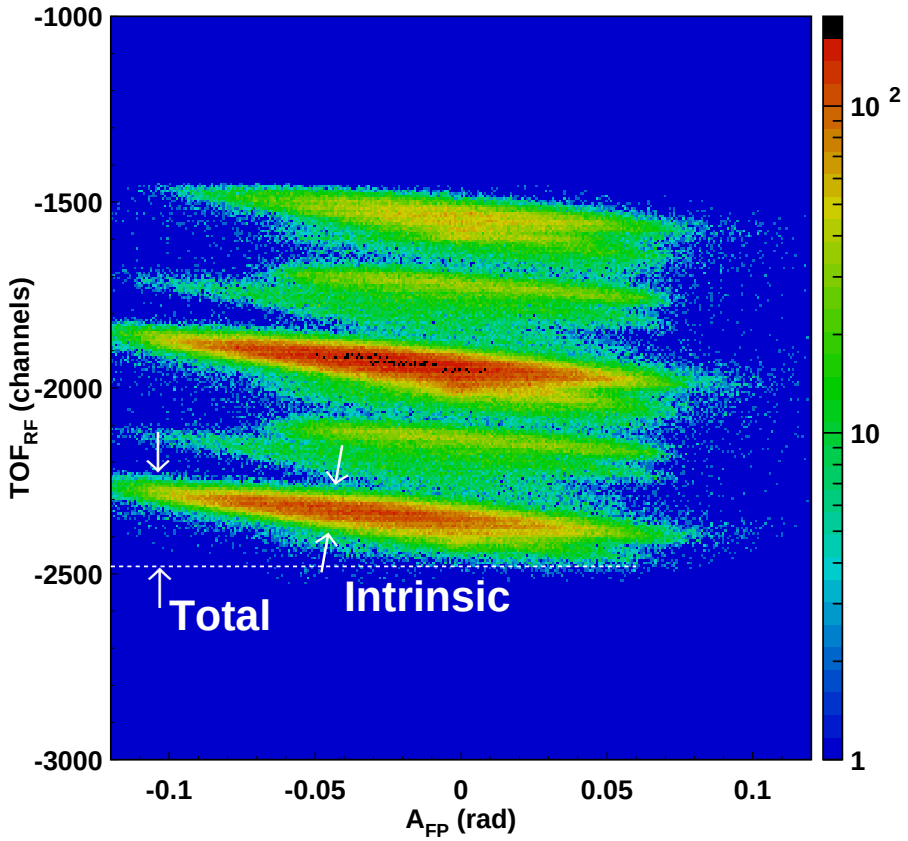

Figure 5.8: Relative time-of-flight (TOF$_{RF}$ (channels) plotted versus the vertical angle (A$_{FP}$ (rad)) for particles detected in the S800 focal plane.

Q-value for ^{64}Zn(t,^{3}He)^{64}Cu is -0.560 MeV, so one anticipates ^{3}He particles from this reaction to have energies at and below 114.6 MeV/nucleon. The energy acceptance of the spectrograph is 10.0% and its magnetic rigidity was set to $B\rho$=2.325 Tm. This corresponds to a ^{3}He energy of 108.95 MeV/nucleon along the central ray, with ^{3}He energies ranging from 92.6 to 125.2 MeV/nucleon across the full acceptance. This choice shifts ^{3}He events associated with the ^{64}Cu ground state in the -X_1-direction by approximately 9 cm and spreads events from ^{64}Cu excited states over the remaining ∼50 cm of active detector area in the +X_1-direction. Excitations in ^{64}Cu up to ∼20 MeV may then be detected within the full acceptance.

These ^{3}He events are distinguished from the few remaining reaction products reaching the focal plane. Figure 5.7 shows the $E2$ energy loss plotted versus the time-of-flight for all events which are accepted into the focal plane. Energy loss by fast ions with

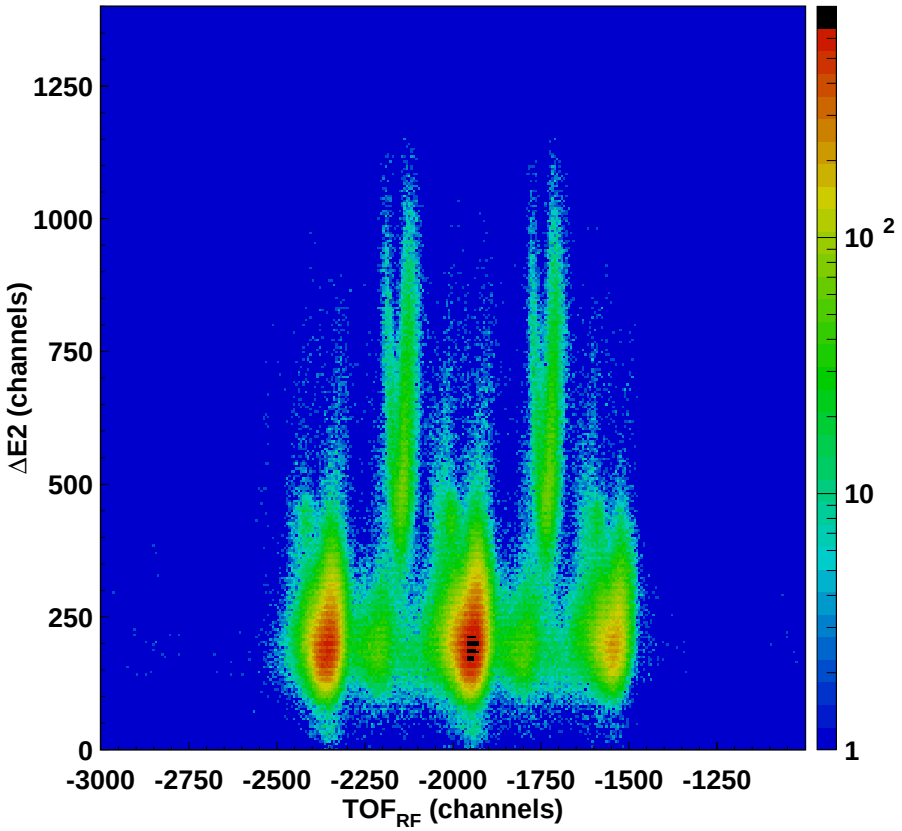

Figure 5.9: Energy loss (ΔE2 (channels)) plotted versus the time-of-flight (TOF$_{RF}$ (channels), compensated for the correlation between time-of-flight and vertical angle.

charge Z in matter is proportional to Z^2 as per the Bethe-Bloch equation [99]. Therefore, increasing energy loss should roughly correspond to increasing charge for peaks in the $\Delta E2$ spectrum. The vertical width of an individual peak is related to the distribution of energies for events of the same species. Multiple RF cycles are included in the spectrum. The two tall vertical peaks correspond to ^{3}He events. However, it is clear from Figure 5.7 that individual peaks are not cleanly separated and there is no indication that weak contaminants are not being obscured. Corrections are calculated for this spectrum that sharpen the peaks by compensating for contributions to the energy and timing width that are not related to the reaction mechanism.

Figure 5.8 again shows the time-of-flight for the same data displayed in Figure 5.7, now plotted against the corresponding dispersive angle in the focal plane. The total width of the TOF distribution contains a contribution which is intrinsic and one which is due to

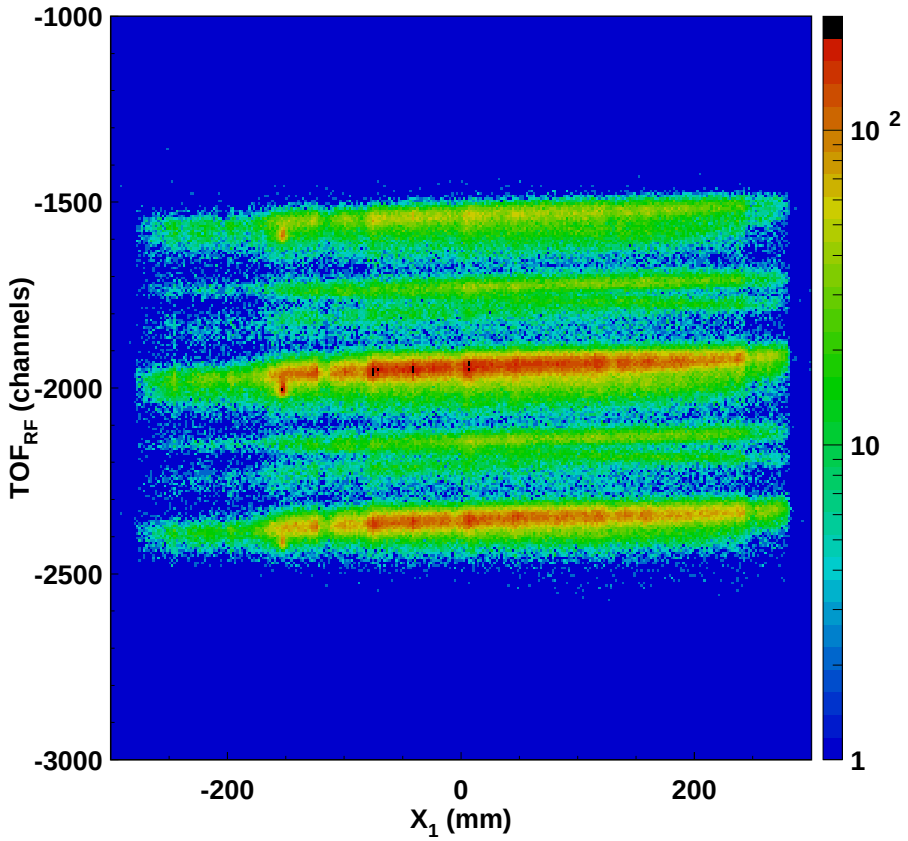

Figure 5.10: The time-of-flight (TOF_{RF} (channels), compensated for the correlation between time-of-flight and vertical angle, plotted versus the vertical position (A_{FP} (rad)).

its correlation with A_{FP}. The overall correlation is negative but different for each band seen, indicating it is different for each particle. This correlation is expected since particles with larger angles relative to the central ray through the spectrograph have followed more eccentric trajectories and therefore have taken a longer time to traverse the distance to the focal plane. Since this contribution to the timing width is optical, the distribution is transformed to remove the correlation such that the width of peaks projected onto the time-of-flight axis is minimized. Not all of the bands can be simultaneously corrected, so at first, the band belonging to ^{3}He is an educated guess. Back-gating on ^{3}He in the corrected PID (shown later) provides verification.

Figure 5.9 again displays the PID spectrum for the events displayed in Figure 5.7, but now uses the event's time-of-flight corrected for the correlation with dispersive angle. As suspected, weaker peaks which were obscured by the width of larger peaks in Figure 5.7

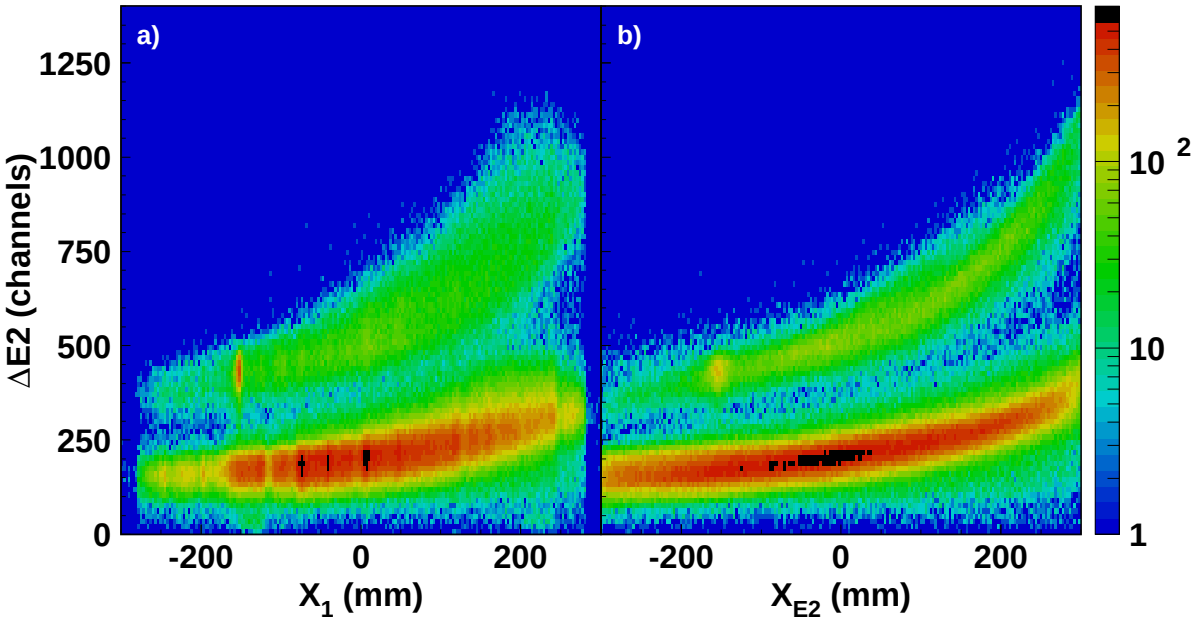

Figure 5.11: Energy losses (ΔE2 (channels)) of particles stopping or passing through the E2 scintillator. a). E2 energy loss plotted as a function the corresponding particle's dispersive position (X_1 (mm)) in CRDC1. b). E2 energy loss plotted as a function of the corresponding particle's dispersive position (X_{E2} (mm)) at the E2 scintillator plane.

begin to emerge. Additional corrections are applied to further clarify the PID spectrum. Figure 5.10 shows the TOF, corrected for its correlation with the dispersive angle, plotted versus the events' corresponding dispersive position. Again, the total width of the TOF distribution has an intrinsic and an optical part. The correlation seen is expected since particles with larger energies will take less time to traverse the distance to the focal plane. Again, the optical contribution to the timing resolution is removed by transforming the distribution so as to minimize the width of the projection onto the TOF axis.

The energy loss signal is similarly corrected for contributions to its width that are unrelated to the reaction mechanism. Figure 5.11 shows the E2 energy loss plotted versus the particles' corresponding dispersive position. In both insets a) and b), there is a generally positive correlation though there are two distinctly different functional relationships. As an aside, it is important to note that ΔE2 is the same phototube signal used in the mask analysis and displayed in Figure 5.3. However, the CRDC1 calibration changes the

sign convention for the dispersive position axis. Again, the correlation between ΔE2 and $X_{1,\mathrm{E2}}$ is largely due to signal attenuation, as light is gathered by the phototube mounted at the $+X$ end of the scintillator. At a given position though, it is clear there are separate possible energy loss signals. These can only come from differences in the charge of species incident on the scintillator.

The energy loss signal is implictly corrected for correlations with event angles in the focal plane by projecting the event position onto the E2 scintillator plane. The two bands are sharpened because particle tracks that have large angles in the focal plane will traverse more scintillator material, suffering larger energy loss, at E2 than events that are incident normal to the E2 surface. Careful comparison of Figure 5.11(a) and (b) confirms this interpretation. One sees that the high-energy tail of the energy loss distribution at a given position comes down as a result of tracing positions from CRDC1 to E2. The low-energy side of the energy loss distribution remains fixed because these particles are incident normal to the E2 surface.

The greater separation between bands in Figure 5.11(b)allows more precise correction of the correlation due to signal attenuation. Each band is separately fitted to determine its ΔE2 centroid as a function of X_{E2}. These functions are then used to remove the correlation due to attenuation and minimize the projection of each band on the ΔE2 axis. Figure 5.12 shows the final PID spectrum for the ^{64}Zn data set, including all corrections. Two multiples of the RF in the time-of-flight signal have been collapsed to place all (t,^{3}He) events (identified later) at the TOF origin. Comparing with the raw PID spectrum in Figure 5.7 shows two distinct bands of relative energy loss; one at approximately ΔE2=200 channels and ΔE2=500 channels, corresponding to ion charges Z=1 and Z=2. One would expect their signal ratio to be 1:4 however, the spectrograph places an energy bias on the PID. Ions represented in the lower band then are likely deuterons. All of these events are clearly separated from ^{3}He candidates in the upper band and are discarded as background to further analysis. The particles in the upper band may possibly be ^{3}He or alphas.

There are five distinct peaks in the Z=2 band of the PID spectrum in Figure 5.12.

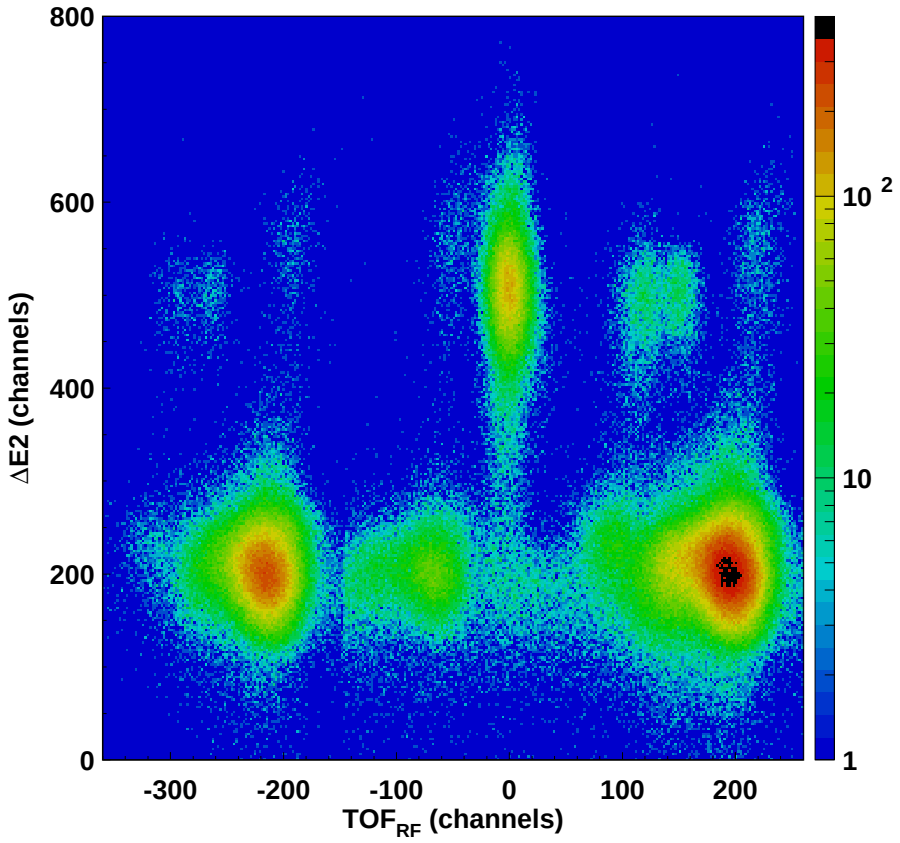

Figure 5.12: The E2 energy loss (ΔE2 (channels)), compensated for different particle charges and pathlengths through the scintillator, plotted versus the relative time-of-flight (TOF$_{RF}$ (channels)), compensated for the correlation with dispersive angle and position.

Particles in the three peaks at TOF<-150 channels are the same as those in the identical three-peak structure at TOF>100 channels. They are simply artifact events remaining from collapsing the multiple RF structures. Of the five peaks at TOF>-100 channels, notice that three peaks have energy loss centroids at ΔE2$\sim$500 (channel) and the remaining two at ΔE2$\sim$550 (channel). This difference is due to the mass-dependence of ion energy losses, indicating that the lower three peaks are due to ^{3}He particles, the lightest possible helium ions. The two peaks at slightly higher energy loss are alpha particles and are hereafter discarded from further analysis. Events associated with the (t,^{3}He) reaction belong to one of the remaining three peaks.

These events are distinguished using their dispersive position spectrum, filed by gating on their peak in the PID spectrum. One is lead to look at this spectrum since the spread in energy loss for two of the peaks is quite similar while the strongest peak at TOF=0 (channel) is quite broad vertically. Figure 5.13 displays the result of placing a gating condition on one of the narrow, upper band peaks in Figure 5.12 and filling focal plane position and angle spectra. Figure 5.13(left) and (center) show the 2D position spectra of these events, in CRDC1 and CRDC2 respectively. Figure 5.13 (right) shows the non-dispersive versus dispersive angle. In all three spectra, the distributions of these events are very narrow, particularly their dispersive positions $X_{1,2}$. The narrow distribution in Figure 5.13 (left) and (center) indicate that these events are monoenergetic and that there was no nuclear scattering with the reaction target. This indicates that these events are ^{3}He charge-states, resulting from capture of atomic electrons in the target. The remaining peak structure in the upper band of the PID spectrum in Figure 5.12, located at TOF$_{\rm RF}$=0 and with broad spread in energy loss, are unambiguously ^{3}He events stemming from nuclear interactions with the target. The charge-state events are useful for calibration purposes but, it is these events that be the subject of the complete analysis.

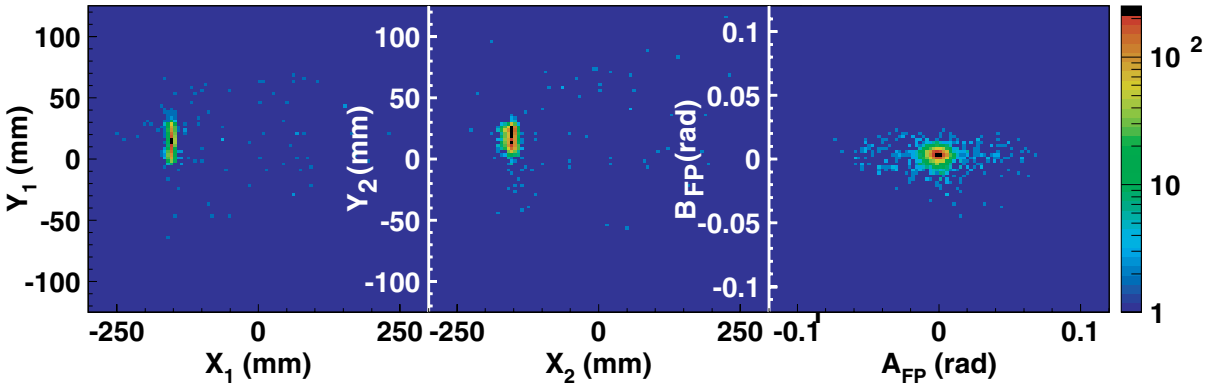

Figure 5.13: Location and emittance of the ^{3}He^{++} charge-state. (Left). The 2D position spectrum of ^{3}He^{++} charge-state events in CRDC1. (Center). The 2D position spectrum of ^{3}He^{++} charge-state events in CRDC2. (Left). The non-dispersive (B_{FP} (rad)) versus dispersive angle (A_{FP} (rad)) of ^{3}He^{++} charge-state events in the focal plane.

5.4 Raytracing through the S800 Spectrograph

The ^{3}He charge-state events, identified in the PID spectrum in the previous section, are useful for calibrating the ray-tracing procedure through the spectrograph. These events are likely due to the production of singly ionized ^{3}He$^+$ particles in the A1900 Fragment Separator since their different TOF means that they cannot be produced in A1900 production target. They are included by the Separator's momentum acceptance since, when singly ionized, they have the same charge-to-mass ratio as the triton but, are then stripped of the remaining electron in the S800 reaction target. These events are useful in several ways. First, since they are nearly monoenergetic and have small scattering angles, they define the beam axis through the spectrograph to high accuracy. Secondly, since they have undergone no nuclear reactions with the target, they are used to set the $Q_{\text{react}} = 0$ MeV point. Furthermore, the intensity of this charge-state is directly proportional to the incident triton intensity. This is a consequence of the triton production target and the reaction target both being above the electron-stripping/capture equilibrium thickness [139]. Therefore, the charge-state events can be used as a surrogate for direct measurement and normalization of the triton beam (which is too rigid to be accepted in the spectrograph). Discussion will return to this point later in the text.

The ray-tracing procedure is enabled by use of a transfer matrix representation of the

S800 spectrograph which is calculated with the ion-optical code COSYInfinity [134]. The technique for kinematic reconstruction and correction of optical aberrations outlined in Ref. [134] is an alternative to physical addition of high-order multipole magnets in the spectrograph. The user specifies the magnetic elements, currents, drift distance and aperture sizes of the S800 spectrograph in the COSYInfinity input file. The code then, by tracing events between the reaction target and the focal plane, calculates fifth-order polynomial expansions of a particle's phase space distributions at the target, in terms of its phase space distributions at the focal plane. For example, the dispersive angle at the target for a particle trajectory is expanded as a fifth-order polynomial in the angles and positions of this trajectory at the focal plane: $A_{\mathrm{TAR}}=f(X_1, A_{\mathrm{FP}}, Y_1, B_{\mathrm{FP}})$. One exception is the dispersive position at the target because the dispersive position information from the focal plane is used to reconstruct the percent energy deviation (D_{TAR}) from the energy of the central ray through the spectrograph. The COSYInfinity output used to effect the ray-tracing procedure with the data is a matrix of coefficients for these polynomial expansions.

The ray-trace procedure implicitly assumes that there are no offsets in the focal plane coordinate system ($X_1, A_{\mathrm{FP}}, Y_1, B_{\mathrm{FP}}$). This is true for the idealized spectrograph represented in the COSYIfinity code. However, a real spectrometer contains small shifts in the alignment of magnetic elements. The charge-state's trajectory is ideal for quantifying these effects and correcting the ray-trace procedure for them. In Figure 5.13, comparing dispersive position distributions X_1 and X_2, an average shift between them of 0.7 mm is seen. The X_2 distribution is corrected by shifting the centroid to match that of the X_1 distribution since CRDC1 is located at the focus. This shift is small, considering the CRDC's position resolution is 2.54 mm (FWHM) in the dispersive direction. In Figure 5.13 (left) and (center), the centroid of the non-dispersive position distributions for both CRDC1 and CRDC2 are shifted, by average values of 13.7 mm and 17.6 mm respectively. These differences are somewhat more significant since the non-dispersive position resolution is 19 mm (FWHM). Correcting these two shifts also corrects the non-dispersive angle B_{FP}. These corrections define the endpoint of the central ray through

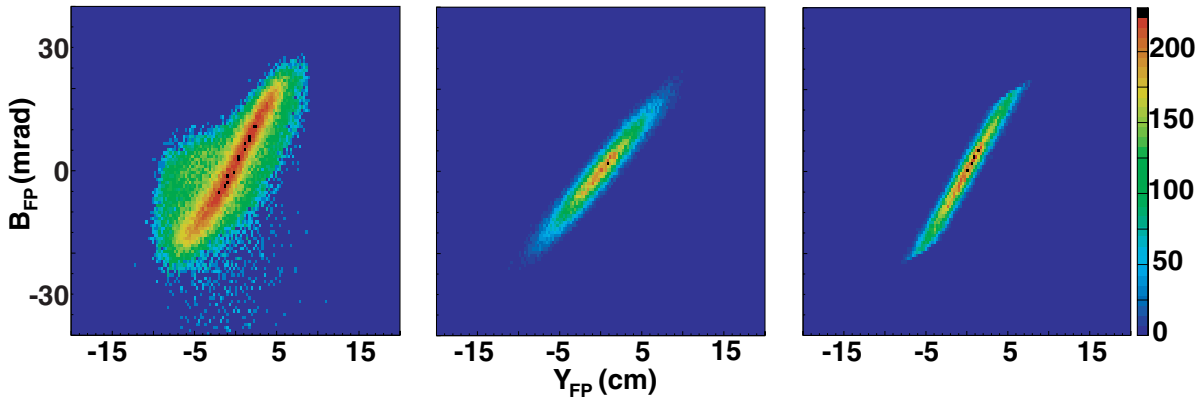

Figure 5.14: Phase space selections, with horizontal angle (B_{FP} (mrad)) plotted versus horizontal position (Y_{FP} (cm)), comparing measured ^{64}Zn(t,^{3}He) events to events simulated in the ion-optical code MOCADI [133]. (Left). The distribution of a subset of measured ^{64}Zn(t,^{3}He) events. (Center). The distribution of events simulated with MOCADI, locating the reaction target along the beam axis as per design specification. (Right). The distribution of events simulated with MOCADI, locating the reaction target 7.0 cm upstream along the beam axis, as compared to design specification.

the spectrograph as the centroid of the charge-state distribution and are applied to all other events.

The endpoint of the central ray must also be clearly defined in order to optimize the ray-tracing procedure. The main ambiguity in the location of the end point at the reaction target is the path length from the focal plane. As the magnetic field of the S800 spectrograph is increased, the size of the fringe fields increase so that the field of the first quadrupole magnet of the S800 encroaches on the target position. Different conventions used by COSY Infinity to account for the fringe field length in the ray-trace matrix differ by as much as several centimeters. Also, there was some ambiguity in the location and alignment of the large scattering chamber at the reaction target. The overall correlation however, between non-dispersive parameters Y_1 and $B_{\rm FP}$, is dominantly due to the optics and should be sensitive to differences in path length.

Figure 5.14 shows the correlation between Y_1 and $B_{\rm FP}$ for ^{3}He events (not the charge-state but the reaction candidates) in the focal plane. The left panel shows the measured correlation. The center and right panels show the same correlation for ^{3}He events simulated with the ion-optical code MOCADI [133]. Similar to light optics with a simple lens,

adjusting the drift length between the target and the fringe field of the first quadrupole in the MOCADI simulation adjusts the correlation between Y_1 and $B_{\rm FP}$. In Figure 5.14 (left), the correlation in the data is 3.67 mrad/cm. In the center panel, the correlation seen in simulation is 2.24 mrad/cm when the input is based on the S800 design specification (the same used to build the COSYInfinity input). Increasing the trace length to the target by 7 cm conforms the simulation to data, shown in the right panel.

The ray-trace procedure is carried out with the corrected central ray location and path length. From the focal plane parameters $(X_1, A_{\rm FP}, Y_1, B_{\rm FP}$ the target parameters $(D_{\rm TAR}, A_{\rm TAR}, Y_{\rm TAR}, B_{\rm TAR}$ are calculated for each event. The scattering angle in the laboratory frame $(\Theta_{\rm lab})$ of an event is calculated from its dispersive and non-dispersive (Cartesian) angles as follows

$$\Theta_{\rm lab} = tan^{-1}\left(\sqrt{tan^2(A_{\rm TAR}) + tan^2(B_{\rm TAR})}\right). \tag{5.3}$$

Finally, the excitation energy (E_X) in the target-like residue is determined by a missing mass calculation. As a convention, let X indicate the target-like residue species, a the beam-like ejectile, Y the target-like reactant, and b the beam species, so that a reaction in general is represented as

$$b + Y \rightarrow X + a. \tag{5.4}$$

The missing mass $m_{\rm miss}$ is then related to the excitation energy by

$$E_X = m_{\rm miss} - m_Y, \tag{5.5}$$

where the missing mass has contribution from missing energy and missing momentum

$$m_{\rm miss} = \sqrt{E^2_{\rm miss} - \vec{p}_{\rm miss} \bullet \vec{p}_{\rm miss}}. \tag{5.6}$$

The missing energy is that energy missing from the beam and participant masses in the reaction

$$E_{\mathrm{miss}} = E_b + m_b + m_Y - E_a - m_a, \tag{5.7}$$

where the ejectile energy E_a in terms of the central energy of the spectrograph (E_{S800}) is

$$E_a = (1 + D_{\mathrm{TAR}}) \times E_{\mathrm{S800}}, \tag{5.8}$$

and the associated missing momentum in Cartesian components is

$$\vec{p}_{\mathrm{miss}} = \vec{p}_b - \vec{p}_a = \begin{pmatrix} -\sqrt{(E_a + m_a)^2 - m_a^2}\sin A_{\mathrm{TAR}} \\ -\sqrt{(E_a + m_a)^2 - m_a^2}\sin B_{\mathrm{TAR}} \\ \sqrt{(E_b + m_b)^2 - m_b^2} - \sqrt{(E_a + m_a)^2 - m_a^2}\cos\Theta \end{pmatrix}, \tag{5.9}$$

The masses used are taken from the recent atomic mass evaluation of Audi, Wapstra and Thibault [140, 141]. The magnetic rigidity of the A1900 Fragment Separator gives a beam energy of E_b=345 MeV. The energy of the central ray in the spectrograph is also determined from the magnetic rigidity to be E_{S800}=326.848 MeV ($B\rho$ = 2.325 T·m). In both cases however, the magnetic field can be measured accurately but there is some ambiguity in the bending radii. Therefore, by taking the charge-state's location in the focal plane to be the Q_{react}=0 point, the beam energy is adjusted to E_b=337.0 MeV to match with what is seen in the spectrograph. The choice is arbitrary and adjusting the S800 central ray to match the A1900 would produce the same result.

The excitation energy and scattering angle is used to isolate events resulting from reactions with the ^{64}Zn target foil. Recall that the foil is mounted in an aluminum frame with plastic. Also, the foil will almost certainly contain hydrogen absorbed from exposure to the atmosphere. Figure 5.15 (top-left) shows the ^{3}He scattering angle plotted against the excitation energy in ^{64}Cu. Two features immediately suggest background contamination of the ^{64}Cu spectrum. The first and most significant is the curved band of events, starting near the origin (Θ_{lab}=0°, E_X=0 MeV) and creating an arc that goes

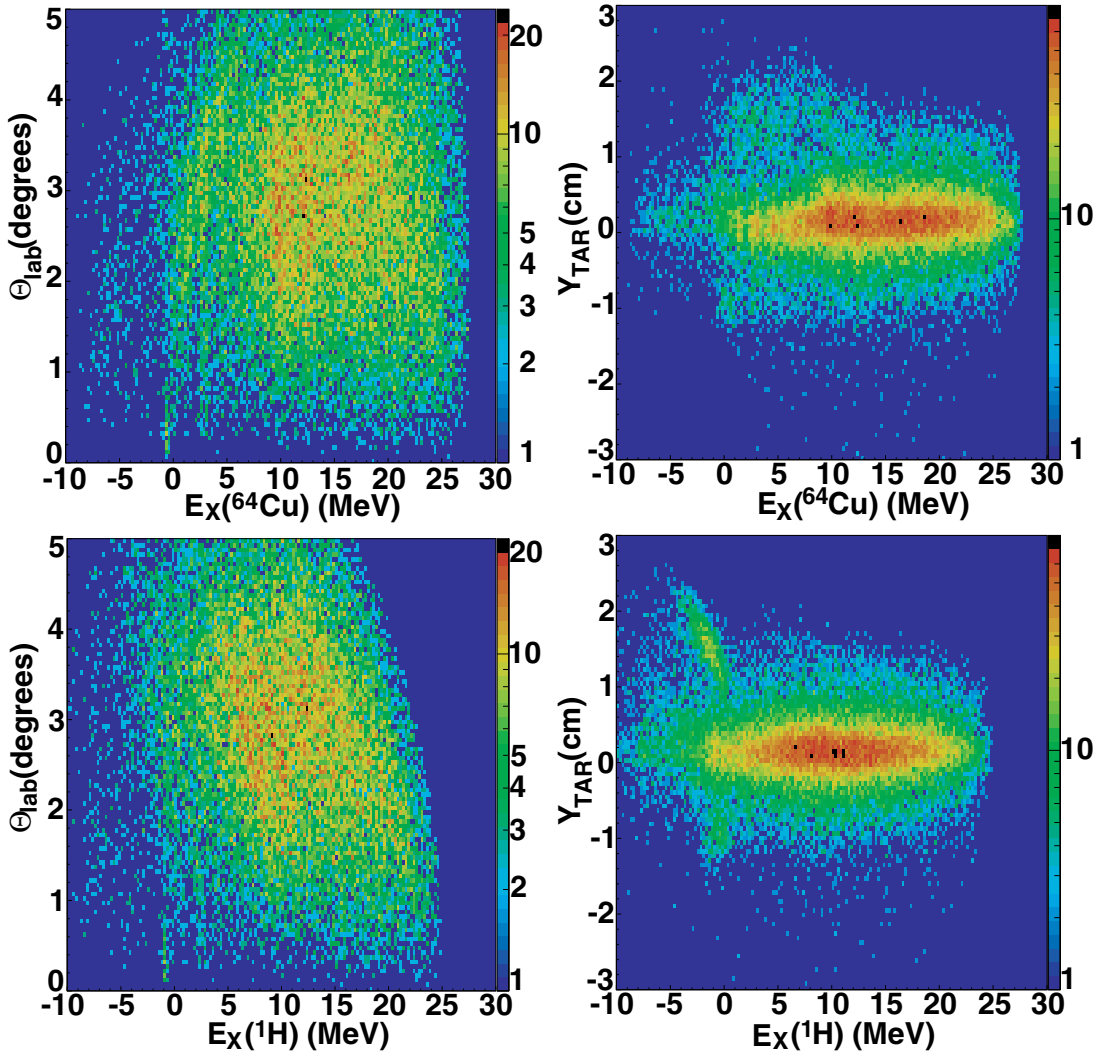

Figure 5.15: (Top-left) The ^{3}He scattering angle plotted as a function of ^{64}Cu excitation energy. (Top-right) Y_{TAR} distribution of ^{3}He events plotted as a function of ^{64}Cu excitation energy. (Bottom-left) The ^{3}He scattering angle plotted as a function of ^{1}H excitation energy. (Bottom-right) Y_{TAR} distribution of ^{3}He events plotted as a function of ^{1}H excitation energy.

to positive excitation as one looks at larger scattering angles. This arc is characteristic of reaction on hydrogen in/near the target. When the masses for the ^{64}Zn(t,^{3}He)^{64}Cu reaction are taken in the missing mass calculation of Equation 5.6, states in ^{64}Cu will appear as vertical bands because the recoil energy is correctly compensated for as a function of scattering angle. Reactions on the much lighter protons leave neutrons that have large recoil energies and thus the pronounced arc.

In Figure 5.15 (top-right), the non-dispersive distribution of ^{3}He positions at the target is plotted as a function of excitation energy in ^{64}Cu. The intensity distribution of the incident triton beam intuitively should have a step-function profile, falling off quickly past $Y \sim \pm 1$ cm, though with some weak tail in the distribution due to beam halos. The intensity in these tails is small, but when incident on plastic (hydrogen) at the edges of the target frame, the large cross section for H(t,^{3}He) reactions compensates for small triton rate. At two positions in Figure 5.15 (top-right), at approximately Y_{TAR}=1.5 cm and -1.0 cm, one sees events at the same excitation energy that the curved band in Figure 5.15 (top-left) occupies. Recalculating the excitation energy for reactions on hydrogen correctly compensates for the neutron recoil. The result is displayed in Figure 5.15 (bottom-left) shows this correlation is straighted (and events from the target foil are now curved), confirming that these events are from hydrogen. Re-plotting the Y_{TAR}-distribution against the excitation energy in Figure 5.15 (bottom-right), reveals sharp peaks at the positions previously mentioned. Since this hydrogen background is spatially localized, gating on small values for Y_{TAR} (-0.60 cm $< Y_{\mathrm{TAR}} <$ 0.85 cm) remove these events. Figure 5.16 shows the result of applying this gate. The excitation energy, plotted against the scattering angle as in Figure 5.15 (top-left) is now clean of the majority of events from hydrogen.

5.5 Background Subtraction

There are two additional sources of background, suggested by events below $E_X = 0$ in Figure 5.16 which have unphysical energies for the ^{64}Zn(t,^{3}He)^{64}Cu reaction. One part

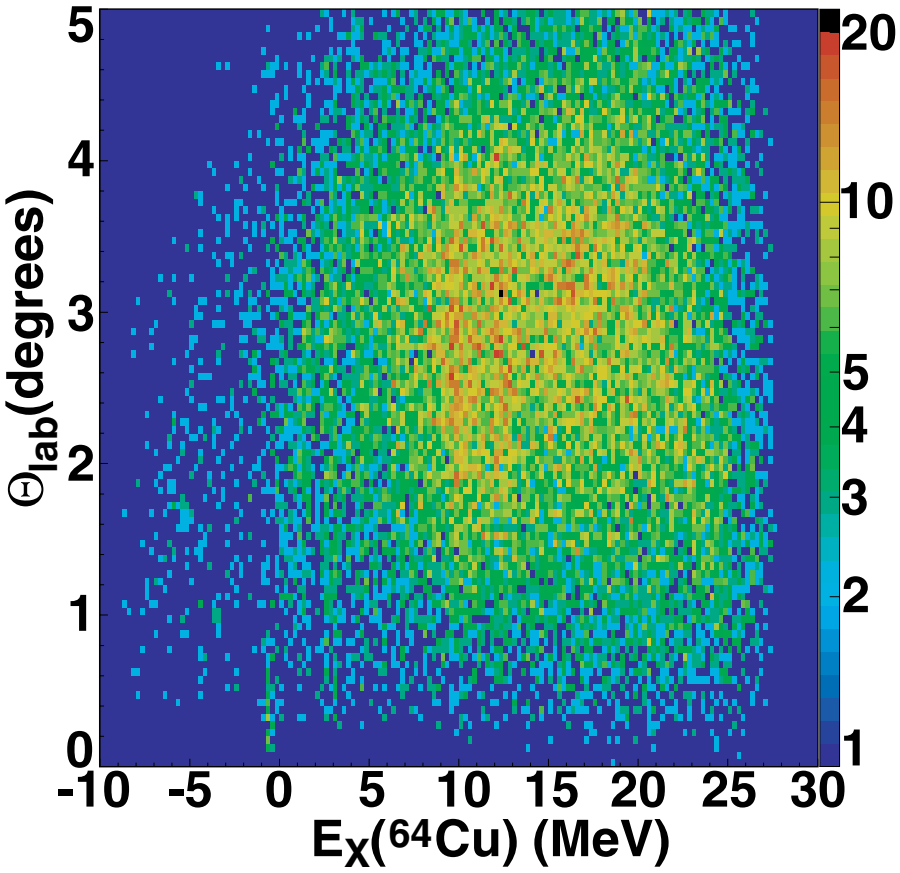

Figure 5.16: The ^{3}He scattering angle plotted as a function of ^{64}Cu excitation energy, gated on events with -0.60 cm $< Y_{\mathrm{TAR}} <$ 0.85 cm.

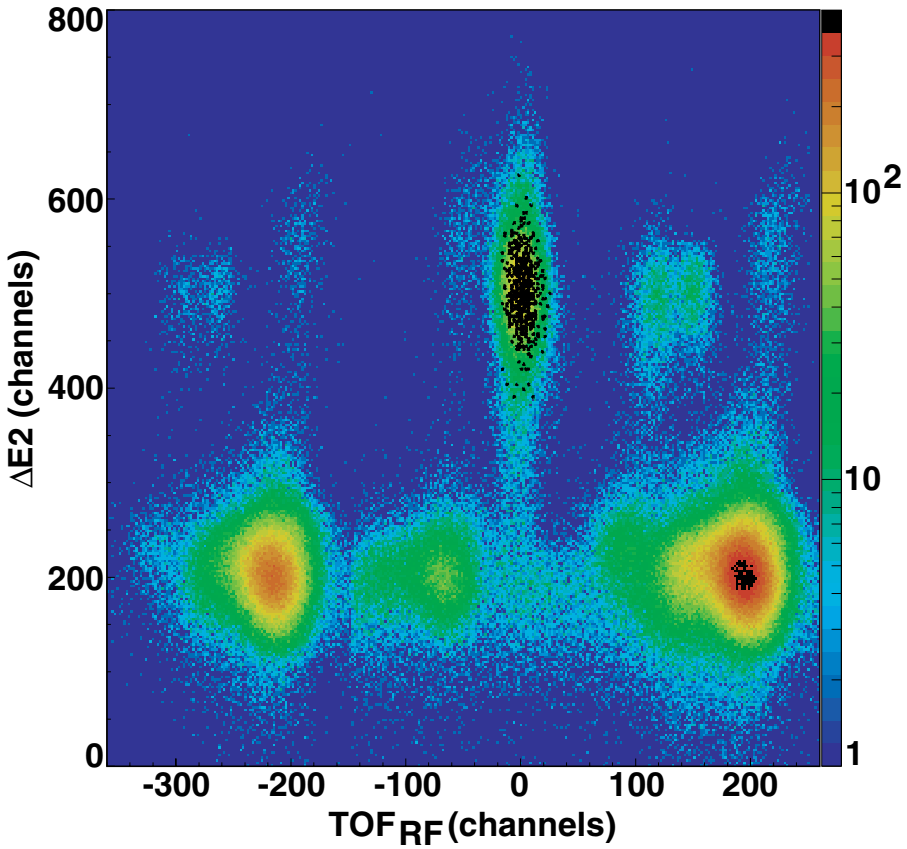

Figure 5.17: The PID spectrum with charge-state events seen in Figure 5.16 overlaid as black points.

of the background is evenly spread over all scattering angles and the other is seen just below $E_X = 0$, at very forward angles. Calculating the cross section for the broad group of events reveals that their angular distribution is flat. Later studies have revealed that this background is caused by ^{6}He contaminants in the triton beam which undergo 3-neutron removal to make ^{3}He. Since this reaction has a many-body exit channel, the ^{3}He energy distribution is wide and events are evenly spread over the full area of the CRDCs. Introduction of a wedge degrader in the A1900 Fragment Separator has, since the time of this measurement, shown that these contaminants are removed completely. For this analysis, a simulated background with flat cross section at all excitation energies is normalized to those events below $E_X = 0$ then subtracted from the total spectrum.

The second source of background, the narrow peak below $E_X = 0$, is a second, weaker ^{3}He charge-state. Like the first charge-state identified, it is nearly monoenergetic and very

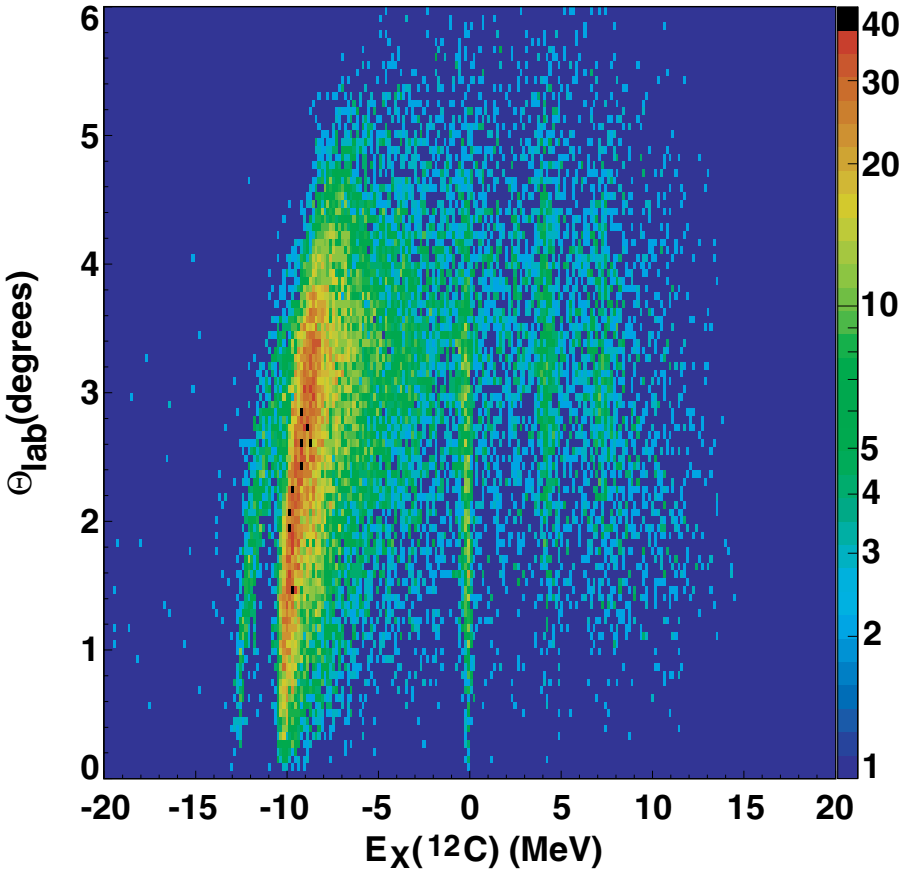

Figure 5.18: The ^{3}He scattering angle plotted as a function of ^{12}C excitation energy, for (t,^{3}He) reactions on the $^{12}CD_2$ target.

forward peaked in scattering angle. Back-gating the PID spectrum in Figure 5.12 on this charge-state however, shows they have a different TOF from the first ^{3}He charge-state. This is displayed in Figure 5.17 which has black points overlaid on the PID spectrum for these charge-states events. They have the exact same TOF as the ^{3}He events from reactions on the ^{64}Zn target which is partially why they weren't discovered earlier in the analysis. Also, identical TOF means this charge-state is created in the reaction target and is a by-product of the original fragmentation reaction, not an interaction somewhere else in the A1900 or Transfer Hall beamlines. It is subtracted by using the first charge-state as a model.

5.6 Normalization to Absolute Cross Section

The last step to determine the absolute reaction cross section in ^{64}Cu is the normalization. The equation below summarizes the ingredients in a measured cross section:

$$\frac{d\sigma}{d\Omega_{\text{lab}}} = \frac{N_{\text{events}}}{N_{\text{beam}} N_{\text{target}}} \times \frac{1}{d\Omega_{\text{lab}}} \tag{5.10}$$

The number of events N_{events} is integrated from the background subtracted spectrum for a given scattering angle interval. The corresponding opening angle $d\Omega_{\text{lab}}$ subtended by the scattering angle is determined from a simple geometric integration. The number of target particles N_{target} is known from the target thickness. The number of incident tritons N_{beam} has been the most difficult to determine. Efforts were made during the experiment to correlate current on the A1900 D1 Faraday bar, used as a beam dump for some of the unreacted ^{16}O primary beam, with rate on the in-beam scintillator at the S800 target position. In much the same way that data were periodically taken to calibrate the CRDCs with mask plates, the rate at the beam dump and the S800 target were periodically calibrated against one another. Since the rate at the beam dump current can be measured during regular measurements, it was thought that knowing its correspondence with the rate at the S800 target would allow the triton intensity to be indirectly monitored. The charge-state events are an additional relative measure of the beam intensity. Analysis of this calibration data for the direct triton intensity however, shows the absolute scale was not reliable. Most likely, the S800 target scintillator's bias voltage was not properly optimized, causing the scintillator to count noise and thus overestimate the triton rate at the target. This is solved in a later experiment, through comparison of the ^{12}C(t,^{3}He) reactions rates, which provides a correction by way of scaling factor. This relative measurement is reliable since comparison with the relative charge-state yields render the same scaling factor.

Data taken on a $^{12}CD_2$ target is used a reference measurement to normalize the ^{64}Cu cross sections instead, comparing it to the later measurement with a $^{12}CH_2$ target. Figure 5.18 shows the scattering angle versus excitation energy in ^{12}C for the $^{12}CD_2$(t,^{3}He)

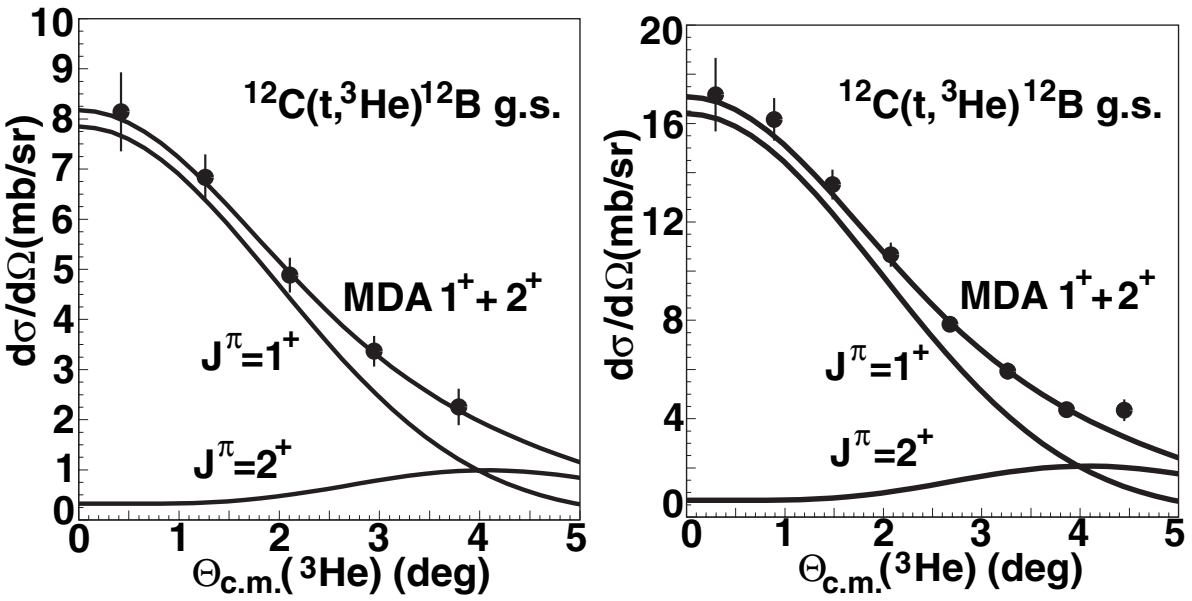

Figure 5.19: Differential cross section of the transition from ^{12}C 0^+ ground state to ^{12}B 1^+ ground state via the (t,^{3}He) reaction. (Left) This cross section as measured during the ^{64}Zn(t,^{3}He) experiment. (Right) The same cross section measured during a later experiment with the correct normalization.

reaction measured alongside ^{64}Zn. All corrections taken here are the same as discussed for ^{64}Zn target data. The transition to the ^{12}B ground state is a strong, known Gamow-Teller state, seen clearly at $E_x = 0$. The two excited states in ^{12}B, the 2^- state at 4.4 MeV and the 1^- at 7.7 MeV, are also clearly seen. Events below $E_x = 0$ come from (t,^{3}He) reactions on deuterons (strong arc) and protons (weaker arc). The arc from deuterons is broader since the residue di-neutron is particle unbound. The ground state differential cross section is determined using the indirect normalization method described above, then compared to the later measurement of the same state which is properly normalized.

Figure 5.19 compares the ^{12}B ground state differential cross section from this measurement (left) with the properly normalized reference measurement (right). The shapes are consistent however, the normalization for the present data is smaller by a factor 2.1±0.13. This error is determined from comparing their fit to a $\Delta L = 0$ distribution, calculated in the DWBA code FOLD [114] for the corresponding $0^+ \rightarrow 1^+$ transition. Therefore, since the all other spectrograph settings are identical for $^{12}CD_2$ and ^{64}Zn target settings, the ^{64}Cu differential cross sections are scaled by this same factor. Lastly, there is strong

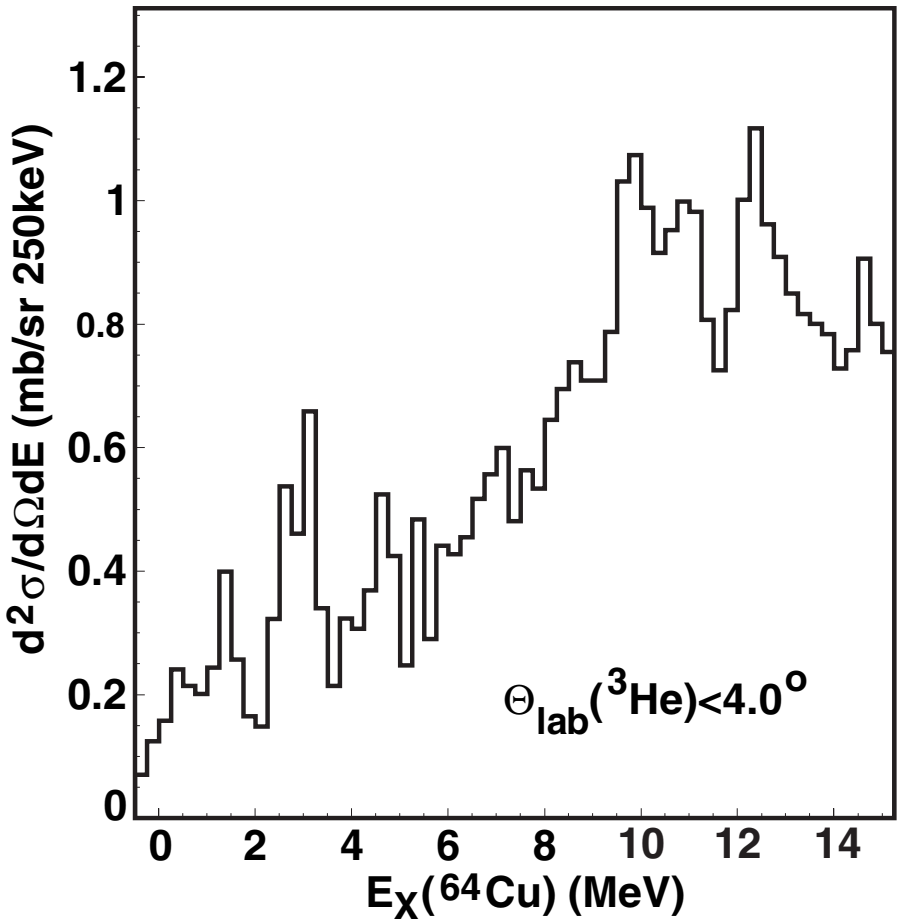

Figure 5.20: The doubly differential cross section of states in ^{64}Cu, plotted as a function excitation energy and gated on events with $\Theta_{\rm lab}(^3{\rm He})$ <4.0°

evidence that the later measurement is a reliable reference. In the following chapter, the Gamow-Teller strength is extracted by taking advantage of a mass-dependent proportionality between cross section and B(GT), determined from the large body of (^{3}He,t) charge-exchange data. The larger of the two ^{12}B ground state cross sections (Figure 5.19 (right)) is consistent with the (^{3}He,t) systematics over a large mass range. This is strong evidence that indeed, Figure 5.19 (left) is an outlier and Figure 5.19 (right) is a reliable reference cross section.

This concludes discussion of the analysis from the measurement of excitations in ^{64}Cu via the ^{64}Zn(t,^{3}He) charge-exchange reaction. Figure 5.20 shows the excitation energy spectrum, with doubly differential cross sections for states in ^{64}Cu plotted as a function of excitation ^{64}Cu. The energy resolution achieved is 280 keV and the scattering angle resolution is $\sim$10 mrad (FWHM). There are three to four distinct excitations seen at and below 5 MeV and two near 10 MeV which are likely dipole resonances. The resolution is not high enough to resolve individual states however, so analysis of cross sections and extraction of Gamow-Teller strength in ^{64}Cu, discussed in the following chapter, will be carried out in a bin-by-bin rather than state-by-state fashion.

Chapter 6

Results

In this chapter, attention will turn from the determination of the differential cross section, to the extraction of the Gamow-Teller operator strength in ^{64}Cu. This determination is facilitated by an empirical proportionality, first suggested by Alford *et al.* [28] and later formalized by Taddeucci *et al.* [32], between the differential cross section and the Gamow-Teller strength in the limit of vanishing momentum transfer. Stated succinctly, the proportionality is:

$$\left.\frac{d\sigma}{d\Omega}\right|_{q\to 0} = \widehat{\sigma}_{\mathrm{GT}} B(\mathrm{GT}) \tag{6.1}$$

where the constant $\widehat{\sigma}_{\mathrm{GT}}$ is called the Gamow-Teller "unit cross section". It is expressed by Taddeucci *et al.* as $\widehat{\sigma}_{\mathrm{GT}} = KN_D|J_{\sigma\tau}|^2$, where K is a kinematic factor in the reduced masses of the entrance and exit channels, N_D is a distortion factor describing the distortion of incoming and outgoing waves in the Coulomb field of the target, and $|J_{\sigma\tau}|^2$ is the volume integration of the radial dependence of the $V_{\sigma\tau}(r)$ term in the effective nucleon-nucleon interaction.

Using Equation 6.1 requires determination of the unit cross section which can be done using one of three methods. The first method is to explicitly calculate $\widehat{\sigma}_{\mathrm{GT}}$ in a DWBA calculation. However, the result is usually of insufficient accuracy and depends on the description of the reaction mechanism. The second method requires a strong,

well-separated GT-state where the corresponding B(GT) is known from β-decay. The normalization determined by comparing the β-decay B(GT) to the measured cross section is then taken as $\widehat{\sigma}_{\rm GT}$ overall. This is the method most often used in the literature but, as discussed at the end of this chapter, one that has an important drawback concerning the systematic error analysis. The third method uses the mass-dependent trend for the unit cross section from the (^{3}He,t) reaction [110] and is applied here. The last two are ideally model-independent methods, since both are normalized to β-decay strength. The chapter concludes by examining sources of systematic error in Equation 6.1 for the ^{64}Cu case.

6.1 Multipole Decomposition Analysis

Figure 6.1 shows a basic scheme for the application of the multipole decomposition analysis (MDA) technique. Gamow-Teller states are distinguished from other transitions by their $\Delta L = 0$ angular distributions which peak at 0° scattering angle. Gating on small scattering angles, Figure 6.1 (b) shows a potential GT state peaking just above 3.1 MeV. Conversely, gating on scattering angles around 2.8°, as in Figure 6.1 (c), shows a potential dipole state ($\Delta L = 1$) near 10 MeV. The MDA distinguishes transitions based on shape in this way, yet other candidate GT states are difficult to distinguish, as the energy resolution is generally not sufficient to separate individual states. Therefore, determination of the GT cross section and associated B(GT) is performed on a bin-by-bin basis.

Figure 6.2 shows a selection of angular distributions associated with transitions to J^π states in ^{64}Cu due to the ^{64}Zn(t,^{3}He) reaction. The cross sections have been calculated in the DWBA using the code FOLD [114]. It is important to note that the absolute cross section determined by FOLD is not used in the MDA, which allows the normalization to vary as a free fit parameter (see previous discussions on exchange in Chapter 3). Therefore, the curves are displayed with arbitrary normalizations. The ^{64}Zn ground state has J^π=0^+ so Gamow-Teller transitions are to J^π=1^+ states in ^{64}Cu. This is reflected in the forward-peaking, $\Delta L = 0$ shape seen in the J^π=1^+ curve in Figure 6.2. The flat

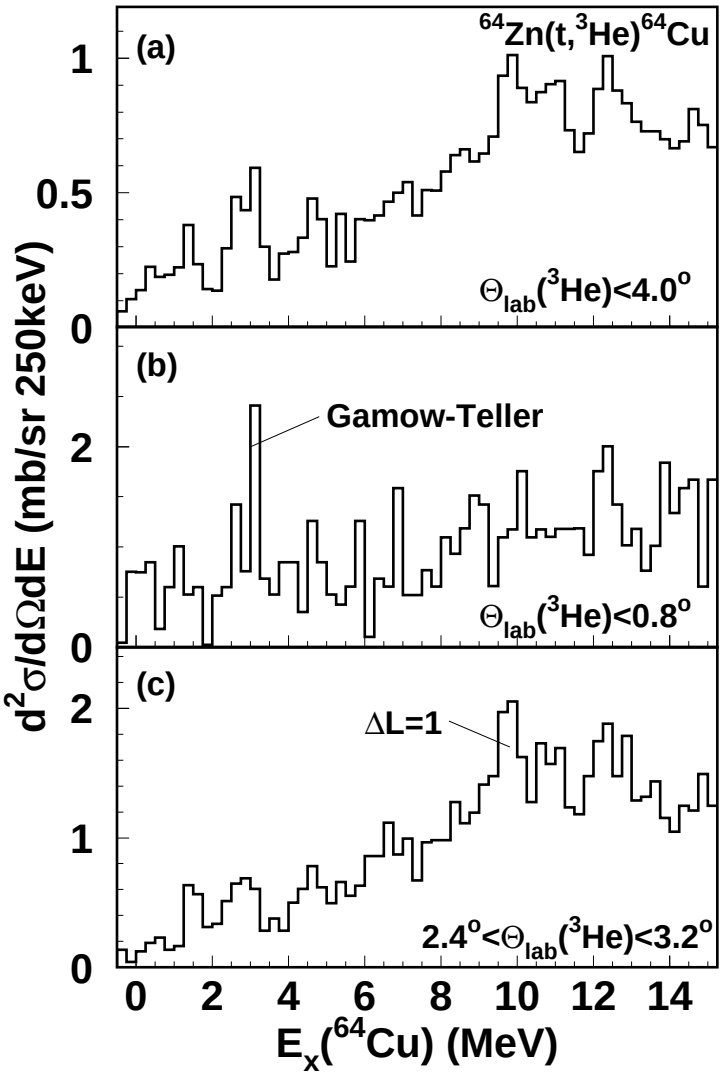

Figure 6.1: Doubly differential cross section of the ^{64}Zn(t,^{3}He)^{64}Cu reaction, plotted as a function of excitation energy in ^{64}Cu. (a) For all events, up to 4.0° in scattering angle. (b) Events near 0° scattering angle. (c) Events around 2.8° scattering angle.

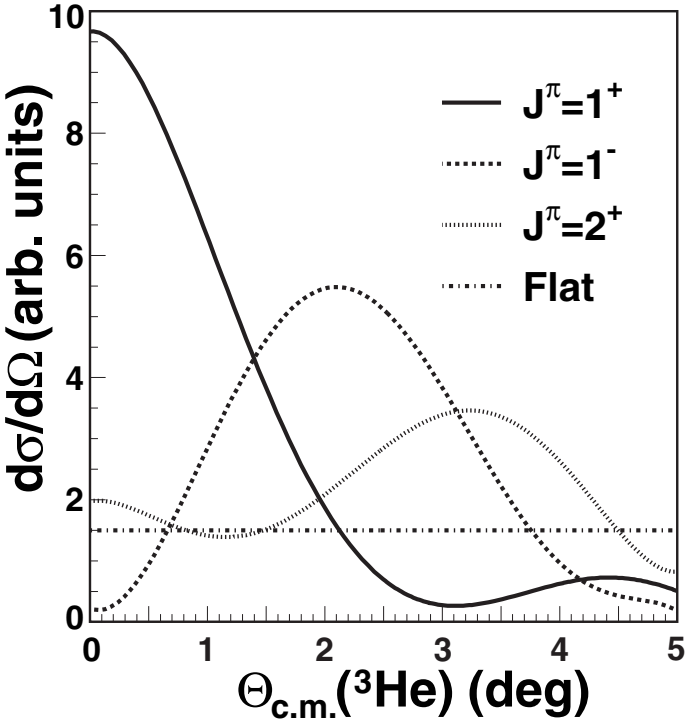

Figure 6.2: A sample selection of differential cross sections calculated in the DWBA code FOLD [114].

distribution is included to approximate larger angular momentum transfers, which are difficult to differentiate due to low statistics, and the quasi-free continuum, onset at the ^{64}Cu proton separation energy S_p ≈7.201 MeV. Formally, the angular distributions here certainly do not form a complete set. Under the conditions present in the experiment however, it is nearly complete. This is because semi-classically, the angular momentum of the ejectile ^{3}He particle should scale with the momentum transfer q as $L = q \times b$. At intermediate beam energies ($\gtrsim$100 MeV/nucleon) and forward angles, q is small. Therefore, one expects the angular momentum transfer to also be small and that larger transfers diminish in importance at this beam energy [111].

The data is analyzed by examining the angular distribution of events in each 250 keV excitation energy bin of the spectrum in Figure 6.1 (a). Pairs of the distributions in Figure 6.2 are used to fit the angular distribution and determine the Gamow-Teller content, if any, based on the normalization of the J^π=1^+ curve resulting from the fit. The pair of curves minimizing the χ^2/N of the fit is generally taken as the best description

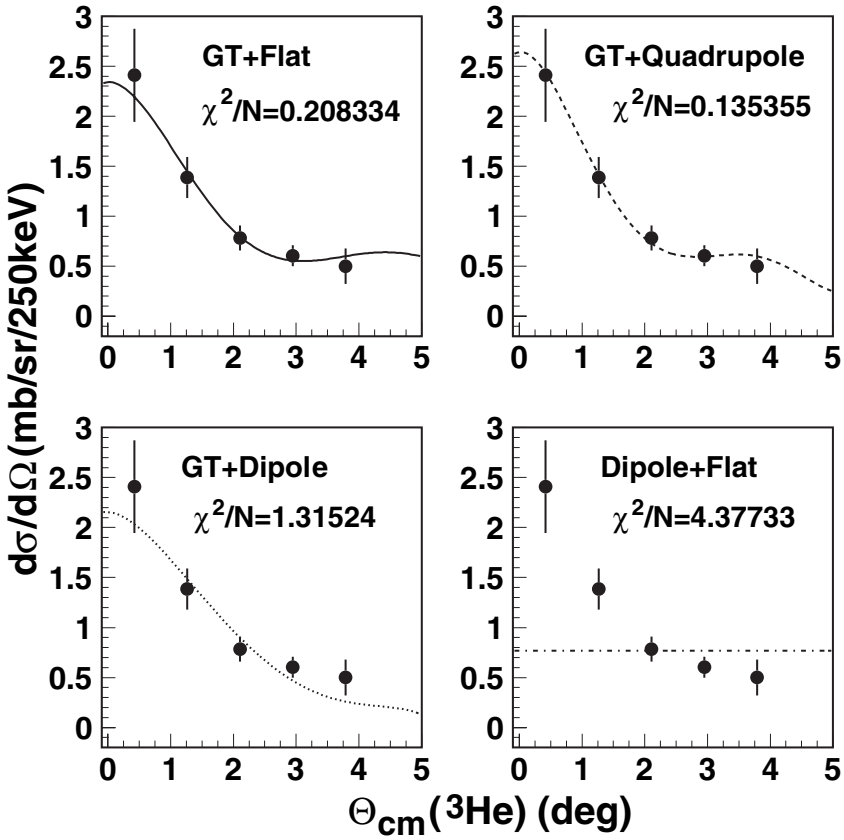

Figure 6.3: Four attempts to fit the angular distribution of events with 3.0 MeV $<$ $E_x(^{64}Cu) < 3.25$ MeV. (Top-left) Using a Gamow-Teller plus a flat angular distribution, (Top-right) a Gamow-Teller plus a quadrupole distribution, (Bottom-left) a Gamow-Teller plus a dipole distribution, (Bottom-right) and a dipole plus a flat distribution. The corresponding χ^2/N for each fit is displayed.

of the angular distributions.

Returning to consideration of the 3.1 MeV state, Figure 6.3 shows the angular distribution of events in the 250 keV-wide energy bin centered at 3.125 MeV. This state is forward-peaked in Figure 6.1 (b), making it a candidate GT state. However, it is not separated from neighboring states and does not have a pure Gamow-Teller angular distribution. Figure 6.3 displays the result of fitting the angular distribution with four pair-wise combinations of curves displayed in Figure 6.2. This fitting procedure is repeated for the angular distribution of each energy bin. The χ^2/N of the fit is displayed in each insert in Figure 6.3 and shows that GT + flat or GT + quadrupole shapes both describe the 3.1 MeV angular distribution data well.

Figure 6.4 shows again the result of fitting the 3.1 MeV state with a GT + quadrupole

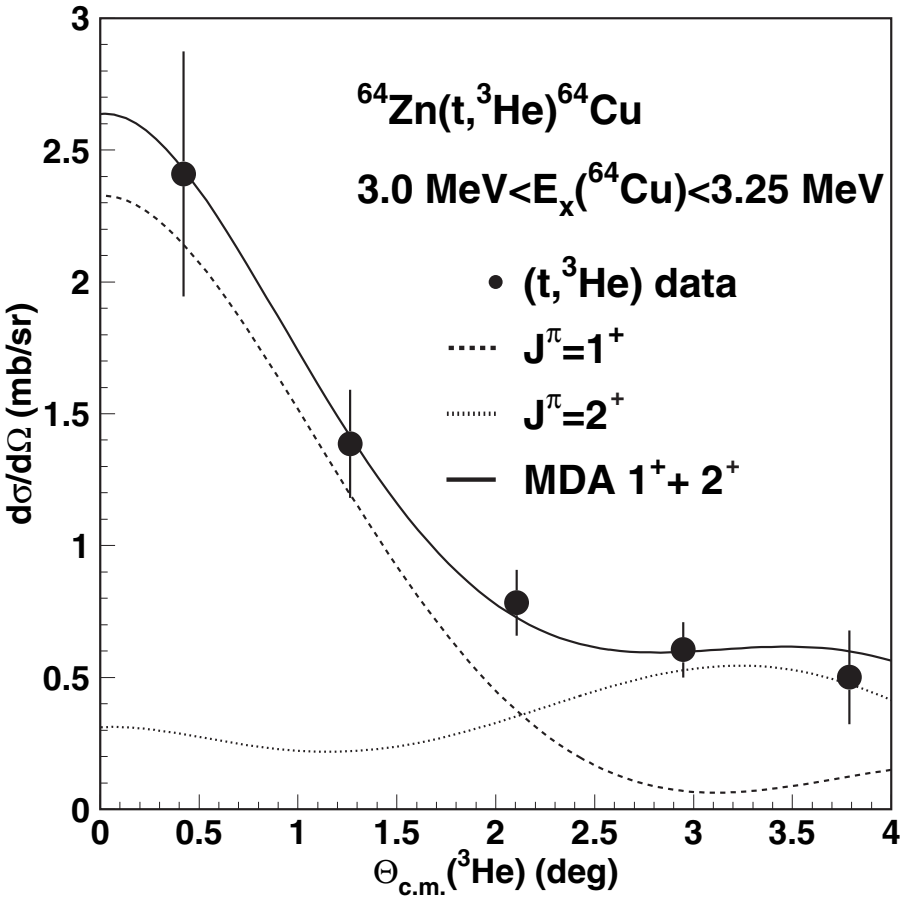

Figure 6.4: The fit for the angular distribution of events with 3.0 MeV $< E_X(^{64}Cu) <$ 3.25 MeV, using the Gamow-Teller plus quadrupole distribution, decomposed into the individual partial cross sections.

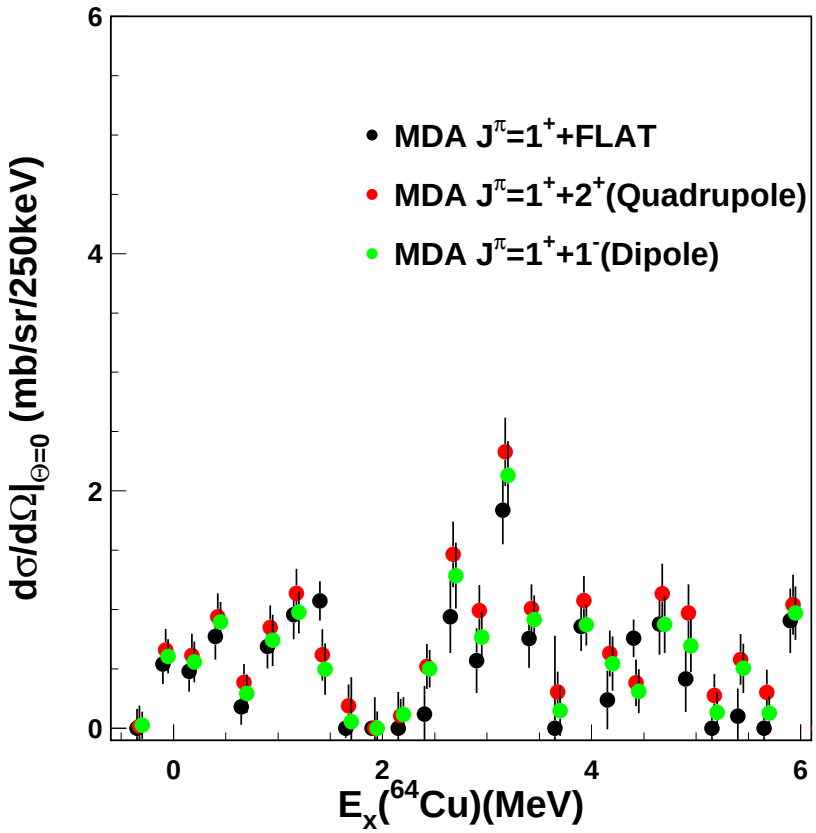

Figure 6.5: The 0° cross section of the Gamow-Teller (ΔL=0; J^π=1^+) component for each excitation energy bin in ^{64}Cu.

combination of angular distributions, only here the component distributions are shown explicitly. The 3.1 MeV state is well-described as having relatively strong $\Delta L = 0$ and weak $\Delta L = 2$ components, corresponding to to transitions to states in ^{64}Cu with J^π=1^+ and J^π=2^+ respectively. The $\Delta L = 0$ component of the fit is taken as the Gamow-Teller angular cross section for this energy bin. The Gamow-Teller cross section for each bin is determined in this way if the best description of the data from the fitting procedure includes a Gamow-Teller component. No Gamow-Teller cross section is assigned to a bin in the case where dipole + flat or other pairs of distributions offer a better description.

6.2 Extrapolation to Zero Momentum Transfer

The condition placed on the differential cross section in Equation 6.1, extrapolation to zero momentum transfer ($q \rightarrow 0$), is practically achieved in the data analysis by extrapolating measured GT cross sections to 0° scattering angle ($\Theta_{\mathrm{c.m.}}(^3\mathrm{He}) = 0^\circ$) and zero reaction Q-value (Q_{react}=0 MeV). The first is accomplished using the GT partial cross sections determined for each bin from the MDA. For example, for the 3.1 MeV state decomposed in Figure 6.4, the result is $d\sigma/d\Omega(\Theta = 0^\circ) = 2.3 \pm 0.3$ (mb/sr). Figure 6.5 shows the result of the extrapolation to $\Theta = 0^\circ$ for GT cross sections determined in each energy bin up to 6 MeV of excitation. The error displayed is that resulting from the fit.

Each set of 0° GT cross sections shown in Figure 6.5 is the result of pairing the GT component with another plausible angular distribution, as discussed previously. However, to within the error in the fit, all three models displayed show good agreement with one another. This is a result of statistical error, which is generally not sufficient to differentiate larger angular momentum transfers. Their close agreement does shows that determination of the 0° GT cross section is quite robust, though χ^2/N ultimately settles which description is used. The MDA then is a reliable method to distinguish $\Delta L = 0$ from $\Delta L > 0$ distributions.

The extrapolation to zero momentum transfer is completed by extrapolating 0° GT cross sections to zero reaction Q-value,

$$\left.\frac{d\sigma}{d\Omega}\right|_{q\rightarrow 0} = \left[\frac{\frac{d\sigma}{d\Omega}(Q=0,0^\circ)}{\frac{d\sigma}{d\Omega}(Q,0^\circ)}\right]_{DWBA} \times \left[\frac{d\sigma}{d\Omega}(Q,0^\circ)\right]_{exp}. \tag{6.2}$$

The 0° GT cross section determined from the data are scaled by a ratio, between 0° cross sections at a given reaction Q-value and Q=0. The ratio is calculated in the DWBA with the code FOLD [114], where tensor interactions are switched off to isolate the effect of larger momentum transfer. Figure 6.6 shows the value of this ratio for 100 theoretical states, predicted by the GXPF1a shell model effective interaction [107]. Note that choice of effective interaction does not change this ratio. GXPF1a is chosen only for the large number of states available from the calculation.

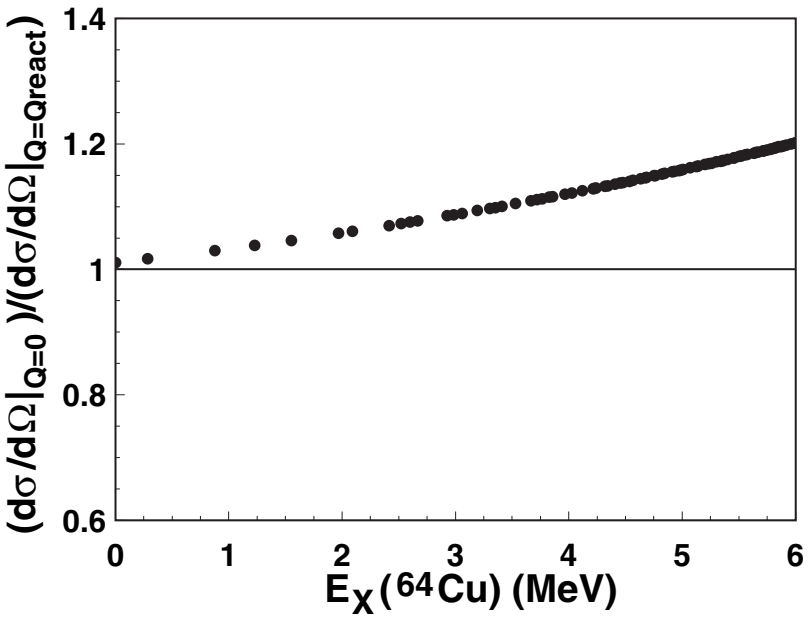

Figure 6.6: The ratio of the 0° cross section calculated with and without accounting for the reaction Q-value, using the DWBA code FOLD [114].

Figure 6.7 shows the 0° GT cross sections, taken from the value with the lowest χ^2/N for each energy bin in Figure 6.5, before (red) and after (blue) the extrapolation to zero momentum transfer. This is an important step toward the extraction of Gamow-Teller strength. It is true that for the most part, extrapolation to zero reaction value constitutes a small correction to the overall extrapolation to zero momentum transfer which is largely accomplished once the 0° GT cross section is determined. However, Figure 6.6 shows that the size of the ratio (deviation from unity) grows with increasing excitation energy. Also, since the correction comes as a scaling factor, the effect of extrapolating to zero reaction Q-value is larger for stronger states. For example, the correction to GT states at 3.1 and 6 MeV in Figure 6.7 are both ∼10%.

6.3 Application of the Unit Cross Section

The final step to determine the Gamow-Teller operator strength using Equation 6.1 is multiplication of the extrapolated cross sections by the unit cross section $\widehat{\sigma}_{\mathrm{GT}}$. Figure 6.8 shows the value of the unit cross section, plotted versus the target mass A, determined

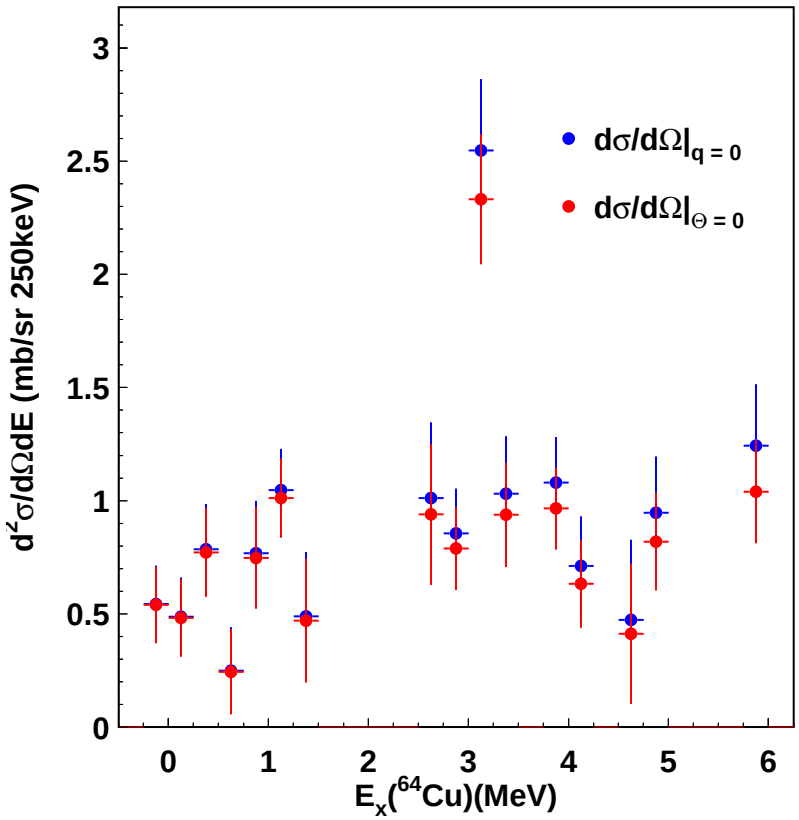

Figure 6.7: The doubly differential cross section that best describes the data on a bin-by-bin basis, (red) extrapolated to 0° scattering angle and then (blue) to zero momentum transfer.

from (^{3}He,t) cross section measurements on a wide range of target masses [110]. Zegers *et al.* find a simple relationship between target mass and the unit cross section,

$$\widehat{\sigma}_{\mathrm{GT}} = 109 \times A^{-0.65}. \tag{6.3}$$

In addition to this relationship, the authors of [110] (including this author) have recently found that for the cases so far analyzed, the GT unit cross section for (t,^{3}He) is consistently the same. Therefore, the high statistics and strong systematics present in the data for the (^{3}He,t) unit cross section benefit the determination of B(GT$_+$) from (t,^{3}He), particularly in cases where the typical normalization of relative B(GT) with states of known strength from β-decay is not possible. The B(GT$_+$) in ^{64}Cu is just such a case, where only the weak ground state strength is known from β-decay ($\log(ft) = 5.301 \pm 0.006$ [142], implying B(GT$_+$)=0.058$\pm$0.001) and the proportionality breaking in Equation 6.1 is potentially large. Also, the ground state is not individually resolved.

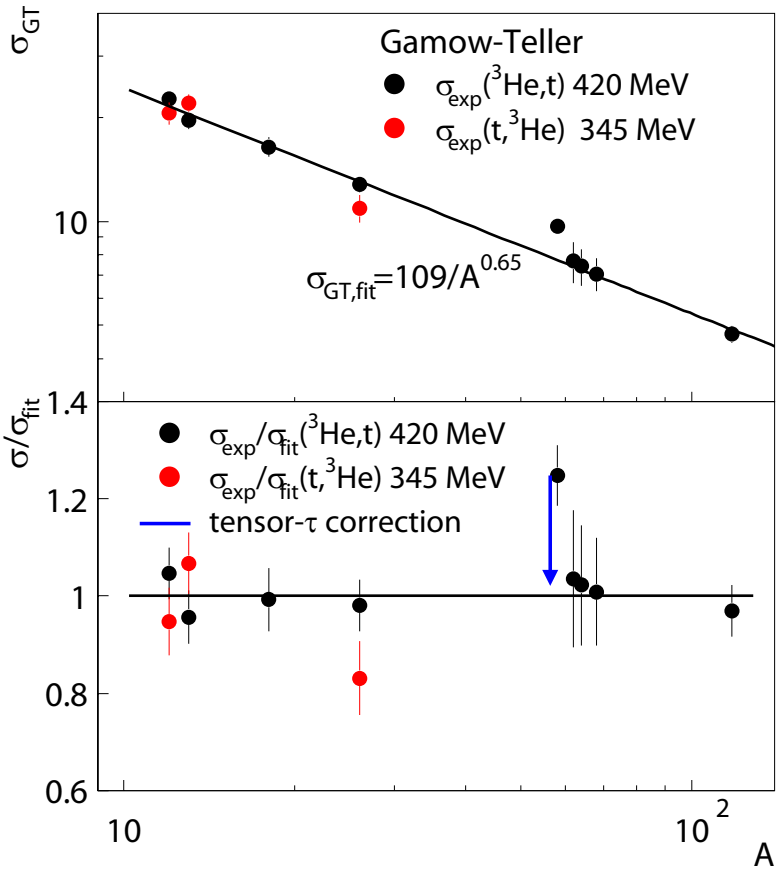

Figure 6.8: The Gamow-Teller unit cross section $\widehat{\sigma}_{\rm GT}$, determined for the (^{3}He,t) reaction at 140 MeV/nucleon, as a function of target mass A [110].

E_x (MeV)	B(GT$_+$)
0.000	0.059±0.02
0.125	0.08±0.02
0.375	0.11±0.03
0.625	0.03±0.03
0.875	0.11±0.03
1.125	0.14±0.02
1.375	0.07±0.04
2.625	0.14±0.05
2.875	0.12±0.03
3.125	0.35±0.04
3.375	0.14±0.03
3.875	0.15±0.03
4.125	0.10±0.03
4.625	0.06±0.05
4.875	0.13±0.03
5.875	0.17±0.04
$\sum$B(GT$_+$)	1.95±0.13

Table 6.1: Tabulated results for the extraction of B(GT$_+$) in ^{64}Cu, as a function of excitation energy E_x (MeV).

Figure 6.9 shows the extracted B(GT$_+$) in ^{64}Cu, determined by multiplying the extrapolated cross sections of Figure 6.7 by the unit cross section for $A = 64$ in Equation 6.3. These values are also tabulated in Table 6.1. The ground state is not individually resolved in this measurement, partly due to its weak B(GT) and partly due to the presence of other known 1^+ states nearby at 0.344, 0.66, and 0.927 MeV. Therefore, the B(GT) of the ground state bin is modified manually to agree with the β-decay result [142]. Originally, the ground state strength was spread over two bins, centered at -0.125 MeV and 0.125 MeV respectively, mixed with strength from the first 1^+ excited state at 0.344 MeV. These two strengths are 0.074 ± 0.023 and 0.067 ± 0.024 respectively. The strength of the first bin is reduced to 0.058 to correspond to β-decay and the excess strength of 0.016 is added to the next higher bin. Also, the center of the first bin is shifted to $E_x = 0$, since strength below this is unphysical and only due to the 280 keV experimental resolution. Both modifications are smaller than quoted errors and are done to aid calculation of electron-capture rates later in the text.

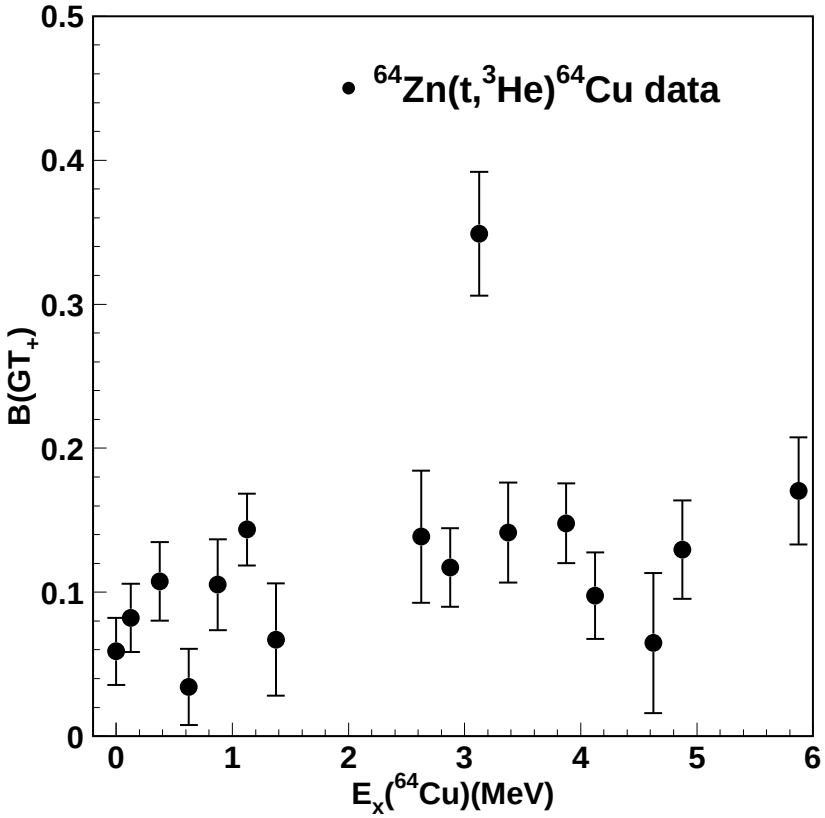

Figure 6.9: The GT_+ strength ($B(GT_+)$) in ^{64}Cu, plotted as a function of excitation energy in ^{64}Cu.

6.4 Analysis of Systematic Errors

The tensor contribution to the interaction between the target and probe systems is known [32,111] to be the main source of proportionality breaking between B(GT) and differential cross section at vanishing momentum transfer (Equation 6.1). The tensor interaction couples $\Delta L = 0$ with $\Delta L = 2$ modes and though the $\Delta L = 2$ amplitude by itself is usually very small by comparison, the amplitudes interfere. Therefore, the effect on the total GT cross section can be large. The interference effect can be constructive or destructive and has been shown to generally be stronger for states with smaller B(GT) [111]. However, large effects have also been observed in stronger states, in a few cases, depending on particular features of the initial and final state wave functions, like that of ^{58}Cu seen in the ^{58}Ni(^{3}He,t) reaction [112]. In their analysis, Cole *et al.* show that inconsistencies between B(GT) extracted from ^{58}Ni(^{3}He,t) and ^{58}Ni(p,n) arise from strong tensor effects, and break the proportionality with cross section in the two lowest lying GT states by $\sim$20%.

The proportionality breaking due to these tensor forces can be studied theoretically as the tensor component of the effective interaction $V_{\mathrm{T}\tau}$ can be turned off in the FOLD code. Alternatively, one can remove the tensor contribution to the $\Delta L = 2$ mode manually by removing $\Delta L = 2$ contributions to the one-body transition densities. However, the latter method yields the same result as the first and is more time-consuming. The present procedure for investigating the systematic error in the B(GT) extraction due to the tensor uses the first method, following the procedure shown in Ref. [111]. There, the relative systematic error is defined as

$$\text{Rel.sys.err.} = \frac{B(\mathrm{GT})_{\mathrm{DWBA}} - B(\mathrm{GT})_{\mathrm{SM}}}{B(\mathrm{GT})_{\mathrm{SM}}}, \tag{6.4}$$

where $B(\mathrm{GT})_{\mathrm{DWBA}}$ is determined by first calculating the differential cross section in DWBA with the full effective interaction, including the tensor forces. Thereafter, the DWBA cross section is treated like data, extrapolating to $q \rightarrow 0$ and dividing by $\widehat{\sigma}_{\mathrm{GT}}$ to determine B(GT). The shell model strength $B(\mathrm{GT})_{\mathrm{SM}}$ is calculated using the

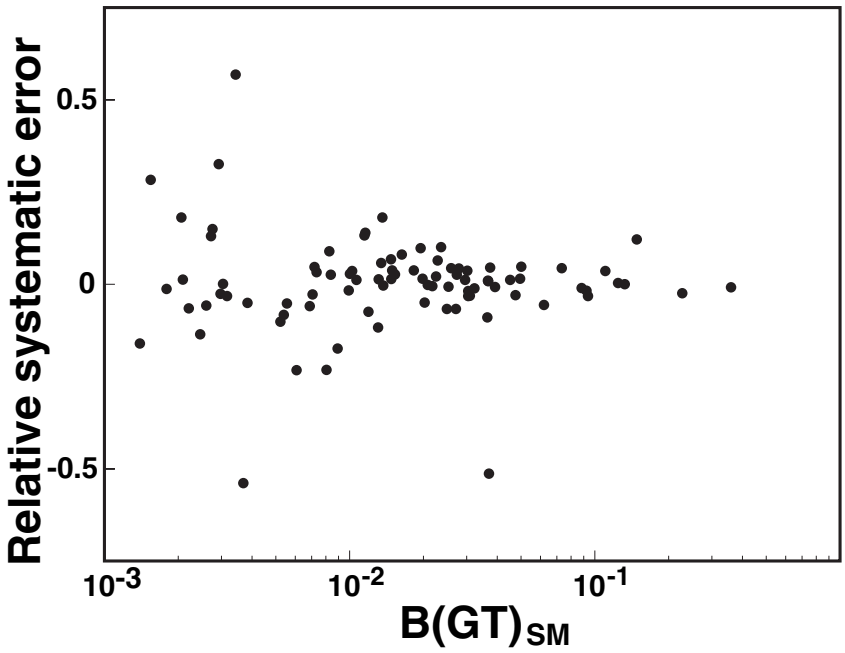

Figure 6.10: The relative systematic error in the extraction of B(GT), plotted as a function of the shell model strength.

GXPF1a effective interaction [53]. The one-body transition densities of this SM calculation also served as the input for the DWBA calculation used to estimate $B(GT)_{\mathrm{DWBA}}$. The $B(GT)_{\mathrm{SM}}$ should match $B(GT)_{\mathrm{DWBA}}$ if there were no systematic errors present. Relative systematic error is calculated on a state-by-state basis using Equation 6.4. The results are shown in Figure 6.10 for 100 states calculated using the GXPF1a effective interaction. The results using other interactions, such as KB3G [52], are qualitatively similar. Again, the GXPF1a interaction is used since more states over a larger excitation energy range are available from the calculation.

The magnitude of the proportionality breaking is clearly seen in Figure 6.10, reflected in the vertical width of the envelope formed by the points and becoming larger for weaker B(GT). Figure 6.11 shows three vertical sections of Figure 6.10, allowing a quantitative gauge of the error. An approximate relationship between B(GT) and relative systematic error can be determined with the standard deviation of these projections,

$$\sigma_{\mathrm{rel.sys.err.}} \approx 0.03 - 0.033 \times \ln(B(GT_+)). \tag{6.5}$$

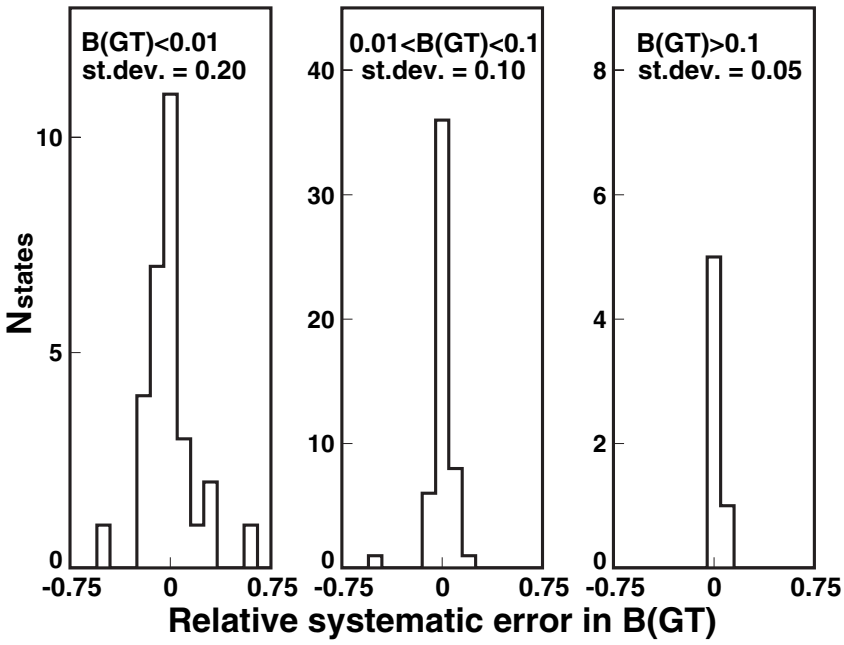

Figure 6.11: Vertical sections of Figure 6.10, projected onto the y-axis, showing the spread in the values for the relative systematic error of the B(GT) extraction.

This relationship is consistent with that seen in the case of ^{26}Mg [111].

Figures 6.12 and 6.13 show the results of the same procedure to determine the relative systematic, now carried out with the tensor interaction turned off for calculating the DWBA strengths. The envelope seen in Figure 6.10, much wider at low strength, is largely collapsed, showing that the tensor force is the dominant contribution to the proportionality breaking. The remaining widths seen in Figure 6.13 show there are still other contributions to the systematic error in the B(GT) extraction. These are mostly caused by exchange contributions to the cross section (see Chapter 3)

This error analysis also highlights the utility of using the GT unit cross section determined from (^{3}He,t) measurements [110]. Recall that the ^{64}Cu ground state strength is the only one known from β-decay, with a B(GT$_+$) of 0.058$\pm$0.001 [142]. For this state, Equation 6.5 anticipates a $\sim$12% likely systematic error in the B(GT) determined from its measured cross section. However, Figure 6.10 shows that states with strengths in this vicinity can still exhibit strong tensor effects, like the outlier at approximately B(GT) = 0.03 with a relative systematic error of 50%. If the ground state cross section in ^{64}Cu were to exhibit similar, unusually strong tensor effects like this outlier, then normalization to

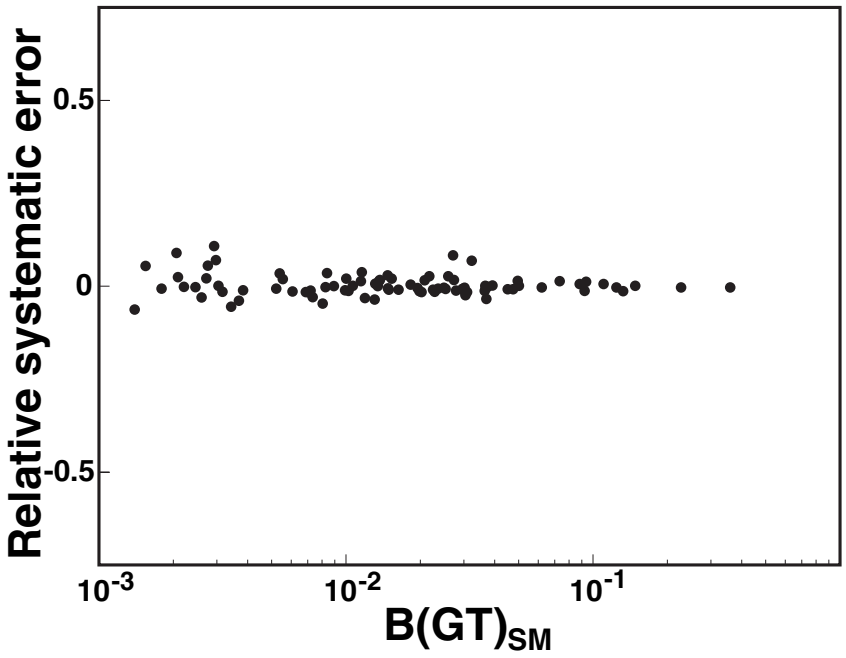

Figure 6.12: The relative systematic error in the extraction of B(GT), plotted as a function of strength, neglecting the tensor interaction between the target-probe systems.

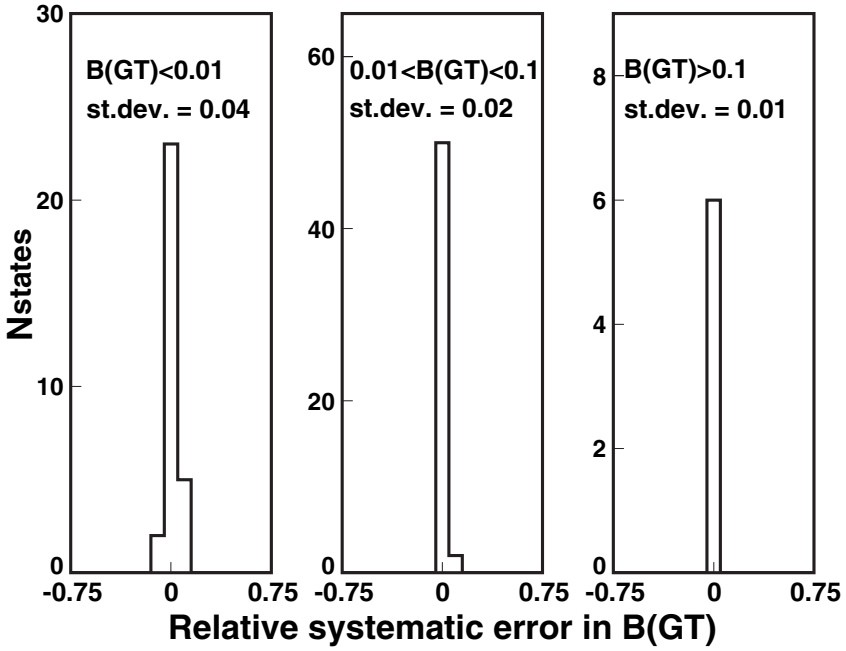

Figure 6.13: Vertical sections of Figure 6.12, projected onto the y-axis, showing the spread in the values for the relative systematic error of the B(GT) extraction.

the known B(GT) from β-decay for the ground state would introduce a 50% systematic error for all states in the spectrum. This outlier is not the ground state, which has a 6.7% uncertainty, in this particular case. Rather, it is the first excited state, predicted by the shell model to be at 0.284 MeV. This scenario however, does take place in the ^{58}Ni(p,n)^{58}Cu case, as revealed in the analysis of discrepancies between ^{58}Ni(^{3}He,t) and ^{58}Ni(p,n) reactions [112]. Therefore, there is strong incentive to rely on the unit cross section determined from (^{3}He,t) to scale B(GT) from (t,^{3}He) cross section data when normalization using β-decay would otherwise force reliance on weak states.

Chapter 7

Discussion

This chapter's purpose is three-fold. First, the recent determination of Gamow-Teller-plus strength in ^{64}Cu using the ^{64}Zn(d,^{2}He) reaction [143] is compared with the present result. Second, theoretical B(GT$_+$) distributions in ^{64}Cu, as determined using shell model effective interactions GXPF1a [107] and KB3G [52], are compared to the present result. Third, the stellar electron-capture rates, corresponding to strength determinations from (t,^{3}He) reaction data, are compared to rates determined using GXPF1a and KB3G shell model interactions.

7.1 Comparison with the (d,^{2}He) Reaction

The GT$_+$ strength has been extracted previously from differential cross sections measured in ^{64}Cu with the (d,^{2}He) reaction at 91.5 MeV/nucleon [143]. The ^{64}Zn nucleus is a candidate for neutrino-less double β-decay which, if such a process exists, would establish it as a Majorana particle and place constraints on the mass hierarchy among neutrino leptonic flavors [144]. Grewe *et al.* [143] examine both the B(GT$_-$) and B(GT$_+$) in ^{64}Cu using the ^{64}Zn(d,^{2}He) and ^{64}Ni(^{3}He,t) [145] reactions, respectively, in order to constrain the neutrino-less double β-decay matrix elements. Though their motivation for measurement differs, the experimental result of Grewe *et al.* is directly comparable to the result in this thesis.

Figure 7.1 shows the distribution of B(GT_+) in ^{64}Cu as determined using (t,^{3}He) (black) and (d,^{2}He) (red) reactions [143]. Grewe *et al.* achieved an excitation energy resolution of 115 keV (FWHM) for doubly differential cross sections measured in ^{64}Cu. Therefore, they were able to individually resolve several low-lying $J^\pi = 1^+$ states and where possible, performed the B(GT_+) extraction on a state-by-state, rather than a bin-by-bin basis. Despite this difference, Figure 7.1 still shows qualitatively, a good overall correspondence between features of the B(GT_+) spectra. Grewe *et al.* resolve the weak ground state transition which, recalling from Chapter 6, is of known strength from β-decay. Therefore, they use this strength to determine the overall unit cross section and subsequently the B(GT) for the rest of the spectrum. Consequently, the agreement between the B(GT_+) for the lowest bin from the (t,^{3}He) data and the B(GT_+) for the ground state from the (d,^{2}He) data is exact, since the (t,^{3}He) for the lowest bin was manually pegged to the β-decay value. The reason this is done is so that the electron-capture calculation, presented below, will be as realistic as possible. The manual adjustment is also justified since the β-decay strength for the ground state and that which comes directly from the MDA agree within statistical errors. There is only one other minor discrepancy, due only to the use of sources for the ground state strength; Grewe *et al.* takes for the ground state a value from 1996: $\log ft = 5.294 \pm 0.005$ [146], while for the present work, a value from 2007 is taken: $\log ft = 5.301 \pm 0.006$ [142].

Grewe *et al.* encounters similar difficulty resolving states in the excitation interval from 200 to 600 keV. They assign B(GT_+)=0.182 ± 0.034 for this interval, resulting from an MDA method similar to the one presented in Chapter 6. The differences arise from DWBA calculations involving the (d,^{2}He) probe which is more difficult to treat theoretically since the ^{2}He system is unbound. The location of strength in the first 1 MeV of excitation therefore is not identical with the (t,^{3}He) result. Following a bin-by-bin approach, the (t,^{3}He) result for the total strength in this interval is similar, but it is found spread over several energy bins. This is reasonable since the energy resolution is 280 keV (FWHM) and the bins are 250 keV wide. Nevertheless, Figure 7.2 shows that the total strength is consistent. There, the running sum of B(GT_+) is plotted against excitation

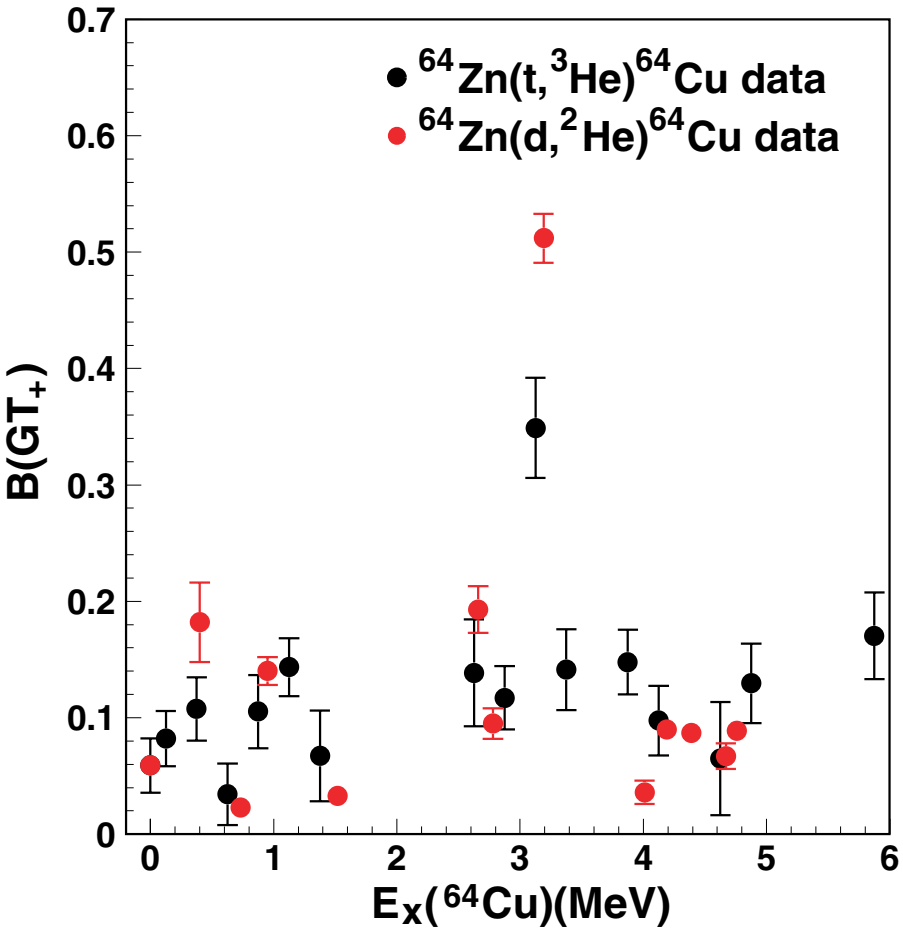

Figure 7.1: Comparison of B(GT$_+$) distributions in ^{64}Cu as determined from (t,^{3}He) (black) and (d,^{2}He) (red) reactions [143].

in ^{64}Cu, with the vertical width of bands representing the cumulative error in the sum. Examining the running sum, the correspondence between the these two data is clearer. The relative lack of B(GT$_+$) seen from ≈1500 to 2500 keV of excitation is consistent. Also, both measurements agree on the location and strength of the two strongest Gamow-Teller states in the spectrum, those at ≈2.6 and ≈3.2 MeV, to within experimental resolutions and errors in the strength. This is not as clear in a direct comparison of the spectra in Figure 7.1, e.g., the strength of the state at ≈3.2 MeV, as the resolution for the (t,^{3}He) result spreads the strength of this state in adjacent energy bins.

The most significant point to make, when comparing the (t,^{3}He) and (d,^{2}He) results, is that the overall normalization of the strength has been accomplished in different ways. For the (d,^{2}He) measurement, as mentioned above, the weak ground state transition is resolved and is of known strength, so Grewe *et al.* use this to normalize their ^{64}Cu B(GT) spectrum. In the present case with the (t,^{3}He) measurement, the consistency of the (t,^{3}He) and (^{3}He,t) unit cross sections has been used. The agreement seen in Figure 7.2 between the (t,^{3}He) and (d,^{2}He) results is further evidence that using the (^{3}He,t) unit cross section for normalizing (t,^{3}He) cross section to B(GT) is a reasonable procedure. The total strengths are in reasonable agreement, up to 5 MeV excitation, the energy up to which Grewe *et al.* extract B(GT). From the (t,^{3}He) result, $\sum \mathrm{B(GT_+)} = 1.78 \pm 0.13$ and from (d,^{2}He), the result for the total strength is $\sum \mathrm{B(GT_+)} = 1.61 \pm 0.05$. As stated earlier in Chapter 6, the consistency of the (t,^{3}He) and (^{3}He,t) unit cross sections adds an advantage to using the (t,^{3}He) reaction because it reduces the likelihood that a state where proportionality breaking effects are strong is used to determine the overall normalization. As discussed in Chapter 6 this is a risk in the ^{64}Cu case, where the only state of known strength is weak (B(GT$_+$)≈0.03) and the corresponding breaking is potentially on the level of 50%.

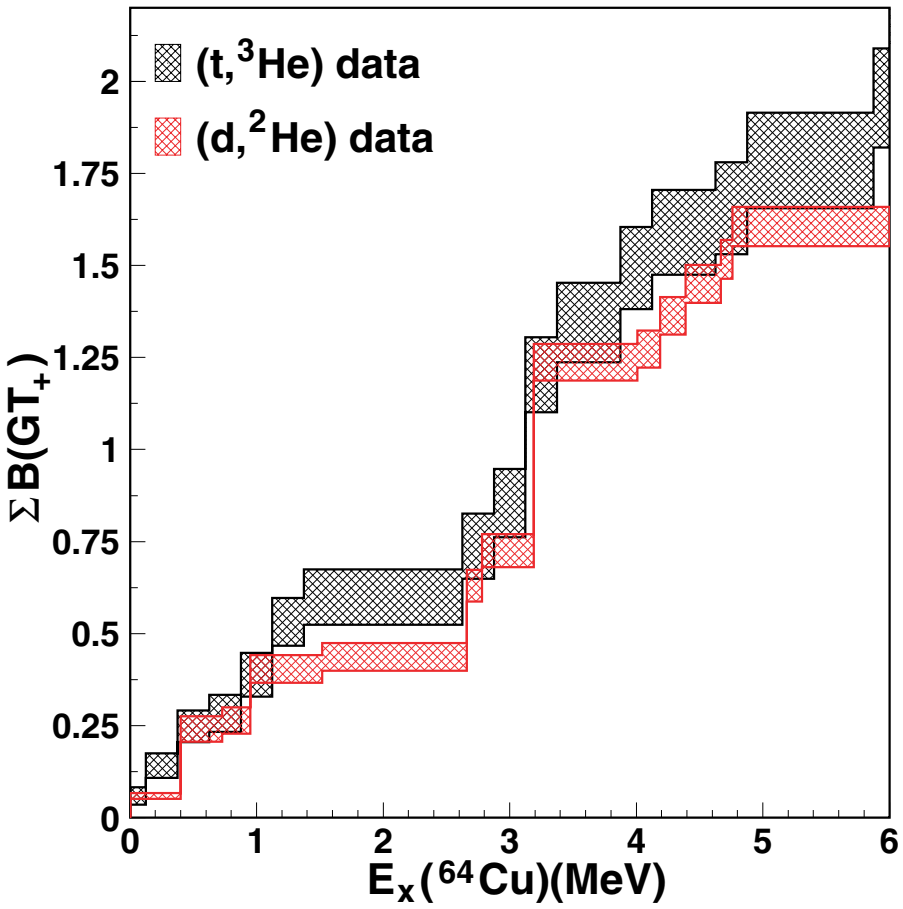

Figure 7.2: Comparison of the running sum of $B(GT_+)$ in ^{64}Cu as determined from (t,^{3}He) (black) and (d,^{2}He) (red) reactions [143]. The vertical width of each curve represents the cumulative error in the sum.

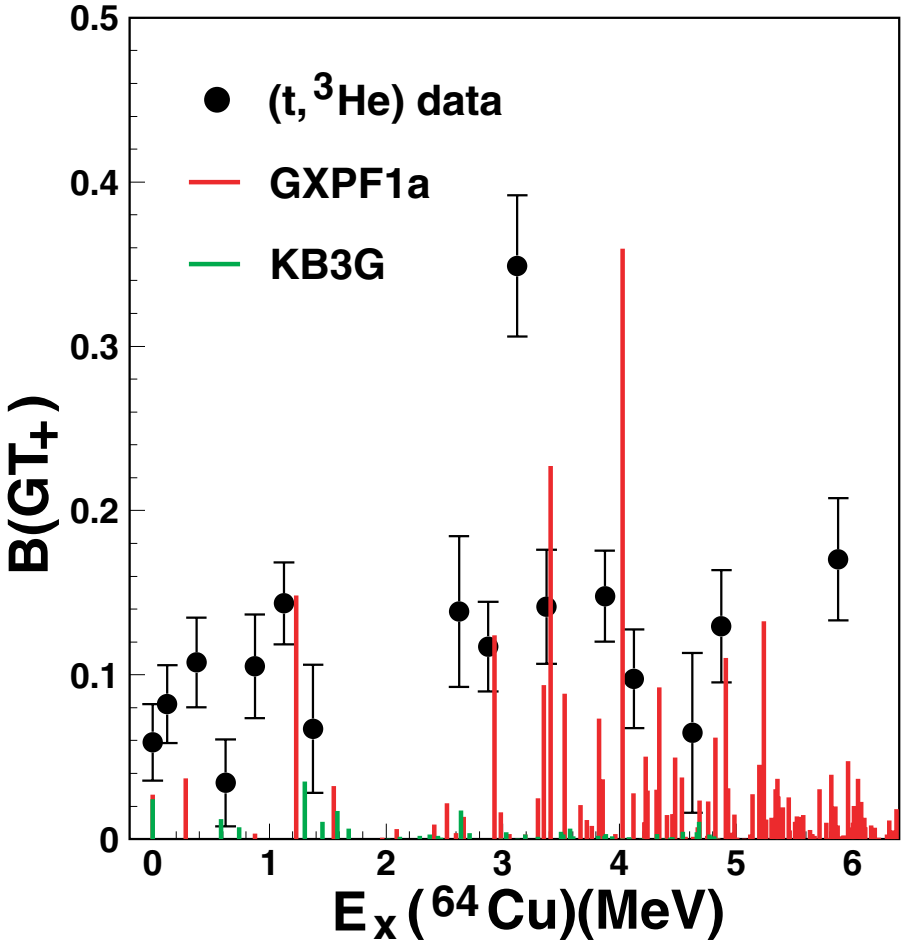

Figure 7.3: The B(GT_+) in ^{64}Cu as predicted by shell model effective interactions GXPF1a [107] (red) and KB3G [52] (green) in comparison to the (t,^{3}He) result. The shell model calculation is performed using NuShellX [51].

7.2 Comparsion to Shell-Model Calculation

A crucial comparison to make is between data and theoretical estimates, since one major motivation for this work is the parameterization of stellar electron capture. As discussed in Chapter 2, rates must ultimately rely on theory to provide the majority of Gamow-Teller transitions, since most are unmeasurable. If a theoretical approach can however, robustly reproduce measurable transitions from parent ground states over a wide mass range, there is increased confidence that the same approach will work for transitions in general. Figure 7.3 compares the presently measured B(GT$_+$) spectrum in ^{64}Cu to that calculated with the shell-model code NuShellX [51] using effective pf-shell interactions GXPF1a [107] and KB3G [52]. The calculation using the KB3G interaction is carried out for the first 50 states predicted in the pf-shell model space. The GXPF1a calculation is carried out for 100 states. The KB3G interaction is chosen since it is the interaction used to calculate the LMP rates [46], used in many stellar evolution codes. The GXPF1a interaction is chosen since it has been fitted to the largest number of data sets over the entire pf-shell [107]. To compare with measured spectra, the universal quenching factor discussed in Chapter 3 of $(0.74)^2$ is applied to KB3G and GXPF1a GT strengths.

The most prominent feature of the comparison is the lack of strength predicted by KB3G which was constructed specifically to calculate B(GT) values in pf-shell nuclei. This discrepancy is expected however, since the KB3G interaction is determined using only spectroscopic data from the lower pf-shell, up to $A = 52$ [52]. Comparatively improved performance by GXPF1a in the upper pf-shell is anticipated, as the interaction is determined by fitting ∼700 energy data across $47 \leq A \leq 66$ [53, 107, 147]. In the particular case of GXPF1a then, comparison to B(GT) values is informative, as the interaction there is most finely-tuned for calculation of low-lying rotational level systematics and corresponding B(Eλ) values. Comparison to B(GT) then offers an independent check on the GXPF1a description of the pf-shell.

The running sum for these three B(GT$_+$) spectra are presented in Figure 7.4. Up to 6 MeV, for the (t,^{3}He) result this is $\sum$B(GT$_+$) = 1.95 ± 0.13, for GXPF1a it is

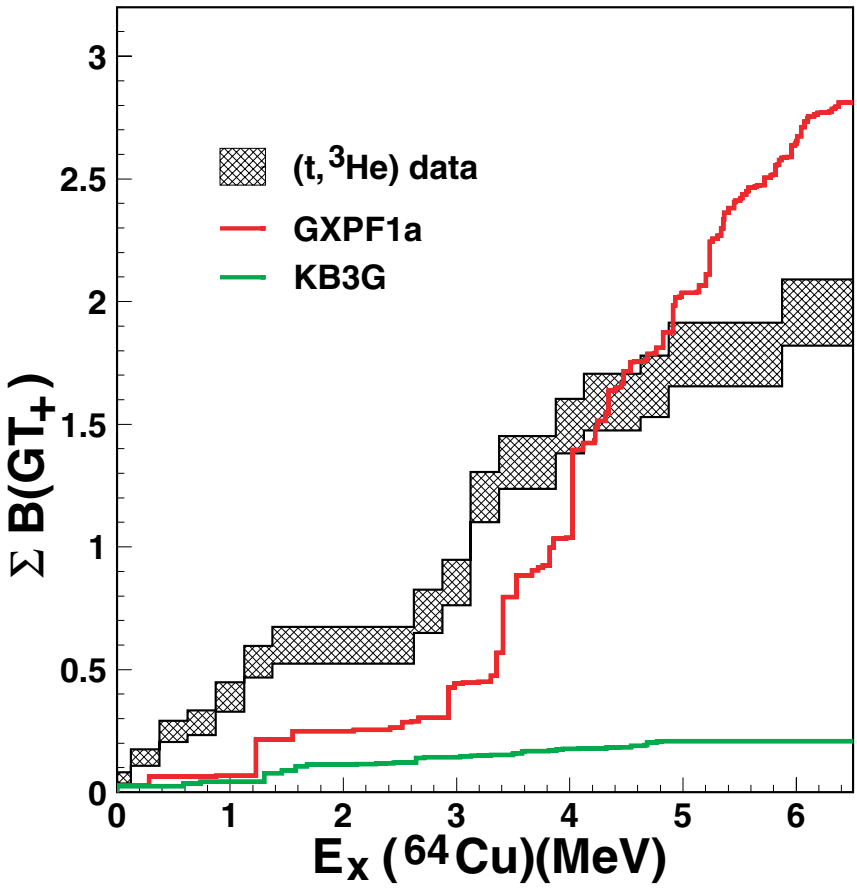

Figure 7.4: Comparison of the running sum of $B(GT_+)$ in ^{64}Cu as determined from (t,^{3}He) data (black) and by shell model effective interactions GXPF1a [107] (red) and KB3G [52] (green). The vertical width of the data curve represents the cumulative error in the sum. No error is assigned to the theoretical results.

$\sum$B(GT$_+$) = 2.81 and for KB3G up to 5 MeV the sum is $\sum$B(GT$_+$) = 0.21. The KB3G calculation was not carried up to 6 MeV excitation because the result up to 5 MeV is identical with a 6 MeV calculation already performed by Grewe *et al.* [143]. They find one additional GT state above 5 MeV that brings their KB3G calculation of the total strength to $\sum$B(GT$_+$) = 0.69. Again, half or more of the strength below 3 MeV is not reproduced by shell-model calculations. From a viewpoint of nuclear structure studies, however, the GXPF1a performance is quite reasonable. Overall, it approximately reproduces the location, strength and scatter of the Gamow-Teller giant states and, with the m-scheme based method used in NuShellX [51], reproduces the fragmentation of the GT strength over many final states. However, the corresponding electron capture rates show a particular sensitivity to the low-lying distribution of B(GT$_+$).

Figure 7.5 shows the side-by-side comparison of B(GT$_+$) spectra (left) presented in Figure 7.4 and their corresponding electron capture rates (right) at an electron-density of $\rho Y_e = 10^7$ g/cm^3. This density corresponds to times early in the pre-core-collapse phase of a 14 M$_{\rm solar}$ star. The electron capture rate is calculated from the B(GT$_+$) using the method of Fuller, Fowler, and Newman [26] described in Chapter 2. In the relevant temperature region, marked by the yellow band, the measured B(GT$_+$) results in an electron capture rate of $\log(\mathrm{EC}_{\rm rate}(\mathrm{s}^{-1})) = -3.06$ (or 8.71×10^{-4} captures/second). At the same temperature, the GXPF1a rate predicted is a factor 3.5 smaller and KB3G a factor 5.0 smaller.

It is not immediately obvious from their B(GT$_+$) spectra and running sums, seen in Figures 7.3 and 7.4 why it is that the electron capture rates determined from data, GXPF1a, and KB3G differ as they do. For instance, why do the spectra and summed strength for GXPF1a and KB3G interactions differ so much and yet, their electron capture rates seems so similar? Their total strengths up to 5 MeV excitation differ by nearly a factor of 10 but their electron capture rate by only 44%. Or, since the GXPF1a sum of the GT-strength overtakes that of the data (at $\sim$5 MeV), why is it that the GXPF1a electron capture rate doesn't overtake that of the data?

The answer to these questions has three ingredients. The electron capture rate is

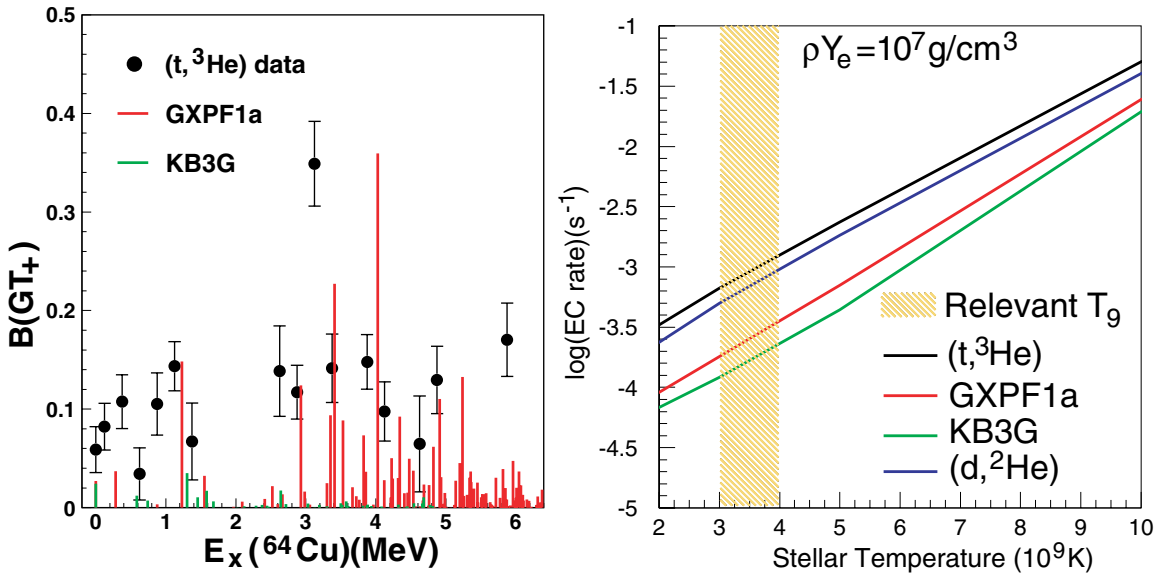

Figure 7.5: Side-by-side comparison of $(t,^3\mathrm{He})$ and shell model results for $\mathrm{B(GT_+)}$ in ^{64}Cu with their corresponding stellar electron-capture rates, calculated at $\rho Y_e = 10^7 \mathrm{g/cm^3}$.

roughly proportional to the B(GT) and the energy-integrated product of a phase space term and the occupation function of available electrons (see details in Chapter 2). The contribution from a given GT-state to the overall electron capture rate is roughly parameterized by the product $B(GT_+) \times \int (\text{Phase Space} \times \text{Electron Occupation})$. The well-known "Sargent's Rule", that β-decay rates are proportional to reaction Q-value taken to the power 5, is due to the phase space term. Therefore, this term is large at the daughter ground state and falls toward zero rapidly for increasing excitation energy. The occupation function for electrons is understood in the usual way, being unity (degeneracy) below the Fermi energy ϵ_F and zero above, though the Fermi surface is smeared at finite temperature.

With these three ingredients in mind, consider again the capture rates presented in Figure 7.5. The electron confinement at this density ($\rho Y_e = 10^7$ g/cm^3) raises the electron Fermi energy to $\epsilon_\mathrm{F} \approx 0.7$ MeV. Above this energy, neglecting finite temperature, the capture reaction is not energetically possible since there are no electrons with kinetic energy sufficient reach the reaction Q-value. Consequently, the electron occupation term acts as a low-pass filter on the $\mathrm{B(GT_+)}$ spectrum. The capture rate is determined by the B(GT) in states below ϵ_F and is unaffected by the strength of states above ϵ_F. The simi-

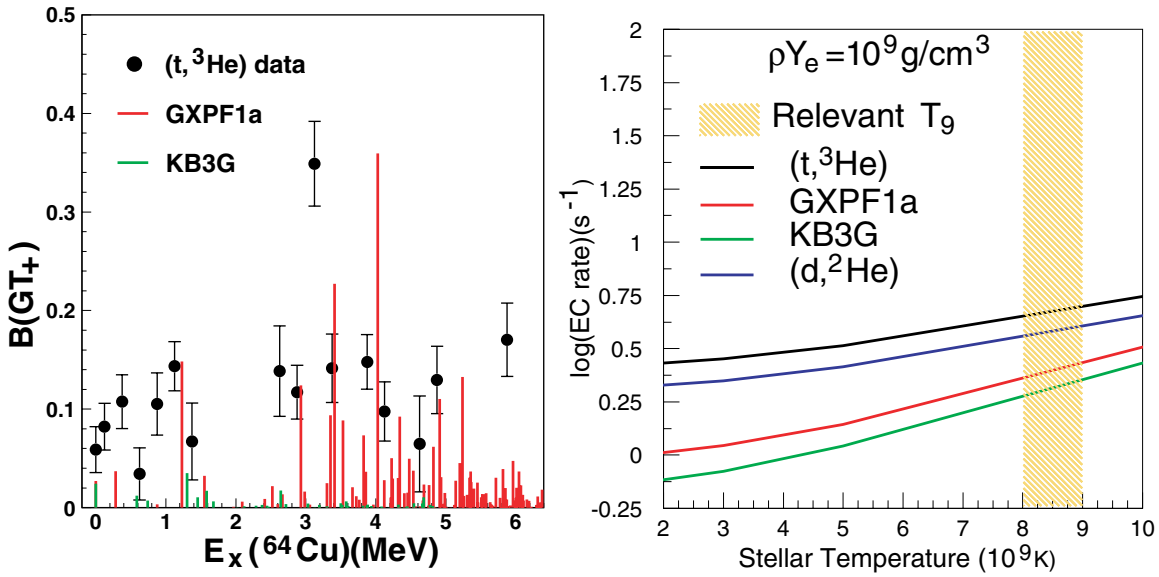

Figure 7.6: Side-by-side comparison of $(t,^3\mathrm{He})$ and shell model results for $\mathrm{B(GT_+)}$ in ^{64}Cu with their corresponding stellar electron-capture rates, calculated at $\rho Y_e = 10^9\mathrm{g/cm}^3$.

larity of both shell-model rates at this density then becomes clear when one reexamines the sum of $\mathrm{B(GT_+)}$ at ≈0.7 MeV in Figure 7.4. There, the total strength predicted by GXPF1a and KB3G are nearly identical and less than half that seen in the $(t,^3\mathrm{He})$ data. The capture rate determined from data then is larger and differences in the $\mathrm{B(GT_+)}$ above ≈0.7 MeV have little impact on the overall rate.

Figure 7.6 shows the electron capture rate along with the $\mathrm{B(GT_+)}$ spectra from data and shell-model calculations, as in Figure 7.5, only now the stellar density is $\rho Y_e = 10^9\mathrm{g/cm}^3$. This corresponds to moments (outer-core in-fall velocity < 1000km/s [91]) just before the onset of collapse, again with the relevant temperature highlighted in yellow, in a 14 M_{solar} star. At this density, the Fermi surface is pushed up to $\epsilon_{\mathrm{F}} \approx 4.7$ MeV. Looking at the total GT-strengths in Figure 7.4 again, one sees that at this energy, KB3G has added little additional strength. However, the total strength predicted by GXPF1a has risen sharply and now agrees with the total strength from data. Yet, the respective electron capture rates remain similar, relative to one another. All rates are larger, but the data still predicts a capture rate about a factor of 3.5 larger than GXPF1a and a factor of 5 larger than KB3G. This is due to the rapid decline in the size of the phase space term as a function of excitation energy, mentioned above. Since it is integrated

with the electron occupation, it acts as a weighting function, reducing the importance of high-lying GT-states made accessible by raising the Fermi surface. The electron capture rate determined from the data remains larger because the low-lying B(GT), which is heavily weighted by the phase space term, is also larger.

Finite temperature has little effect in the particular case of ^{64}Cu since the strengths are small. As the temperature increases, the Fermi surface is smeared so that electrons can typically have energies $\sim k_{\mathrm{B}}T$ above ϵ_{F}. At this temperature, $T = 10 \times 10^9$ K, $k_{\mathrm{B}}T = 900$ keV so that states at and below $\approx$1600 keV are accessible for captures. In Figure 7.4, this is just above where GXPF1a and KB3G make gains in the total predicted strength, though it is insufficient to produce much change in the capture rate. In the case of ^{58}Co however, a relatively strong GT-state below 2 MeV makes this effect more pronounced [112]. In such a case, the weak smearing of the Fermi surface is overcome by a strong state at low-lying excitation, where the phase space term is large. The conclusion in both cases however is the same: the specific B(GT) distribution at low excitation in the electron capture daughter dominates the electron capture rate. Nevertheless, relatively small mistakes made in determining the low-lying strength can produce large systematic errors in capture rates that persist over a wide range of temperatures and densities.

To conclude, it is observed that the B(GT$_+$) in ^{64}Cu, as determined with the (t,^{3}He) and (d,^{2}He) [143] charge-exchange reactions, are consistent. Furthermore, the different procedures in the two measurements for the overall normalization of the strength is further evidence that B(GT) can be extracted from charge-exchange in a probe-independent way. Specifically, for the (t,^{3}He) case, the comparison with (d,^{2}He) also reveals the utility of using the consistent (^{3}He,t) unit cross section for the (t,^{3}He) normalization. This has the advantage of avoiding normalization with individual states on a case-by-case basis, which can potentially introduce systematic errors as large as 50%. The comparison of the B(GT$_+$) in ^{64}Cu measured with (t,^{3}He) is also compared to shell-model determinations using NuShellX and the pf-shell effective interactions KB3G and GXPF1a, revealing the excitation energies where improvements in performance are desirable. A potential source for the differences between the measured and calculated strength distributions may be

the interaction of the $g_{9/2}$ single-particle level with the pf-shell states. This is a reasonable possibility however, the model space associated with cross-shell excitations between pf- and sdg-shells is quite large, making corresponding shell-model calculations of that kind very difficult. In the remaining chapter, the overall conclusions of this work will be summarized and recommendations made for technical improvements, new (t,^{3}He) and other charge-exchange measurements to be made, which will advance the state of this important sector in supernova physics.

Chapter 8

Conclusion and Outlook

The production and transmission of a secondary triton beam by fast-fragmentation of ^{16}O and ^{18}O beams has been studied. The triton beam produced at the NSCL-CCF with the ^{16}O primary beam is found to be superior to that of ^{18}O. This is primarily the result of the higher extraction energy possible for the ^{16}O primary beam. With the 150 MeV/nucleon ^{16}O primary beam and a $3 - 4 \times 10^3$ mg/cm^2 $^{\text{nat}}$Be target, triton rates in excess of $8 - 10 \times 10^4$/pnAs of primary beam are achieved. Using this triton beam, a (t,^{3}He) charge-exchange reaction program has been re-instituted at NSCL-CCF, successfully extracting B(GT$_+$) in ^{24}Na via the ^{24}Mg(t,^{3}He) reaction [7].

The B(GT$_+$) distribution in ^{64}Cu has been measured, up to 6 MeV in excitation energy. The ^{64}Cu system is in the pf-shell region of the nuclear landscape. Shell-model calculations of the ^{64}Cu B(GT$_+$) have been made with the NuShellX code [51], using KB3G [52] and GXPF1a [107] pf-shell effective interactions. The sum of the measured strength below 6 MeV excitation is $\sum$B(GT$_+$) $= 1.95 \pm 0.13$. For the same excitation energy range, the calculation with GXPF1a gives $\sum$B(GT$_+$) $= 2.81$. The calculation using KB3G was done only up to 5 MeV, finding a total strength of $\sum$B(GT$_+$) $= 0.21$. This calculation was stopped at 5 MeV since, up to this energy, it is identical to the same calculation done by Grewe *et al.* [143]. Their calculation is carried out to 6 MeV excitation however, finding only one additional significant state and raising the sum to $\sum$B(GT$_+$) $= 0.69$. In the case of the $\sum$B(GT$_+$) calculated with GXPF1a, the NuShellX

code determines from the non-energy weighted GT sum $\sum \mathrm{B(GT_-)} - \sum \mathrm{B(GT_+)} = 3(N-Z)$, that at and below 6 MeV excitation, the calculated $\sum \mathrm{B(GT_+)}$ is exhausted to the 93% level. This agrees with data taken at higher excitation energies which indicates there are no strong GT states in the excitation energy interval $6 < E_{\mathrm{x}}(^{64}\mathrm{Cu}) \lesssim 25$ MeV.

Discrepancies between measured and calculated values for the total strength are likely due to admixtures of configurations outside of the pf-shell. Since $A = 64$ is high in the pf-shell, a likely culprit is the intrusion of the $g_{9/2}$ single-particle orbit from the sdg-shell above. This is a reasonable possibility because the, for region around $N = 34$, the Nilsson model picture of the single-particle energies shows the $g_{9/2}$ level coming down quickly for positive deformation β [146]. The measured ground state deformation for ^{64}Zn is $\beta = 0.24$ [148], so the intrusion of the $g_{9/2}$ level must be considered.

The ^{64}Cu system is in the pf-shell, the isotopes of which are important electron-capture participants in Type Ia and core-collapse supernovae. The electron-capture rate for ^{64}Cu has been calculated from both the measured $\mathrm{B(GT_+)}$ distribution and that of the two shell-model calculations, using KB3G and GXPF1A effective interactions. The difference between rates determined from the data and these shell-model calculations are of the same size as differences between the FFN and LMP rates for nuclei at masses $A \leq 60$. This is significant since recent supernova sensitivity studies show that the upper pf-shell makes important contributions to the overall capture rate and the KB3G interaction is the most advanced form the the interaction used to determine the LMP capture rates. These are the most widely used rates after those of FFN.

Additionally, while the gross features of the measured $\mathrm{B(GT_+)}$ distribution are better reproduced by the GXPF1A interaction, the capture rates for KB3G and GXPF1A are not significantly different under conditions relevant to a $15M_{\mathrm{solar}}$ core-collapse scenario. This is due to the capture rate's particular sensitivity to $\mathrm{B(GT_+)}$ located in the first couple MeV of excitation in the daughter. Since the supernova evolution is significantly changed by choosing either FFN or LMP rates, it should not be surprising if similar size changes still occur, as shell-model calculations are refined to converge on measured B(GT) distributions. Increasing the body of measured $\mathrm{B(GT_+)}$ distributions is crucial

for this development process. Pursuant to this, the (t,^{3}He) charge-exchange reaction will remain an important spectroscopic tool for extracting Gamow-Teller strength.

8.1 Detailed Conclusions

It is important to qualify the statements above and note that decades of modeling work have shown that for both Type Ia and core-collapse explosions, there is likely no single contribution to the microscopic physics that alone will determine how well the explosion is modeled. In both types, the interplay between gravitational, three-dimensional, hydrodynamical, radiation and neutrino transport and nuclear effects is complex and often chaotic. The intrinsic diversity seen even within the relatively uniform Type Ia category suggests that several different factors contribute to the overall success of an explosion. This is even more the case for core-collapse explosions. The accurate determination of Gamow-Teller strength and the accurate treatment of electron-capture will add necessary information for producing successful explosions in the core-collapse case and reproducing Type Ia spectra and iron-group nucleosynthesis yields.

Nevertheless, accurate determination of the electron-capture rates alone will not be sufficient for reaching these goals. In the situation the nuclear-astrophysics community finds itself in, particularly in the case of core-collapse theory, the uncertainties of all major contributions must be reduced or there will always be doubt as to whether or not explosions succeed for the wrong reasons. For example, there have been recent reports of robustly successful core-collapse explosions with the VULCAN/2D code, produced by the excitation of an acoustic, dipolar mode of the core material [149]. This however has lead to some controversy, suggesting that the new explosion mechanism may be the result of accumulated machine round-off errors [150]. For the purposes of this text its not important whether this is the case or not. This merely serves as an example of how fickle the core-collapse explosion mechanism appears to be. Therefore, it is important that relevant sub-fields within nuclear-astrophysics work together to identify and reduce their respective contribution to the overall uncertainties. This includes shell-model de-

terminations of electron-capture which have served as an excellent example of the kind of cooperation that is needed. Supernova modelers have determined the mass ranges of nuclei that are important, shell-model theory has risen to the challenge of calculating B(GT) in medium-heavy nuclei, and this feedback should continue. And again, charge-exchange reactions are the principle nuclear spectroscopy technique needed to guide the shell-model refinements and maximize the quality of B(GT) calculations. These in turn have a direct impact on the quality of electron-capture rate calculations, as has been shown.

One objective of this work has been to demonstrate the reinstitution of the (t,^{3}He) charge-exchange probe at the NSCL CCF to serve this purpose. Prior to the CCF upgrade, the triton beam was produced as a secondary beam by fragmentation of a primary α-particle beam. The secondary triton beam has been recovered by exploring its production from fragmentation of ^{16,18}O beams, the lightest beams now available at NSCL. In addition, the production of tritons for (t,^{3}He) reaction studies has been optimized by studying the effect of target configurations and secondary tuning characteristics. It was found that, due to the need to operate the S800 spectrograph in a dispersion-matched mode, the quality of the triton beam for this purpose is optically sensitive. Consequently, care needs to be taken to establish the location of the optical object location for both A1900 and S800 magnetic devices to centimeter accuracy. Several parameter searches have found the optimal settings for the triton beam production and (t,^{3}He) charge-exchange reaction and are well-documented. Experiments with the secondary triton beam are challenging compared to stable beam experiments, yet are now well under control.

Another major objective of this work was to measure B(GT$_+$) in the pf-shell nucleus ^{64}Cu. This was accomplished up to 6 MeV in excitation energy. Comparison is made to the same measurement made with the (d,^{2}He) reaction. The consistency of the (t,^{3}He) measurement was demonstrated by making this comparison, where a different normalization technique has been used to arrive at a consistent B(GT$_+$). This is greatly aided by the consistency of the (^{3}He,t) and (t,^{3}He) unit cross sections, which is one of several advantages the (t,^{3}He) probe has over (d,^{2}He) for measuring B(GT) in the isospin-raising

direction. Specifically, the advantage is that using the (^{3}He,t) unit cross section, which is established on a large body of high-quality (^{3}He,t) data, reduces the risk that the B(GT) extracted from (t,^{3}He) is normalized to a weak state. For states with weak B(GT), tensor effects break the proportionality with cross section strongly. This is a significant risk in the present case of ^{64}Cu because the only state with known B(GT) from β-decay is the weak ground state transition. And as is was shown here, where the tensor force effects have been studied in the DWBA, for transitions of comparable strength this can introduce a systematic error as large as 50% or more.

The final major objective here has been to determine electron-capture rates for ^{64}Cu, using both measured and shell-model B(GT$_+$) distributions. Again, the (t,^{3}He) result was compared to that of the (d,^{2}He) probe. The difference in the electron-capture rate between these two experimental results is probably a reasonable estimate of the error in the "measured" capture rate. The capture rate has been calculated in order to show what features of the B(GT$_+$) distribution are the most important for the rate calculation and subsequently, the shell-model performance. In this case, the performance of the NuShellX code using KB3G and GXPF1A effective interactions for determining the capture rate has been investigate. It is of course already known that the B(GT$_+$) lying in the first few MeV of excitation is the most important in terms of calculating the rate accurately. This is due to the strong temperature dependence created by the interplay between the sharp cut-off from the electron Fermi surface and the large phase-space enhancement of transitions to low-lying daughter states. Here, it has been shown that, despite significant differences between the ^{64}Cu B(GT$_+$) distribution yielded by KB3G and GXPF1A, neither perform well enough at low-lying excitation to reproduce the capture rate suggested by the data.

8.2 Outlook

There are several projects which could potentially improve the secondary triton beam at NSCL. The easiest project is largely already completed and that is addressing the low-intensity, angularly flat-background seen in the analysis of the ^{64}Cu spectrum. Since

the experiments reported on here were performed, the source of that background has been identified and removed. The background was a ^{3}He contaminant created by 3-neutron removal from ^{6}He, the most intense contaminant in the triton beam. The cross section for this reaction is comparable to the charge-exchange cross section. It has been removed from current experiments by introducing a wedge-degrader at the intermediate image plane of the A1900, at nearly no expense to the triton intensity or beam quality. Including this in the configuration of the A1900 will be crucial for future charge-exchange measurements, particularly at higher masses where the charge-exchange cross sections tend to decrease due to the behavior of the unit cross section. This is mainly due, recalling the discussion from Chapter 3, to increased distortion at higher mass which in turn, reduces the distortion term N_{D} in the unit cross section.

Another possible improvement of the triton beam would be enhanced extraction of the ^{16}O beam from the K1200 cyclotron and the transmission of the triton beam to the reaction target. Several improvements to NSCL CCF operations have already resulted from previous (t,^{3}He) measurements. During the ^{24}Mg measurement, ^{16}O intensities in the K1200 cyclotron created high neutron radiation levels, sufficient to shutdown computerized remote control hardware located inside the vault. This equipment has since been relocated outside the K1200 vault. Also, additional water shielding is now added to the K1200 vault roof to minimize activity outside. This has facilitated safe and reliable increases to the ^{16}O intensity, allowing for greater triton beam intensity. The present limit is now imposed by losses of the ^{16}O beam in the K1200 itself. At the time of the ^{64}Zn measurement, triton beam transmission efficiency, from the A1900 XFP to the reaction target, was typically 35%. This has been improved as part of a recent beam line realignment campaign to about 80%. Further increases in the triton beam intensity will be difficult to achieve without improved K1200 extraction efficiency, which minimizes the amount of ^{16}O particles lost in the K1200 and instead puts it on the production target.

Another difficulty faced in the ^{64}Zn measurement, the unreliable normalization of the incident triton beam, has since been remedied as well. The bias of the in-beam scintillator at the target, used to measure the triton rate, has been fine-tuned so as to avoid saturation

effects. In addition, due to the beamline realignment campaign, acceptances of the S800 spectrograph can now be modeled correctly over a large scattering angle range, up to nearly $\approx 5^{\circ}$ in the lab frame. In any event, the calibration of relative cross sections using the ^{12}C measurements as a reference cross section has proven fairly reliable. Additionally, the charge-exchange cross section is relatively high on this target and within an hour at typical triton intensities, the structure of ^{12}B can been seen directly in the CRDC position spectrum, making the ^{12}C target a valuable diagnostic tool.

The best method for increasing the triton beam intensity, from the point of view of higher beam intensity and quality, would be to temporarily decouple the K1200 and K500 cyclotrons, and develop a primary triton beam. This would require considerable overhead due to the decoupling, mounting of a source for the K1200 and developing a tritium source tune. The benefits would also be considerable however. The intensity gains would be 1-2 orders of magnitude and would allow many more targets to be measured with comparable beam time. Additionally, the energy spread of a primary triton beam would much smaller, possibly by a factor of 100. This would directly translate into a similarly sized improvement of the experimental energy resolution, to about 30 keV (FWHM), and open many possibilities for fine-structure studies similar to those made using (^{3}He,t) probe at RCNP. However, a major concern and a limit to the possible intensities are radiation safety concerns associated with tritium. Tritium source material and triton implantation-activation in the K1200 and beamlines are significant potential safety hazards that must be managed.

An additional, longer-range plan for upgrades might include a small scattering chamber, constructed for use as an alternative to the large scattering chamber currently in use with S800 spectrograph. The experimental setup in the reaction target area for the (t,^{3}He) charge-exchange studies requires two remote drives, one for targets and the other an in-beam scintillator, and thus is fairly simple. However, this is in spite of the constraints placed on the setup by the large scattering chamber. The large distances from mounting points inside the chamber make it difficult to accurately place targets and scintillators relative to the beam axis. As a consequence, there are more checks of the optics

required during the data analysis because of equipment alignment. Also, switching target ladders mid-experiment can potentially require that the alignment procedure of the setup to be repeated, costing valuable beam time. A smaller, modular scattering chamber, like the one used at the object location of the Analysis Line, would give greater control over the positioning of targets and scintillators and likely reduce the total overhead time to several hours. This would more efficiently use available beam time and better enable several targets to be measured in a single experiment.

Regarding the charge-exchange measurments themselves, the result for the ^{64}Zn measurement shows that variations in electron-capture rates, of the size seen between FFN and LMP below mass 60, persist at higher mass due to differences between shell-model and measured B(GT). This means that there is no reason to believe that similar disparities don't exist for an arbitrary, unmeasured B(GT). More B(GT$_+$) distributions on pf- and sdg-shell nuclei are needed to vet shell-model work in these regions of the nuclear landscape. The (d,^{2}He) reaction has a long history and has yielded a large body of B(GT$_+$) data in the pf-shell. It is unfortunate that there is no longer a functioning (d,^{2}He) program at intermediate beam energies. However, the data that exists is not being used to its full potential, to carefully study the performance of shell-model B(GT$_+$) calculations and their associated electron-capture rates. Aside from a revived (d,^{2}He) program, the (t,^{3}He) reaction is currently the only light charge-exchange probe for determining B(GT$_+$) with sub-MeV excitation energy resolution. Future (t,^{3}He) measurements should be proposed in order to investigate the upper pf- and sdg-shell region, paying particular attention to studying the effect a $g_{9/2}$ intruder state has on the B(GT$_+$) distribution. Measured B(GT$_+$) distributions in this mass region will build confidence that shell-model capture rates for nuclei that are unmeasurable are more likely to be realistic. Also, as B(GT) data and refined electron-capture rates have been made available for higher masses, the feedback they have with the supernova dynamics has tended to move the region of relevant masses for knowing the capture rates. For example, at the time of FFN's work, there were several capture parents in the sd-shell that were considered dominant over almost all other cases. The introduction of the LMP rate set

moved this region up solidly into the pf-shell. Currently, there is interest beyond this mass region, as reported by Hix *et al.* [4], that captures on nuclei with masses as high as $A = 120$ or more can play a role in the core-collapse explosion. A major goal of the (t,^{3}He) charge-exchange program should be to improve intensities and energy resolution so as to provide high resolution B(GT$_+$) data sets in these higher mass regions.

The shell-model calculations of B(GT$_+$) distributions must also improve for this effort to benefit supernova modeling. There is evidence that shell-model calculations in the upper pf-shell still do not adequately converge (M. Horoi, private communication). However, the NuShellX code is now performing calculations for some of the largest model-spaces ever. Efforts are already underway to perform a campaign of shell-model B(GT) calculations, to identify benchmark cases for further measurement and to serve as the basis of a new EC capture database using the GXPF1A effective interaction and it refinements. This author endorses and encourages this effort. This calculation survey is important because of the relatively large number of cases that can be measured. The number of cases is small, as stated previously, in terms of the number of transitions that will play a role at some point along a supernova trajectory. However, the number of measurable cases is still large enough that careful guidance is needed to make an experimental (t,^{3}He) campaign efficient with beam time is receives. Toward this end, it is important to determine the measurable cases that also provide the most insight into the shell-model interactions. Charge-exchange reactions performed in inverse kinematics with radiative beams promise to provide valuable information in this regard. The first charge-exchange reaction in inverse kinematics, using the (^{7}Li,^{7}Be) probe, was recently completed with a ^{28}S secondary beam and analysis is ongoing. Also, a new plastic scintillator array LENDA (Low-Energy Neutron Detector Array), for detecting low energy neutrons is under construction [151]. This array will enable (p,n) charge-exchange reaction studies in inverse kinematics with radioactive beams, providing B(GT$_-$) distributions in radioactive nuclei.

Bibliography

[1] F. Osterfeld. *Rev. Mod. Phys.*, 64:491–557, 1992.

[2] W. G. Love and M. A. Franey. *Phys. Rev. C*, 24:1073–1094, 1981.

[3] F. Brachwitz, D. J. Dean, W. R. Hix, K. Iwamoto, K. Langanke, G. Martínez-Pinedo, K. Nomoto, M. R. Strayer, F.-K. Thielemann, and H. Umeda. *Astrophys. J.*, 536:934–947, 2000.

[4] W. R. Hix, O. E. B. Messer, A. Mezzacappa, M. Liebendörfer, J. Sampaio, D. J. Dean, and G. Martínez-Pinedo. *Phys. Rev. Lett.*, 91:201102, 2003.

[5] I. Daito, H. Akimune, Sam M. Austin, D. Bazin, G. P. A. Berg, J.A. Brown, B. S. Davids, Y. Fujita, H. Fujimura, M. Fujiwaraa, R. Hazamad, T. Inomataa, K. Ishibashi, J. Jänecke, S. Nakayamaf, K. Pham, D. A. Roberts, B. M. Sherrill, M. Steiner, A. Tamiig, M. Tanakah, H. Toyokawa, and M. Yosoi. *Nucl. Instr. and Meth. A*, 397:465–471, 1997.

[6] B. M. Sherrill, H. Akimune, Sam M. Austin, D. Bazin, A. M. van den Berg, G. P. A. Berg, J. Caggiano, I. Daito, H. Fujimura, Y. Fujita, M. Fujiwara, K. Hara, M. N. Harakeh, J. Jänecke, T. Kawabata, A. Navin, D. A. Roberts, and M. Steiner. *Nucl. Instr. and Meth. A*, 432:299–304, 1999.

[7] G. W. Hitt, Sam M. Austin, D. Bazin, A. L. Cole, J. Dietrich, A. Gade, M. E. Howard, S. D. Reitzner, B. M. Sherrill, C. Simenel, E. E. Smith, J. Stetson, A. Stolz, and R. G. T. Zegers. *Nucl. Instr. and Meth. A*, 566:264–269, 2006.

[8] M. E. Howard, R. G. T. Zegers, Sam M. Austin, D. Bazin, B. A. Brown, A. L. Cole, M. Famiano, A. Gade, G. W. Hitt, M. Matos, S. D. Reitzner, C. Samanta, L. J. Schradin, Y. Shimbara, E. E. Smith, and C. Simenel. *Phys. Rev. C*, 78:047302, 2008.

[9] M. P. Nakada, J. D. Anderson, C. C. Gardner, J. McClure, and C. Wong. *Phys. Rev.*, 110:594–595, 1958.

[10] J. D. Anderson and C. Wong. *Phys. Rev. Lett.*, 7:250, 1961.

[11] J. D. Anderson, C. Wong, and J. W. McClure. *Phys. Rev.*, 126:2170, 1962.

[12] P. H. Bowen, G. C. Cox, G. B. Huxtable, J. P. Scanlon, and J. J. Thresher. *Nucl. Phys.*, 30:475–487, 1961.

[13] K. Ikeda, S. Fujii, and J. I. Fujita. *Phys. Lett.*, 3:271, 1963.

[14] R. R. Doering, A. Galonsky, D. M. Patterson, and G. F. Bertsch. *Phys. Rev. Lett.*, 35:1691–1693, 1975.

[15] G. L. Moake, L. J. Gutay, R. P. Scharenberg, P. T. Debevec, and P. A. Quinn. *Phys. Rev. Lett.*, 43:910–913, 1979.

[16] B. D. Anderson, J. N. Knudson, P. C. Tandy, J. W. Watson, R. Madey, and C. C. Foster. *Phys. Rev. Lett.*, 45:699, 1980.

[17] D. E. Bainum, J. Rapaport, C. D. Goodman, D. J. Hören, C. C. Foster, M. B. Greenfield, and C. A Goulding. *Phys. Rev. Lett.*, 44:1751, 1980.

[18] C. D. Goodman, C. A. Goulding, M. B. Greenfield, J. Rapaport, D. E. Bainum, C. C. Foster, W. G. Love, and F. Petrovich. *Phys. Rev. Lett.*, 44:1755, 1980.

[19] D. J. Hören, C. D. Goodman, C. C. Foster, C. A. Goulding, M. B. Greenfield, J. Rapaport, D. E. Bainum, E. Sugarbaker, T. G. Masterson, F. Petrovich, and W. G. Love. *Phys. Lett. B*, 95:27, 1980.

[20] D. J. Hören, C. D. Goodman, C. C. Foster, C. Gaarde, C. A. Goulding, M. B. Greenfield, J. Rapaport, T. N. Taddeucci, E. Sugarbaker, T. Masterson, S. M. Austin, A. Galonsky, and W. Sterrenburg. *Phys. Lett. B*, 99:383, 1981.

[21] C. Gaarde, J. Rapaport, T. N. Taddeucci, C. D. Goodman, C. C. Foster D. E. Bainum, C. A. Goulding, M. B. Greenfield D. J. Hören, and E. Sugarbaker. *Nucl. Phys. A*, 369:258, 1981.

[22] H. A. Bethe, G. E. Brown, J. Applegate, and J. M. Lattimer. *Nucl. Phys. A*, 324:487–533, 1979.

[23] G. M. Fuller, W. A. Fowler, and M. J. Newman. *Astrophys. J. Supp. Ser.*, 42:447, 1980.

[24] G. M. Fuller, W. A. Fowler, and M. J. Newman. *Astrophys. J.*, 252:715, 1982.

[25] G. M. Fuller, W. A. Fowler, and M. J. Newman. *Astrophys. J. Supp. Ser.*, 48:279, 1982.

[26] G. M. Fuller, W. A. Fowler, and M. J. Newman. *Astrophys. J.*, 293:1, 1985.

[27] G. M. Fuller, W. A. Fowler, and M. J. Newman. *http://ie.lbl.gov/astro/fuller.html*.

[28] W. P. Alford, R. L. Helmer, R. Abegg, A. Celler, O. Häusser K. Hicks, K. P. Jackson, C. A Miller, S. Yen, R. E. Azuma, D. Frekers, R. S. Henderson, H. Baer, and C. D. Zafiratos. *Phys. Lett. B*, 179:20–24, 1986.

[29] N. S. P. King, P. W. Lisowski, G. L. Morgan, P. N. Craig, R. G. Jeppesen, D. A. Lind, J. R. Shepard, J. L. Ullmann, C. D. Zafiratos, C. D. Goodman, and C. A. Goulding. *Phys. Lett. B*, 175:279, 1986.

[30] T. N. Taddeucci, J. Rapaport, D. E. Bainum, C. D. Goodman, C. C. Foster, C. Gaarde, J. Larsen, C. A. Goulding, D. J Horen, T. Masterson, and E. Sugarbaker. *Phys. Rev. C*, 25:1094, 1982.

[31] M. A. Franey and W. G. Love. *Phys. Rev. C*, 31:488–498, 1985.

[32] T. N. Taddeucci, C. A. Goulding, T. A. Carey, R. C. Byrd, C. D. Goodman, C. Gaarde, J. Larsen, D. Horen, J. Rapaport, and E. Sugarbaker. *Nucl. Phys. A*, 469:125–172, 1987.

[33] F. P. Brady, C. M. Castaneda, G. A. Needham, J. L. Ullmann, J. L. Romero, T. For, M. L. Johnson, N. S. P. King, C. M. Morris, F. Petrovich, and R. H. Howell. *Phys. Rev. Lett.*, 48:860, 1982.

[34] K. P. Jackson, A. Celler, W. P. Alford, K Raywood, R. Abegg, R. E. Azuma, C. K. Campbell, S. El-Kateb, D. Frekers, P. W. Green, O. Häusser, R. L. Helmer, R. S. Henderson, K. H. Hicks, R. Jeppesen, R. Lewis, C. A Miller, A. Moalem, M. A. Moinester, R. B. Schubank, G. G. Shute, B. M. Spicer, M. C. Vetterli A. I. Yavin, and S. Yen. *Phys. Lett. B*, 201:25–28, 1988.

[35] E. R. Flynn and J. D. Garrett. *Phys. Rev. Lett.*, 29:1748–1751, 1972.

[36] C. Ellegaard, C. Gaarde, J. S. Larsen, C. D. Goodman, I. Bergqvist, L. Carle'n, P. Ekström, B. Jakobsson, J. Lyttkens, M. Bedjidian, M. Chamcham, J. Y. Grossiord, A. Guichard, M. Gusakow, R. Haroutunian, J. R. Pizzi, D. Bachelier, J. L. Boyard, T. Hennino, J. C. Jourdin, M. Roy-Stephan, M. Boivin, and P. Radvanyi. *Phys. Rev. Lett.*, 50:1745, 1983.

[37] J. Jänecke, K. Pham, D. A. Roberts, D. Stewart, M. N. Harakeh, G. P. A. Berg, C. C. Foster, J. E. Lisantti, R. Sawafta, E. J. Stephenson, A. M. van den Berg, S. Y. van der Werf, S. E. Muraviev, and M. H. Urin. *Phys. Rev. C*, 48:2828–2839, 1993.

[38] H. Akimune, I Daito, Y. Fujita, M. Fujiwara, M. B. Greenfield, M. N. Harakeh, T. Inomata, J. Jänecke, K. Katori, S. Nakayama, H. Sakai, Y. Sakemi, M. Tanaka, and M. Yosoi. *Nucl. Phys. A*, 569:245c–254c, 1994.

[39] R. G. T. Zegers, A. M. van den Berg, S. Brandenburg, F. R. R. Fleurot, M. Fujiwara, J. Guillot, V. M. Hannen, M. N. Harakeh, H. Laurent, K. van der Schaaf, S. Y. van der Werf, A. Willis, and H. W Wilschut. *Phys. Rev. Lett.*, 84:3779, 2000.

[40] H. Okamura, S. Fujitaa, Y. Hara, K. Hatanaka, T. Ichihara, S. Ishida, K. Katoh, T. Niizeki, H. Ohnuma, H. Otsu, H. Sakai, N. Sakamoto, Y. Satou, T. Uesaka, T. Wakasaa, and T. Yamashita. *Phys. Lett. B*, 345:1–5, 1995.

[41] H. M. Xu, C. A. Gagliardi, G. K. Ajupova, B. Kokenge, and Y.-W. Lui. *Phys. Rev. C*, 54:3266–3269, 1996.

[42] S. Rakers, F. Ellinghaus, R. Bassini, C. Bäumer, A. M. van den Berg, D. Frekers, D. De Frenne, M. Hagemann, V. M. Hannen, M. N. Harakeh, M. Hartig, R. Henderson, J. Heyse, M. A. de Huu, E. Jacobs, M. Mielkea, J. M. Schippers, R. Schmidt, S. Y. van der Werf, and H. J. Wörtchea. *Nucl. Instr. and Meth. A*, 481:253–261, 2002.

[43] Yu. V. Gaponov and Yu. S. Lyutostanskii. *Sov. J. Nucl. Phys.*, 19:33, 1974.

[44] B. A. Brown and B. H. Wildenthal. *Annu. Rev. Nucl. Part. Sci.*, 38:29–66, 1988.

[45] T. Kajino, E. Shiino, H. Toki, B. A. Brown, and B. H. Wildenthal. *Nucl. Phys. A*, 480:175–187, 1988.

[46] K. Langanke and G. Martínez-Pinedo. *Nucl. Phys. A*, 673:481–508, 2000.

[47] The K500⊗K1200, A coupled cyclotron facility at the National Superconducting Cyclotron Laboratory. NSCL Report MSUCL-939, 1994.

[48] A. Heger, K. Langanke, G. Martínez-Pinedo, and S. E. Woosley. *Phys. Rev. Lett.*, 86:1678–1681, 2001.

[49] A. Heger, S. E. Woosley, G. Martínez-Pinedo, and K. Langanke. *Astrophys. J.*, 560:307–325, 2001.

[50] B. A. Brown *et al.* Report MSUCL-1289. Technical report, NSCL.

[51] W. D. M. Rae. NushellX for windows and linux. unpublished.

[52] A. Poves, J. Sánchez-Solano, E. Caurier, and F. Nowacki. *Nucl. Phys. A*, 694:157–198, 2001.

[53] M. Honma, T. Otsuka, B. A. Brown, and T. Mizusaki. *Phys. Rev. C*, 69:034335, 2004.

[54] B. E. J. Pagel. *Nucleosynthesis and Chemical Evolution of Galaxies*. Cambridge University Press, 1997.

[55] H. Joglekar, K. Gangala, M. N. Vahia, and A. Sule. *Puratattva, Journal of the Indian Archaeological Society*, 36, 2006.

[56] R. L. Gilliland and M. M. Phillips. *IAU Circular*, 1(6810), January 1998.

[57] Frieman *et al. Astron. J.*, 135:338, 2008.

[58] Sako *et al. Astron. J.*, 135:348, 2008.

[59] R. Minkowski. *Pub. Astron. Soc. Pac.*, 53:224–225, 1941.

[60] F. Bertola. *Ann. d'Ap.*, 27:319, 1964.

[61] J. H. Elias, K. Mathews, G. Neugebauer, and S. E. Persson. *Astrophys. J.*, 296:378, 1985.

[62] R. P. Harkness, J. C. Wheeler, B. Margon, R. A. Downes, R. P. Kirshner, A. Uomoto, E. S. Barker, A. L. Cochran, H. L. Dinerstein, D. R. Garnett, and R. M. Levreault. *Astrophys. J.*, 317:355, 1987.

[63] R. Barbon, F. Ciatti, and L. Rosino. *Astron. & Astrophys.*, 72:287–292, 1979.

[64] F. Zwicky. *Phys. Rev. Series II*, 55:726, 1939.

[65] E. Hubble. 15(3):168–173, 1929.

[66] C. T. Kowal. *Astron. J.*, 73:1021, 1968.

[67] G. A. Tammann. *Rev. Mod. Astron.*, 19:1–29, 2008.

[68] G. A. Tammann. In *Scientific Research with the Space Telescope*, volume 263, Washington. Printing Office.

[69] M. M. Phillips et.al. *Publ. Astron. Soc. Pac.*, 99:592, 1987.

[70] M. M. Phillips, P. Lira, N. B. Suntzeff, R. A. Schommer, M. Hamuy, and J. Maza. *Astron. J.*, 118:1766–1776, 1999.

[71] S. Perlmutter textitet al. *Astrophys. J.*, 517:565, 1999.

[72] E. M. Burbidge, G. R. Burbidge, W. A. Fowler, and F. Hoyle. *Rev. Mod. Phys.*, 29:547–654, 1957.

[73] W. A. Fowler and F. Hoyle. *Astron. J.*, 65:345, 1960.

[74] K. Nomoto, K. Thielemann, and K. Yokoi. *Astrophys. J.*, 286:644, 1984.

[75] P. Hoeflich and A. Khokhlov. *Astrophys. J.*, 457:500–528, 1996.

[76] P. Nugent, E. Baron, D. Branch, A. Fisher, and P. H. Hauschildt. *Astrophys. J.*, 485:812–819.

[77] P. A. Mazzali, N. Chugai, M. Turatto, L. B. Lucy, I. J. Danziger, E. Cappellaro, M. della Valle, and S. Benetti. *Mon. Not. R. Astron. Soc.*, 284:151–171, 1997.

[78] A. Fisher, D. Branch, K. Hatano, and E. Baron. *Mon. Not. R. Astron. Soc.*, 304:67–74, 1999.

[79] E. Livne. *Astrophys. J.*, 354:L53, 1990.

[80] A. Khokhlov, E. Müller, and P. Höflich. *Astron. Astrophys.*, 270:223, 1993.

[81] P. Höflich, E. Müller, and A. Khokhlov. *Astron. Astrophys.*, 268:570, 1993.

[82] Ruiz-Lapuente *et al. Nature*, 365:728, 1993.

[83] S. E. Woosley and T. A. Weaver. *Astrophys. J.*, 423:371, 1994.

[84] P. Höflich, A. Khokhlov, and J. C. Wheeler. 444:831.

[85] E. Livne and D. Arnett. *Astrophys. J.*, 452:62, 1995.

[86] P. Höflich and A. Khokhlov. *Astrophys. J.*, 457:500, 1996.

[87] W. Hillebrandt and J. C. Niemeyer. *Annu. Rev. Astron. Astrophys.*, 38:191–230, 2000.

[88] D. Branch. *Annu. Rev. Astron. Astrophys.*, 36:17–55, 1998.

[89] S. E. Woosley, A. Almgren, J. B. Bell, G. Glatzmaier, D. Kasen, A. R. Kerstein, H. Ma, P. Nugent, F. Röpke, V. Sankaran, and M. Zinalge. Type Ia Supernovae. volume 78, page 012081. SciDAC 2007, IOP Publishing, 2007.

[90] W. Baade and F. Zwicky. *Proc. Nat. Acad. Sci.*, pages 254–259, 1934.

[91] S. E. Woosley and T. A. Weaver. *Astrophys. J. Supp. Ser.*, 101:181, 1995.

[92] F. Hoyle and W. A. Fowler. *Astrophys. J.*, 132:565, 1960.

[93] W. A. Fowler and F. Hoyle. *Astrophys. J. Supp. Ser.*, 9:201, 1964.

[94] J. Audouze, C. Chiosi, and S. E. Woosley. *Nucleosynthesis and Chemical Evolution*. Sauverny: Geneva Observatory, March 1986. Proceedings of the 16th Advanced Course of the Swiss Society of Astronomy and Astrophysics (SSAA).

[95] S. W. Bruenn. *Astrophys. J. Supp. Ser.*, 58:771–841, 1985.

[96] T. A. Weaver and S. E. Woosley. *Phys. Rep.*, 227:65–96, 1993.

[97] A. Mezzacappa, M. Liebendörfer, O. E. B. Messer, W. R. Hix, F. Thielemann, and S. W. Bruenn. *Phys. Rev. Lett.*, 86:1935–1938, 2001.

[98] R. Buras, M. Rampp, H. Th. Janka, and K. Kifonidis. *Phys. Rev. Lett.*, 90:241101, 2003.

[99] K. S. Krane. *Introductory Nuclear Physics*. John Wiley & Sons, Inc., New York, 1988. p.277-282.

[100] B. H. Wildenthal. *Elementary Modes of Excitation in Nuclei*. 1977. p.69.

[101] K. Langanke, D. J. Dean, P. B. Radha, Y. Alhassid, and S. E. Koonin. *Phys. Rev. C*, 52:718, 1995.

[102] G. Martínez-Pinedo, A. Poves, E. Caurier, and A. P. Zuker. *Phys. Rev. C*, 53:R2602–R2605, 1996.

[103] K. Langanke. *Nucl. Phys. A*, 687:303c, 2001.

[104] W. R. Hix. private communication.

[105] G. Martínez-Pinedo, K. Langanke, and D. J. Dean. *Astrophys. J. Supp. Ser.*, 126:493, 2000.

[106] K. Langanke and G. Martínez-Pinedo. *Nucl. Phys. A*, 731:365–378, 2004.

[107] M. Honma, T. Otsuka, B. A. Brown, and T. Mizusaki. *Eur. Phys. J. A*, 25:499–502, 2005.

[108] A. K. Kerman, H. McManus, and R. M. Thaler. *Annu. Phys.*, 8:551, 1959.

[109] G. R. Satchler. *Nucl. Phys. A*, 55:1, 1964.

[110] R. G. T. Zegers, T. Adachi, H. Akimune, Sam M. Austin, A. M. van den Berg, B. A. Brown, Y. Fujita, M. Fujiwara, S. Galés, C. J. Guess, M. N. Harakeh, H. Hashimoto, K. Hatanaka, R. Hayami, G. W. Hitt, M. E. Howard, M. Itoh, T. Kawabata, K. Kawase, M. Kinoshita, M. Matsubara, K. Nakanishi, S. Nakayama, S. Okumura, T. Ohta, Y. Sakemi, Y. Shimbara, Y. Shimizu, C. Scholl, C. Simenel, Y. Tameshige, A. Tamii, M. Uchida, T. Yamagata, and M. Yosoi. *Phys. Rev. Lett.*, 99:202501, 2007.

[111] R. G. T. Zegers, H. Akimune, Sam M. Austin, D. Bazin, A. M. van den Berg, G. P. A. Berg, B. A. Brown, J. Brown, A. L. Cole, I. Daito, Y. Fujita, M. Fujiwara, S. Galès, M. N. Harakeh, H. Hashimoto, R. Hayami, G. W. Hitt, M. E. Howard, M. Itoh, J. Jänecke, T. Kawabata, K. Kawase, M. Kinoshita, T. Nakamura, K. Nakanishi, S. Nakayama, S. Okumura, W. A. Richter, D. A. Roberts, B. M. Sherrill, Y. Shimbara, M. Steiner, M. Uchida, H. Ueno, T. Yamagata, and M. Yosoi. *Phys. Rev. C*, 74:024309, 2006.

[112] A. L. Cole, H. Akimune, Sam M. Austin, D. Bazin, A. M. van den Berg, G. P. A. Berg, J. Brown, I. Daito, Y. Fujita, M. Fujiwara, S. Gupta, K. Hara, M. N. Harakeh, J. Jänecke, T. Kawabata, T. Nakamura, D. A. Roberts, B. M. Sherrill, M. Steiner, H. Ueno, and R. G. T. Zegers. *Phys. Rev. C*, 74:034333, 2006.

[113] T. Udagawa, A. Schultz, and F. Osterfeld. *Nucl. Phys. A*, 474:131–154, 1987.

[114] J. Cook and J. Carr. Computer program FOLD. Florida State University (unpublished); based on F. Petrovich and D. Stanley, *Nucl. Phys. A* 275:487, 1977; modified as described in J. Cook *et al.*, *Phys. Rev. C* 30:1538, 1984; R. G. T. Zegers, S. Fracasso, and G. Colo‘ (unpublished)., 1988.

[115] B. A. Brown. *Phys. Rev. C*, 58:220, 1998.

[116] S. Cohen and D. Kurath. *Nucl. Phys. A*, 101:1, 1967.

[117] H. Hyuga, A. Arima, and K. Shimizu. *Nucl. Phys. A*, 336:363, 1980.

[118] M. Ericson, A. Figureau, and C. Thévenet. *Phys. Lett. B*, 45:19, 1973.

[119] J. Raynal. *Nucl. Phys. A*, 97:572, 1967.

[120] J. Carr, F. Petrovich, and J. Kelly. Computer program ALLWORLD. unpublished.

[121] G. R. Satchler. *Direct Nuclear Reactions*. Claredon Press, Oxford, 1983.

[122] J. Kamiya, K. Hatanaka, T. Adachi, K. Fujita, K. Hara, T. Kawabata, T. Noro, H. Sakaguchi, N. Sakamoto, Y. Sakemi, Y. Shimbara, Y. Shimizu, S. Terashima, M. Uchida, T. Wakasa, Y. Yasuda, H. P. Yoshida, and M. Yosoi. *Phys. Rev. C*, 67:064612, 2003.

[123] S. Y. van der Werf, S. Brandenburg, P. Grasdijk, W. A. Sterrenburg, M. N. Harakeh, M. B. Greenfield, B. A. Brown, and M. Fujiwara. *Nucl. Phys. A*, 496:305–332, 1989.

[124] D. J. Morrissey, B. M. Sherrill, M. Steiner, A. Stolz, and I. Wiedenhoever. *Nucl. Instr. and Meth. B*, 204:90–96, 2003.

[125] D. Bazin, J. A. Caggiano, B. M. Sherrill, J. Yurkon, and A. Zeller. *Nucl. Instr. and Meth. B*, 204:629–633, 2003.

[126] J. Yurkon, D. Bazin, W. Benenson, D. J. Morrissey, B. M. Sherrill, D. Swan, and R. Swanson. *Nucl. Instr. and Meth. A*, 422:291–295, 1999.

[127] E. W. Grewe, C. Bäumer, A. M. van den Berg, N. Blasi, B. Davids, D. De Frenne, D. Frekers, P. Haefner, M. N. Harakeh, M. Huynyadi, E. Jacobs, B. Junk, A. Korff, A. Negret, P. von Neumann-Cosel, L. Popescu, S. Rakers, and H. J. Wörtche. *Phys. Rev. C*, 69:064325, 2004.

[128] I. Daito, H. Akimune, Sam M. Austin, D. Bazin, G. P. A. Berg, J. A. Brown, B. S. Davids, Y. Fujita, H. Fujimura, M. Fujiwara, R. Hazama, T. Inomata, K. Ishibashi, J. Jnecke, S. Nakayama, K. Pham, D. A. Roberts, B. M. Sherrill, M. Steiner, and A. Tamii and. *Phys. Lett. B*, 418:27–33, 1998.

[129] T. Nakamura, T. Aumann, D. Bazin, Y. Blumenfeld, B. A. Brown, J. Caggiano, R. Clement, T. Glasmacher, P. A. Lofy, A. Navin, B. V. Pritychenko, B.M. Sherrill, and J. Yurkon. *Phys. Lett. B*, 493:209–215, 2000.

[130] H. Geissel, G. Münzenberger, and K. Riisager. *ARNPS*, 45:163–203, 1995.

[131] K. Sümmerer and B. Blank. *Phys. Rev. C*, 61(034607), 2000.

[132] D. Bazin, O.B. Tarasov, M. Lewitowicz, and O. Sorlin. *Nucl. Instr. and Meth. A*, 482:307, 2002.

[133] N. Iwasa, H. Geissel, G. Münzenberg, C. Scheidenberger, Th. Schwab, and H. Wollnik. *Nucl. Instr. and Meth. B*, 126:284, 1997.

[134] K. Makino and M. Berz. *Nucl. Instr. and Meth. A*, 427:338, 1999.

[135] M. Berz, K. Joh, J. A. Nolen, B. M. Sherrill, and A. F. Zeller. *Phys. Rev. C*, 47:537, 1993.

[136] P. M. Endt, J. Blachot R. B. Firestone, and J. Zipkin. *Nucl. Phys. A*, 633:1, 1988.

[137] H. Fujita, Y. Fujita, G. P. A. Berg, A. D. Bacher, C. C. Foster, K. Hara, K. Hatanaka, T. Kawabata, T. Noro, H. Sakaguchi, Y. Shimbara, T. Shinada, E. J. Stephenson, H. Ueno, and M. Yosoi. *Nucl. Instr. and Meth. A*, 484:17–26, 2002.

[138] J. A. Caggiano. PhD thesis, Michigan State University, 1999.

[139] R. Meharchand, H. Akimune, A. M. van den Berg, Y. Fujita, M. Fujiwara, S. Galés, M. N. Harakeh, H. Hashimoto, R. Hayami, G. W. Hitt, M. Itoh, T. Kawabata, K. Kawase, M. Kinoshita, K. Nakanishi, S. Nakayama, S. Okumura, Y. Shimbara, M. Uchida, T. Yamagata, M. Yosoi, and R. G. T. Zegers. *Nucl. Instr. and Meth. B*, 264:221–226, 2007.

[140] A. H. Wapstra, G. Audi, and C. Thibault. *Nucl. Phys. A*, 729:129, 2003.

[141] G. Audi, A. H. Wapstra, and C. Thibault. *Nucl. Phys. A*, 729:337, 2003.

[142] B. Singh. In *Nucl. Data Sheets*, volume 108, page 197. 2007.

[143] E. W. Grewe, C. Bäumer, H. Dohmann, D. Frekers, M. N. Harakeh, S. Hollstein, H. Johansson, K. Langanke, G. Martínez-Pinedo, F. Nowacki, I. Petermann, L. Popescu, S. Rakers, D. Savran, K. Sieja, H. Simon, J. H. Thies, A. M. van den Berg, H. J. Wörtche, and A. Zilges. *Phys. Rev. C*, 77:064303, 2008.

[144] Z. Sujkowski and S. Wycech. *Phys. Rev. C*, 70:052501, 2004.

[145] L. Popescu. PhD thesis, Gent University, 2008.

[146] R. Firestone and V. S. Shirley. *Table of Isotopes*. John Wiley & Sons, Inc., New York, 1996.

[147] M. Honma, T. Otsuka, B. A. Brown, and T. Mizusaki. *Phys. Rev. C*, 65:061301, 2002.

[148] R. R. Johnson and G. D. Jones. *Nucl. Phys. A*, 122:657–666, 1968.

[149] A. Burrows, E. Livne, L. Dessart, C. D. Ott, and J. Murphy. *N. Astr. Rev.*, 50:487–491, 2006.

[150] J. W. Murphy and A. Burrows. *Astrophys. J. Supp. Ser.*, 179:209–241, 2008.

[151] G. Perdikakis, Sam M. Austin, D. Bazin, C. Caesar, J. M. Deaven, C. J. Guess, G. W. Hitt, R. T. Meharchand, D. T. Nguyen, Y. Shimbara, K. Thorne, and R. G. T. Zegers. *LENDA: A Low Energy Neutron Detector Array for Studies of (p,n) Reactions with Radioactive Beams*. Berkley, 2008. Symposium on Radiation Measurments and Applications - SORMA.